

***In silico* Investigation of the Fluid Structure Interaction in  
Spinal Cord and Subarachnoid Space**

BY

YIFEI LIU

B.S., DONG HUA UNIVERSITY, CHINA, 2002

THESIS

Submitted as partial fulfillment of the requirements  
for the degree of Master of Science in Mechanical Engineering  
in the Graduate College of the  
University of Illinois at Chicago, 2010  
Chicago, Illinois

To my family: Xianzhi Wang, Yirong Liu, and my late father Fumin Liu

## ACKNOWLEDGMENTS

I would like to express my gratitude to my advisor, Dr. Thomas J. Royston, who gave me the opportunity to come back to school and start my graduate study. This work will never be completed without his help and support. His inspiration and guidance helped me not only accomplish my research but to enjoy myself in the process. I would also like to thank Dr. Bryn A. Martin, for his precious help and critique during the last several months, which are really valuable in guiding and improving this research. Many thanks to Dr. Francis Loth for his help in the past year and his helpful critique on this thesis, and especially thanks for his coming all the way from Ohio to serve on my defense committee. And I would also like to thank to Dr. Richard L. Magin for serving on my committee member.

Special thanks are also given to my Lab-mates, Zoujun Dai, Kaya Yaşar, and Ying Peng, who have given me so much assistance in my research.

Most importantly, I would like to thank my family: my mother Xianzhi Wang, my sister Yirong Liu, and my late father Fumin Liu. Without their continuous and unwavering support, I would never be who I am. The death by illness of my father changed my interest to the area of medical technology development. And it's my mother and my sister's encouragement and support that helped me make the decision to come back to school.

# TABLE OF CONTENTS

<i>ACKNOWLEDGMENTS</i> .....	<i>IV</i>
<i>TABLE OF CONTENTS</i> .....	<i>V</i>
<i>LIST OF TABLES</i> .....	<i>VII</i>
<i>LIST OF FIGURES</i> .....	<i>VIII</i>
<i>SUMMARY</i> .....	<i>XIII</i>
<b>CHAPTER 1 INTRODUCTION AND ANATOMY BACKGROUND</b> .....	<b>1</b>
<b>1.1 Vertebral Column Anatomy</b> .....	<b>2</b>
<b>1.2 Meninges</b> .....	<b>4</b>
<b>1.3 Spinal Cord Anatomy</b> .....	<b>5</b>
<b>1.4 Cerebrospinal Fluid and the Subarachnoid Spaces</b> .....	<b>7</b>
<b>1.5 Syringomyelia</b> .....	<b>9</b>
<b>1.5.1 Symptoms and Diagnosis</b> .....	<b>11</b>
<b>1.5.2 Treatment and Prognosis</b> .....	<b>12</b>
<b>1.5.3 Causes, Theories, and Existed Engineering Models</b> .....	<b>13</b>
<b>CHAPTER 2 FINITE ELEMENT MODELS CONSTRUCTION AND DEFINITION</b> .....	<b>21</b>
<b>2.1 Model Definition</b> .....	<b>21</b>
<b>2.2 Element Definition</b> .....	<b>23</b>
<b>2.3 Material Properties</b> .....	<b>26</b>
<b>2.4 Dimensions</b> .....	<b>29</b>
<b>2.5 Mesh</b> .....	<b>29</b>
<b>2.6 Boundary Conditions</b> .....	<b>30</b>
<b>CHAPTER 3 INFLUENCE OF ELASTIC PROPERTIES OF THE SPINAL AQUEDUCT</b> .....	<b>33</b>
<b>3.1 Introduction</b> .....	<b>33</b>
<b>3.2 Methodology</b> .....	<b>34</b>

3.3 Results .....	37
3.3.1 The influence of dura material properties on the spinal system (CSD) .....	37
3.3.2 The influence of spinal cord on the spinal system (CLSD and CRSD) .....	46
3.4 Theory .....	50
3.5 Discussion and Conclusion.....	52
<b>CHAPTER 4 INFLUENCE OF STENOSIS AND/OR SYRINX.....</b>	<b>54</b>
4.1 Introduction .....	54
4.2 Methodology.....	55
4.3 Results .....	60
4.3.1 Normal CSF Flow Waveform Input Result.....	61
4.3.1.1 Pressure changes over time .....	62
4.3.1.2 Pressure distribution and wave propagation speed.....	66
4.3.1.3 Pressure and displacement at different times .....	70
4.3.2 Coughing Effect Results.....	78
4.3.2.1 Pressure changes over time .....	78
4.3.2.2 Longitudinal pressure dissociation (LPD) .....	81
4.3.2.3 Transmural pressure (TP).....	83
4.3.2.4 Pressure distribution and wave propagation speed.....	84
4.3.2.5 Pressure and displacement at different times .....	88
4.4 Conclusion and Discussion.....	95
<b>CHAPTER 5 FUTURE STUDIES .....</b>	<b>99</b>
<b>CITED LITERATURE.....</b>	<b>101</b>
<b>VITA .....</b>	<b>104</b>

## LIST OF TABLES

Table 2-1: Element Definitions and Material in the <i>In vitro</i> Models for Each Component .....	24
Table 3-1: Dimensions for Models in Elastic Properties Group: CSD, CLSD, and CRSD .....	35
Table 3-2: Material Properties for Models in Elastic Properties Group: CSD, CLSD, and CRSD.....	36
Table 3-3: Summary of wave speeds for different models measured in the <i>in silico</i> and <i>in vitro</i> models, and calculated by theory .....	53
Table 4-1: Dimensions of the Six Models Examining Influence of Blockage in CSF Flow and/or Syring in Spinal Cord on the Spinal system.....	57
Table 4-2: Material properties of the six Post-Traumatic group models.....	60
Table 4-3: Summary of wave speeds for the six models measured in the <i>in silico</i> and <i>in vitro</i> models.....	98

## LIST OF FIGURES

Figure 1-1: Classification of vertebral column: cervical, thoracic, lumbar, and pelvic. [1]	3
Figure 1-2: Diagram of vertebrae. (a): traverse section view of vertebrae [6] (b) left posterolateral view of articulated vertebrae [7].....	4
Figure 1-3: Transverse section of spinal cord [6]. Spinal cord meninges are denoted in the figure. ....	5
Figure 1-4: Transverse section through spinal cord [6]. ....	6
Figure 1-5: Pathway of cerebrospinal fluid circulation [3].....	8
Figure 1-6: Syringomyelia (a) diagram of syrinx formed in spinal cord. (b) MRI image of a syrinx formed in the spinal cord. [12].....	9
Figure 1-7: Sagittal MRI of head of sub-cranial subarachnoid space of a patient with Arnold-Chiari malformation and Syringomyelia [14].....	10
Figure 1-8: A case of a temporary ACM/ syrinx: 28 yr old female with a car accident head injury, and after the injury healed, the ACM/syrinx almost disappeared. Source- W.C. Clivero and D.H. Dinh, Neurology, v. 30, #5, 758 (1992).Submitted by Bernie H. Meyer [18].....	14
Figure 2-1: Geometry, node locations, element face index and coordinate system of element Fluid 79[35].....	24
Figure 2-2: A gap could occur when an 8-node element meshes with 4-node element, because a deformed mesh may be curved along the 8-node element edge, while the 4-node elements have linear edges. ....	25
Figure 2-3: Geometry, node locations, element face index and coordinate system of Plane 182.....	26
Figure 2-4: An example of mesh in region of stenosis in model SSE. ....	30
Figure 2-5: Boundary conditions defined in the <i>in silico</i> models. The model in this figure is a scale-exaggerated CSD model. The nodes located on the Y-axis are fixed radially, and both ends of solid (dura and SC) are fixed axially. ....	32
Figure 3-1: Geometries for Model: CSD and CLSD. The horizontal to vertical scale is exaggerated. The dimensions and boundary conditions are defined based on the <i>in vitro</i> models. ....	37

Figure 3-2: Pressure vs. time at the pressure port 1 (close to the excited end) of the model (solid line) and at the pressure port 10 (dash line) in response to a smooth sinusoidal excitation transient of duration 100 ms (a) and 50 ms (b). Pressure transient input with amplitude of 100 mmHg is plotted as a green dash line. ....	38
Figure 3-3: Spatial vs. temporal pressure in SAS during the first 500 ms after the start of a sinusoidal excitation transient of duration 100 ms (a) and 50 ms (b). ....	40
Figure 3-4: Pressure vs. time at the pressure port 1 (close to the excited end) of the model (solid line) and at the pressure port 10 (dash line) in response to a symmetric triangular impulse of duration 50 ms (a) and 5 ms (b). Pressure transient input with amplitude of 100 mmHg is the green dash line. ....	41
Figure 3-5: Spatial vs. temporal pressure result in SAS after a triangular excitation is applied. (a) Pressure during the first 500 ms after the start of a triangular transient of duration 50 ms. (b) Pressure during the first 100 ms after the start of a triangular transient of duration 5 ms. ....	42
Figure 3-6: Pressure result for CSD model with 5.2 mm dura in response to a 5 ms triangular impulse during the first 100 ms. (a) Pressure vs. time result at pressure point 1 (solid line) and pressure point 10 (dash line). (b) Spatial vs. temporal pressure result in SAS along the spine. ....	43
Figure 3-7: Pressure result for CSD model with 12 mm dura in response to a 5 ms triangular impulse during the first 100 ms. (a) Pressure vs. time result at pressure point 1 (solid line) and pressure point 10 (dash line). (b) Spatial vs. temporal pressure result in SAS along the spine. ....	44
Figure 3-8: Pressure result for CSD model with 17.9 mm dura in response to a 5 ms triangular impulse during the first 100 ms. (a) Pressure vs. time result at pressure point 1 (solid line) and pressure point 10 (dash line). (b) Spatial vs. temporal pressure result in SAS along the spine. ....	45
Figure 3-9: Pressure result for CSD model with 17.9 mm dura in response to a 5 ms triangular impulse during the first 20 ms. The first three waves can be seen in the figure; the fastest wave is the weakest one arriving at the rostral end of the spine at about 0.012 second. Interaction of the reflection of the first wave and the second wave can also be seen in the plot. ....	45
Figure 3-10: Pressure result for cordless model (CLSD) with different thickness dura in response to a 5 ms triangular impulse during the first 100 ms. (a), (c), (e),(g): Pressure vs. time result at pressure point 1 (solid line) and pressure point 10 (dash line) for dura thickness 2.3 mm, 5.2 mm, 12 mm, and 17.9	

mm, respectively. (b), (d), (f), (h): Spatial vs. temporal pressure result in the SAS along the spine for dura thickness 2.3 mm, 5.2 mm, 12 mm, and 17.9 mm, respectively. ....	48
Figure 3-11: Pressure results for rigid cord model (CRSD) with different thickness dura in response to a 5 ms triangular impulse during the first 100 ms. (a), (c), (e), (g): Pressure vs. time result at pressure point 1 (solid line) and pressure point 10 (dash line) for dura thickness 2.3 mm, 5.2 mm, 12 mm, and 17.9 mm, respectively. (b), (d), (f), (h): Spatial vs. temporal pressure result in SAS along the spine for dura thickness 2.3 mm, 5.2 mm, 12 mm, and 17.9 mm, respectively. ....	50
Figure 4-1: Detailed structure and dimensions of the glass encasing tube for the <i>in vitro</i> models.[5].....	57
Figure 4-2: Geometries of the seven 2-D axisymmetric models set up in ANSYS. The horizontal to vertical scale is exaggerated. The dimensions and boundary conditions are defined based on the <i>in vitro</i> models. Position of pressure sampled element in SAS and Syringe can be found in the figure .....	58
Figure 4-3: CSF flow waveform in the <i>in vitro</i> models which was obtained based on <i>in vivo</i> measurement at C2 level [5]. .....	61
Figure 4-4: CSF flow waveform applied at the <i>in silico</i> models, which is a replication of the <i>in vitro</i> input. ....	62
Figure 4-5: Pressure in SAS at the ten pressure port positions in the first 5 seconds in response to excitation of continuous normal CSF pulsation for the six models. Pressure at each port has 10 mm Hg deductions from the anterior port.....	64
Figure 4-6: Pressure in syringe at pressure port positions in the first 5 seconds in response to excitation of continuous normal CSF pulsation for the six models. Pressure at each port has 10 mm Hg deductions from the anterior port. ....	65
Figure 4-7: Spatial vs. temporal pressure result of CSRD in the first 5 seconds in response to periodic excitation of CSF flow. ....	66
Figure 4-8: Spatial vs. temporal pressure in SAS result of for the six models in the first 1 second in response to periodic excitation of CSF flow.....	68
Figure 4-9: Spatial vs. temporal pressure in syringe result of for the six models in the first 1 second in response to periodic excitation of CSF flow. ....	69
Figure 4-10: Pressure in SAS along the spine and displacement of spinal cord in response to excitation of continuous normal CSF pulsation for CSRD models at $t = 0.1, 0.2, \dots, 1$ second, identified as curves 1, 2, ..., 10. ....	73

Figure 4-11: Pressure in SAS along the spine and displacement of spinal cord in response to excitation of continuous normal CSF pulsation for SAE models at $t = 0.1, 0.2, \dots, 1$ second, identified as curves 1, 2, ..., 10. ....	73
Figure 4-12: Pressure in SAS and syrinx along the spine, transmural pressure in the system and displacement of spinal cord and syrinx in response to excitation of continuous normal CSF pulsation for SSE model at $t = 0.1, 0.2, \dots, 1$ second, identified as curves 1, 2, ..., 10. Syrinx and stenosis are denoted in different gray area. ....	74
Figure 4-13: Pressure in SAS and syrinx along the spine, transmural pressure in the system and displacement of spinal cord and syrinx in response to excitation of continuous normal CSF pulsation for SRE model at $t = 0.1, 0.2, \dots, 1$ second, identified as curves 1, 2, ..., 10. Syrinx is denoted in gray area. ....	75
Figure 4-14: Pressure in SAS and syrinx along the spine, transmural pressure in the system and displacement of spinal cord and syrinx in response to excitation of continuous normal CSF pulsation for the SSED model at $t = 0.1, 0.2, \dots, 1$ second, identified as curves 1, 2, ..., 10. Syrinx and stenosis are denoted in different gray area. ....	76
Figure 4-15: Pressure in SAS and syrinx along the spine, transmural pressure in the system and displacement of spinal cord of syrinx in response to excitation of continuous normal CSF pulsation for SRED model at $t = 0.1, 0.2, \dots, 1$ second, identified as curves 1, 2, ..., 10. Syrinx is denoted in gray area ....	77
Figure 4-16: Pressure in SAS at the ten pressure ports position in the first 200 ms in response to 5 ms pressure transient. Pressure at each port has 10 mmHg deductions from the anterior port. ....	80
Figure 4-17: Pressure in syrinx at the ten pressure port positions in the first 200 ms in response to 5 ms pressure transient. Pressure at each port has 10 mmHg deductions from the anterior port. ....	81
Figure 4-18: Longitudinal pressure dissociation (LPD) for models with rigid dura. (a): LPD in the first 0.2 second. (b): zoomed in plot of LPD in the first 20 ms. ....	82
Figure 4-19: Longitudinal pressure dissociation (LPD) for models with distensible dura. (a): LPD in the first 0.2 second. (b): zoomed in plot of LPD in the first 20 ms. ....	83
Figure 4-20: Transmural pressure (TD) for models with syrinx in the first 200 ms. ....	84
Figure 4-21: Spatial vs. temporal pressure in SAS results in the first 30 ms in response to transient impulse. ....	86

Figure 4-22: Spatial vs. temporal pressure in syrinx result in the first 30 ms in response to transient impulse.....	87
Figure 4-23: Pressure in SAS along the spine and displacement of spinal cord in response to excitation of 5 mm triangular impulse for CSRD models at t = 5, 10, ..., 50 ms, identified as curves 1, 2, ..., 10. ....	90
Figure 4-24: Pressure in SAS along the spine and displacement of spinal cord in response to excitation of 5 mm triangular impulse for SAE models at t = 5, 10, ..., 50 ms, identified as curves 1, 2, ..., 10. ....	90
Figure 4-25: Pressure in SAS and syrinx along the spine, transmural pressure in the system and displacement of spinal cord and syrinx in response to excitation of 5 mm triangular impulse for the SSE model at t = 5, 10, ..., 50 ms, identified as curves 1, 2, ..., 10. Syrinx and stenosis are denoted in different gray area.....	91
Figure 4-26: Pressure in SAS and syrinx along the spine, transmural pressure in the system and displacement of spinal cord and syrinx in response to excitation of 5 mm triangular impulse for the SRE model at t = 5, 10, ..., 50 ms, identified as curves 1, 2, ..., 10. Syrinx and stenosis are denoted in different gray area.....	92
Figure 4-27: Pressure in SAS and syrinx along the spine, transmural pressure in the system and displacement of spinal cord and syrinx in response to excitation of 5 mm triangular impulse for the SSE model at t = 10, 20, ..., 100 ms, identified as curves 1, 2, ..., 10. Syrinx and stenosis are denoted in different gray area. ....	93
Figure 4-28: Pressure in SAS and syrinx along the spine, transmural pressure in the system and displacement of spinal cord and syrinx in response to excitation of continuous normal CSF pulsation for the SRED model at t = 10, 20, ..., 100 ms, identified as curves 1, 2, ..., 10. Syrinx and stenosis are denoted in different gray area.....	94
Figure 4-29: The first impulse of pressure in SAS at the ten pressure port positions in the first 20 ms in response to 5 ms pressure transient. ....	97
Figure 4-30: Valve-like action in systole (left) and diastole (right) of the syrinx in SC [43].....	97

## SUMMARY

Spinal system disease, especially those diseases concerning the fluid-structure interaction (FSI) in the system, has attracted more and more attention from neurosurgeons as well as engineers. While *in vivo* and *in vitro* studies provide some insight into the pathology and lead to hypotheses based on observable and measurable parameters, like the pressure in the cerebrospinal fluid (CSF) traveling within the subarachnoid space (SAS) at different locations, these studies are limited in their ability to validate these hypotheses. *In silico* simulations, on the other hand, offer a feasible way to analyze in detail the independent effect of various mechanisms, parameters and geometries, and provide detailed and comprehensive information on the pressure as well as other parameters of interest.

This thesis is focused on *in silico* investigation of the factors that might influence FSI within the spinal system. Two major groups of models were constructed using the finite element code ANSYS (ANSYS Inc., Canonsburg, PA). The first group of models (Elastic properties group) was built to examine the influence of the elastic properties of the spinal aqueduct on the fluid pressure environment of CSF (CHAPTER 3). To satisfy the examination, three sub-group model types, one group of normal and two groups of hypothetical extreme condition models, were constructed. Four models with different dura thicknesses and stiffnesses were included in each sub-group of models. The results suggest that it is the dura's elastic properties that play the key

role in determining the pressure propagation wave speed; the spinal cord elastic properties have little effect on this.

Numerous studies have proposed that the appearance of an obstruction (stenosis) within the CSF pathway in the SAS will somehow cause a higher intracranial pressure, and that high pressure was suggested to be one of the causes of syringomyelia, a specific disease in which a fluid-filled cyst forms in the spinal cord. It has been proposed by many neurosurgeons that the higher intracranial pressure caused by the stenosis forces the fluid to enter the central cord and then form or distend the syrinx. In order to examine this hypothesis, six models (Post-traumatic group) were constructed. Four of the models, having a rigid dura, were built to study the pressure and displacement under different pathology conditions: normal spinal system, stenosis present, syrinx formed after the stenosis appeared, and post-surgery condition after the stenosis is removed. Two other models were constructed with distensible dura to examine the influence of elastic properties of the dura on this specific pathology. Two different excitations, a normal periodic waveform to simulate CSF pulsation and a transient impulse to mimic coughing were conducted on the models. The results confirmed elevated longitudinal pressure dissociation and transmural pressure could be caused by the stenosis. And results and conclusions made from these analyses are consistent with and lend further insight into the *in vivo* and *in vitro* results and hypotheses.

## CHAPTER 1

### INTRODUCTION AND ANATOMY BACKGROUND

Pathogenesis of various diseases from a biomechanics perspective has been the subject of considerable engineering research. An engineering approach provides quantitative support to traditional pathology analyses. In-silico investigation, an engineering analysis method developed with the computer evolution, has been adopted by more and more engineers to simulate the real biomechanical environment in the human body. This thesis is focused on in-silico analysis of cerebrospinal fluid (CSF) pressure wave propagation in the spinal subarachnoid space (SAS), and a particular disease called syringomyelia, which is proposed to be related with the CSF pressure changes in SAS.

When the spinal tissue material properties change or obstruction occurs in the spinal canal, CSF pressure propagation in the SAS will be changed in response. Certain pathologies, like syringomyelia, might appear because of these changes. Syringomyelia is a neurological disease in which a fluid-filled cystic cavity, or syrinx, forms in the spinal cord (SC), resulting in progressive loss of sensory and motor functions, and/or pain in the patient. Ever since the discovery of this disease, many neurosurgeons have devoted effort to find out the etiology and treatment for this disease. Although hypotheses on the origins of syringomyelia vary widely, it has been primarily accepted that biomechanical forces in the spinal system play a dominant role in the initiation and/or progression of this disease.

In recent years, understanding the origin of syringomyelia has received attention from engineers. Significant contributions have been made to examining the relation of biomechanical forces in the spinal system with the disease, which includes application of mathematical theory (Carpenter et al., 2003, Cirovic et al., 2005 and 2009), numerical modeling (Loth et al., 2001, Bertram et al., 2005 and 2008), and *in vitro* phantom models (Martin et al., 2005 and 2008). The goal of this thesis is to build a series of *in silico* models to study the pressure environment and displacement in spinal system in various pathologies under different excitation. The models were constructed nearly identical to the *in vitro* models built by Martin et al., for validation of the computational models..

## 1.1 Vertebral Column Anatomy

The **Vertebral column**, commonly known as the backbone or spine, is a segmented spinal column that encloses and protects the spinal cord and supports the head. Together with the sternum and ribs it forms the skeleton of the trunk of the body.

In human anatomy, the vertebral column makes up about two-fifths of the total height of the body, and is composed of 33 bones called vertebrae. According to the curves of the vertebral column, the vertebrae are divided into five groups (Figure 1-1 ):

***Cervical:*** C1-C7, convex forward, contains seven vertebrae in the neck;

***Thoracic:*** T1-T12, concave forward, adjacent to cervical, contains 12 thoracic vertebrae;

***Lumbar:*** L1-L5 contains five lumbar vertebrae that support the lower back;

***Sacral:*** contains the sacrum, is one bone consisting of five fused sacral vertebrae;

**Coccygeal:** one bone (sometimes two bones), which consists of four fused vertebrae

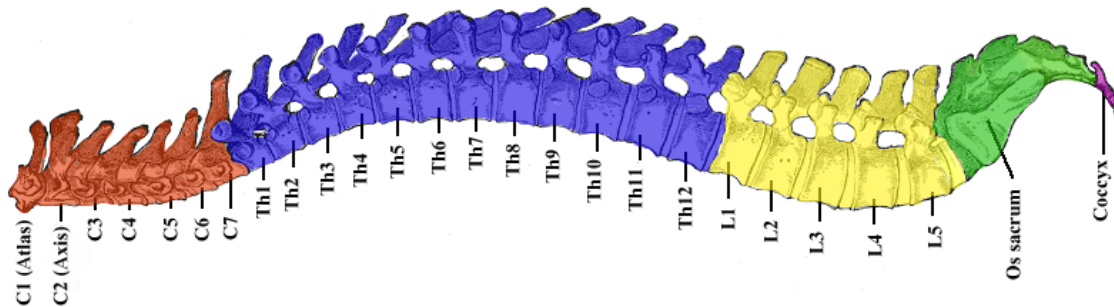


**Figure 1-1: Classification of vertebral column: cervical, thoracic, lumbar, and pelvic. [1]**

Typically, each vertebra consists of two parts: an anterior segment named **body**, and a posterior part named the **vertebral arch** (Figure 1-2). The Body is the thick, disk-shaped anterior portion, which is the weight-bearing part of a vertebra, protects and support the human mass contained. Its anterior and lateral surfaces contain nutrient foramina for blood vessels. The Vertebral arch, which serves as muscle attachment, encloses the vertebral foramen and supports several processes: transverse processes, spinous process, laminae, and pedicles. Together, the vertebral arch and the body of the vertebra surround the spinal cord (Figure 1-2).

Openings between vertebrae are called **vertebral foramina**. The thoracic and lumbar spinal nerves that connect the spinal cord to various parts of the body pass through the openings. Between the bodies of adjacent vertebrae from the second cervical vertebra to the sacrum are vertebral discs (Figure 1-2). A vertebral disk serves to absorb shock on the spine, permit various movements of the vertebral column, and forms strong joints. Under compression, they flatten, broaden, and bulge from their inter-vertebral spaces. Superior to the sacrum, the vertebral discs constitute about one-fourth the length of the vertebral column [2-5].

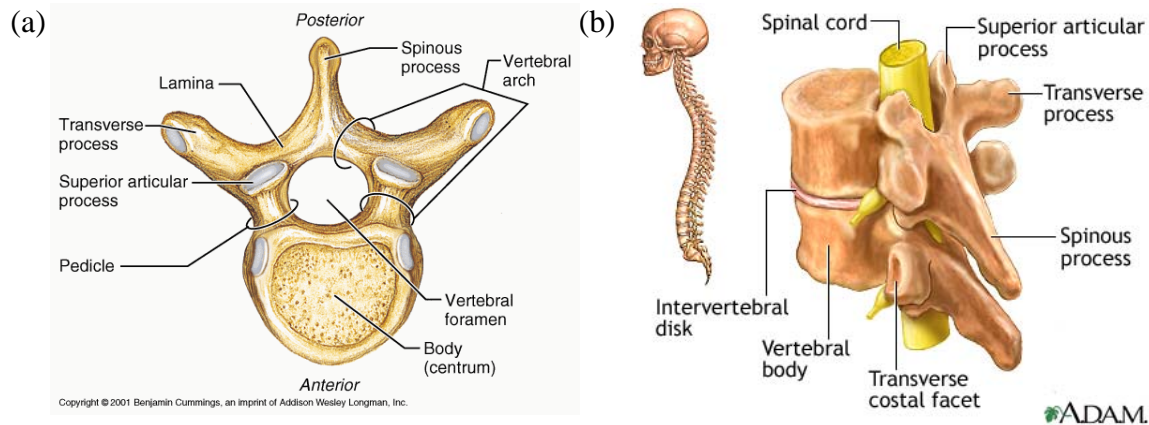


**Figure 1-2: Diagram of vertebrae. (a): traverse section view of vertebrae [6] (b) left posterolateral view of articulated vertebrae [7].**

## 1.2 Meninges

The **meninges** are the system of membranes that are connective tissue coverings that encircle the central nervous system. The meninges consist of three layers: the dura mater, the arachnoid mater, and the pia mater (Figure 1-3).

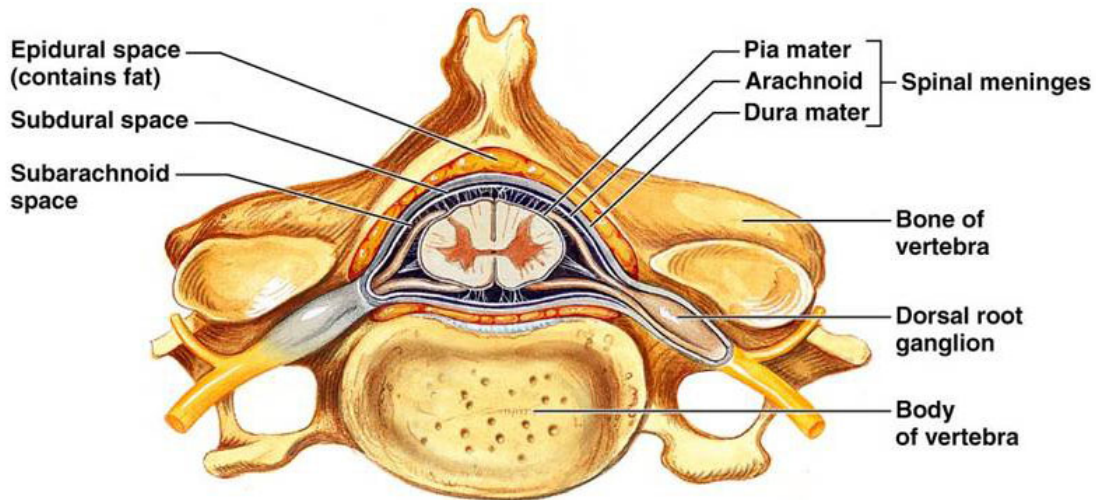
The **Dura mater** is the most superficial layer, which is a thick, durable membrane. It contains larger blood vessels which split into the capillaries in the pia mater. It is composed of dense, irregular connective tissue, and forms a sac from the level of the foramen magnum in the occipital bone. The dura mater surrounds and supports the large venous channels carrying blood from the brain toward the heart.

The **Arachnoid mater** is the middle meninx that is an avascular covering. It's so named because its spider web-like appearance. It provides a cushioning effect for the central nervous system. Between the dura mater and the arachnoid is a thin **subdural space**, which contains interstitial fluid.

The innermost meninx is the **pia mater**, which is a very delicate, thin and transparent membrane. It firmly adheres to the surface of the brain and spinal cord. It contains many blood vessels that supply oxygen and nutrients to the spinal cord.

Between the arachnoid and the pia mater is the **subarachnoid space (SAS)**, which contains cerebrospinal fluid (Figure 1-3) [3].

If the spinal cord experiences trauma, a web-like scar tissue can form, called arachnoiditis, which can be a cause of syringomyelia [8].



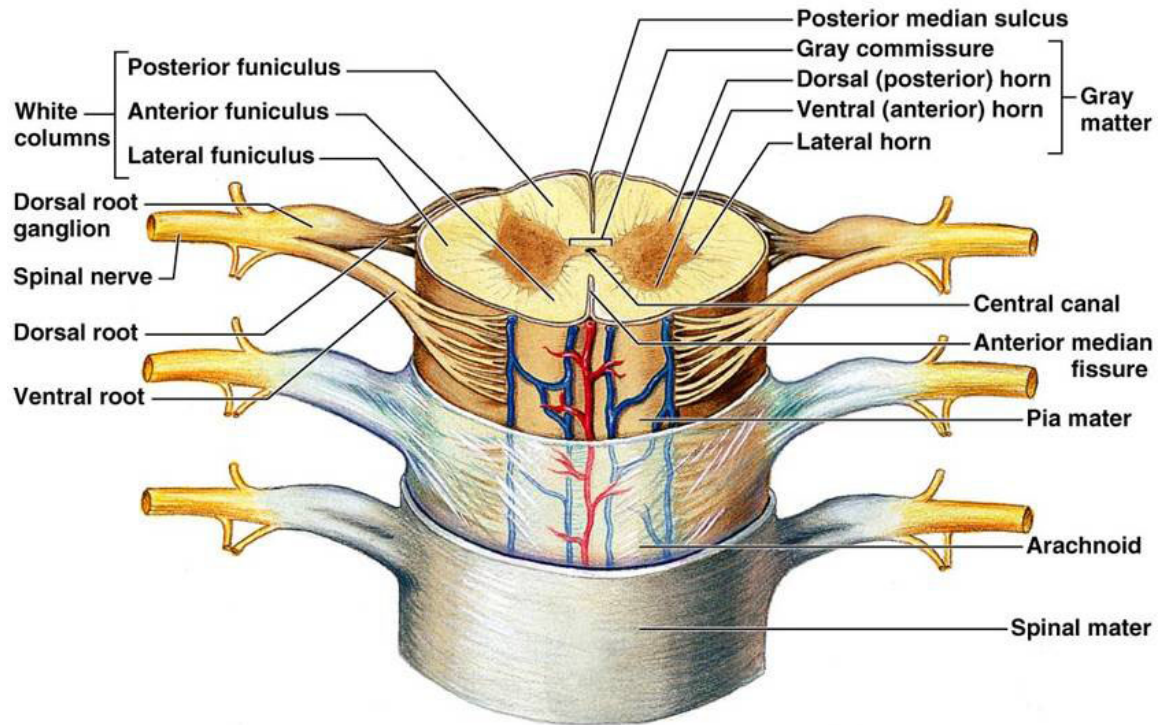
Copyright © 2006 Pearson Education, Inc., publishing as Benjamin Cummings.

**Figure 1-3: Transverse section of spinal cord [6]. Spinal cord meninges are denoted in the figure.**

### **1.3 Spinal Cord Anatomy**

The **spinal cord**, a long, thin, tubular bundle of nervous tissue and support cells, is protected by two types of connective tissue coverings – bony vertebrae and tough meninges – plus a cushion of **cerebrospinal fluid**, which will be introduced in more detail in section 1.4. The spinal

cord extends from the brain down to the space between the first and second lumbar vertebrae, and does not extend the entire length of vertebral column [9].



Copyright © 2006 Pearson Education, Inc., publishing as Benjamin Cummings.

**Figure 1-4: Transverse section through spinal cord [6].**

Figure 1-4 is a cross-section of the spinal cord. Viewed from the cross-section, the spinal cord is composed of two regions: neuronal **white matter** tracts that contain sensory and motor neurons and surround the **gray matter**, a butterfly-shaped central region, which is made up of nerve cell bodies. And, in the center of the spinal cord, surrounded by the gray matter, the **central canal** is a cavity that is an atomic extension of the spaces in the brain containing cerebrospinal fluid [3].

Together, the spinal cord and the spinal nerves mediate the body's quick reaction automatically to environmental changes. **Spinal nerves** are the paths of communication between the

spinal cord and the nerves innervating specific regions of the body. Nerves stretch from the spinal cord outward between individual vertebrae into various locations in the body. If the spinal cord is pinched, various symptoms can be caused depending on which nerves are compressed [3].

#### **1.4 Cerebrospinal Fluid and the Subarachnoid Spaces**

**Cerebrospinal fluid (CSF)** is a colorless bodily fluid that circulates continuously through the cavities within the brain and spinal cord, and around the brain and spinal cord in the subarachnoid space (SAS). Figure 1-5 shows how the CSF circulates in the system.

CSF is produced in the brain by modified ependymal cells in the choroid plexus, and the remainder is formed around blood vessels and along ventricular walls. Normally, CSF is reabsorbed as rapidly as it is formed, at a rate of about 20mL/hr (480mL/day). Because the rates of formation and reabsorption are the same, the pressure of CSF normally is constant.

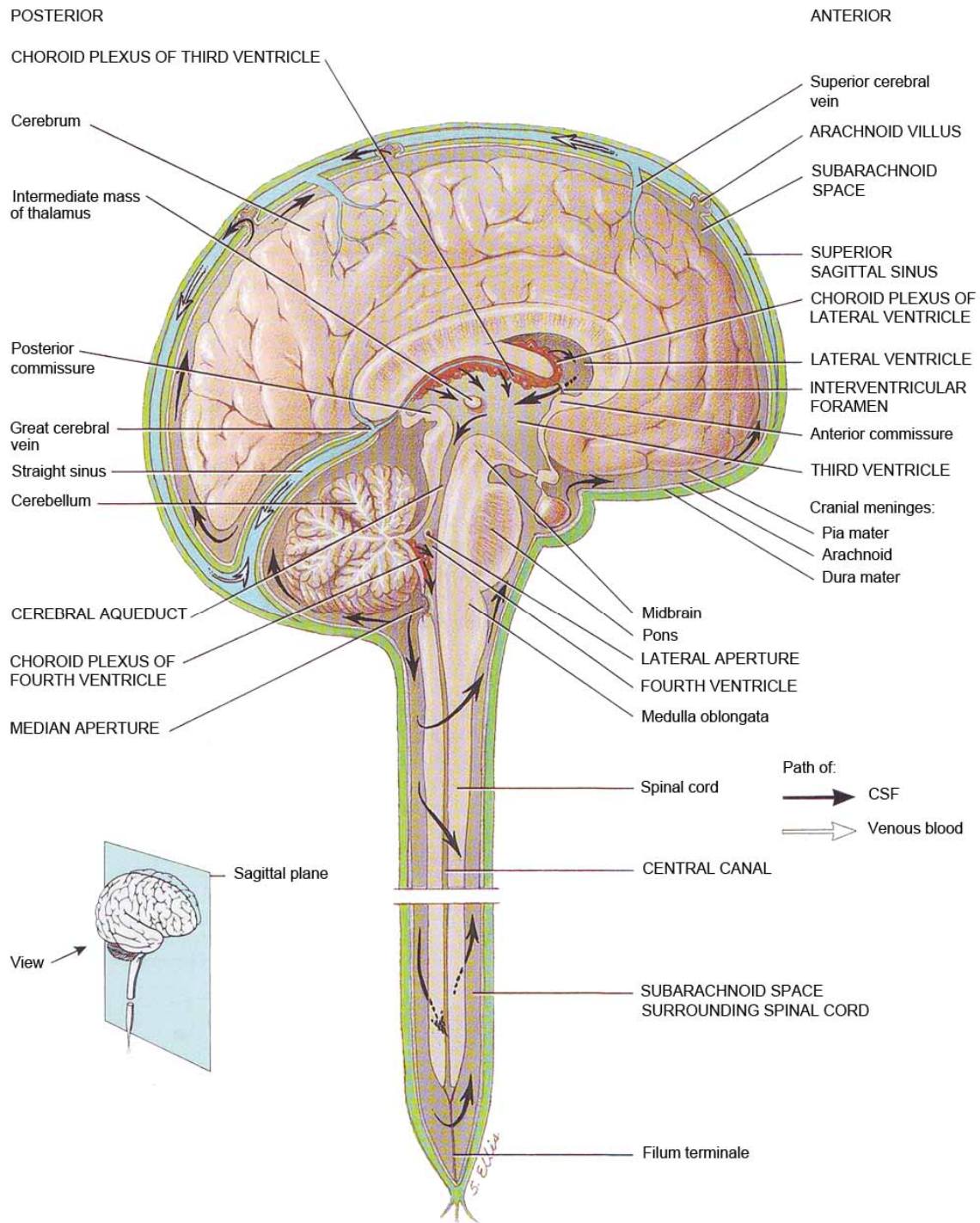


**Figure 1-5: Pathway of cerebrospinal fluid circulation [3]**

To keep the chemical stability, CSF provides an optimal chemical environment, carries oxygen, glucose, and other need substances from the blood to neurons and neuroglia, for accu-

rate neuronal signaling. And with the circulation, CSF also serves as a medium for exchange of nutrients and waste products between the blood and nervous tissue.

The CSF acts as a shock-absorbing medium, providing a basic mechanical and immunological protection to the brain and spinal cord from jolts. Various pathological conditions can be caused by or associated with the obstruction of CSF flow[3, 10-11]. And, the particular disease studied in this thesis, syringomyelia, is widely accepted among these conditions.

### 1.5 Syringomyelia

Syringomyelia generally refers to a neurological pathology where one or more fluid-filled cysts are present in a patient's spinal cord, see Figure 1-6.

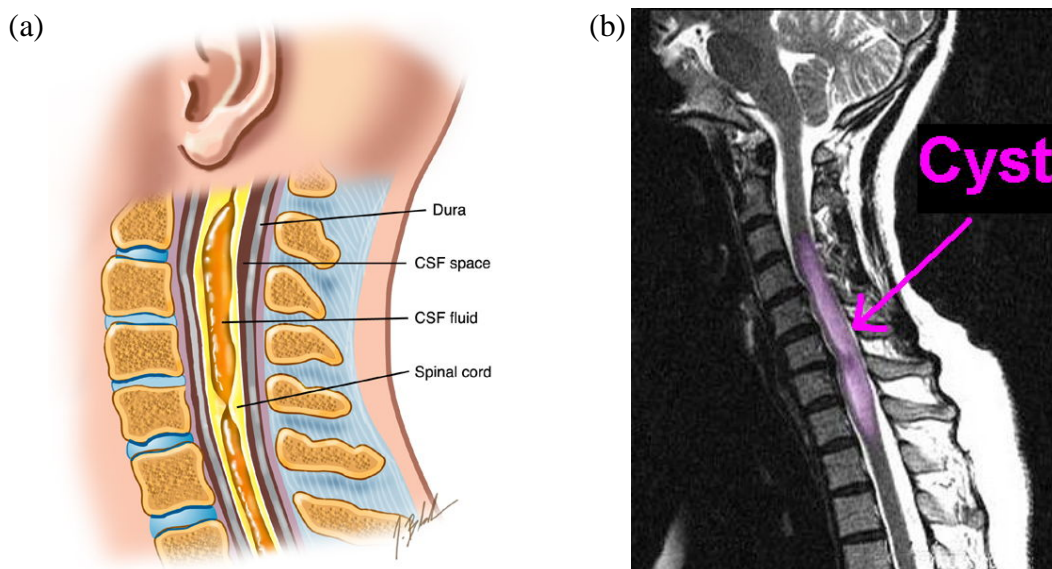


**Figure 1-6: Syringomyelia (a) diagram of syrinx formed in spinal cord. (b) MRI image of a syrinx formed in the spinal cord. [12]**

Although in a restricted definition, this pathology is distinguished as syringomyelia, hydromyelia, or myelomalacia, classified based on characteristics of the cyst and how it affects the spinal cord. [13]. As one of the pathologies associated with blockage in CSF flow in the spinal

canal, the pressure wave propagation under the condition of syringomyelia will be one specific case studied in this thesis.

Further distinguished by whether the syrinx is open to the CSF-filled cranial ventricles and SAS via the small central canal of the spinal cord, syringomyelia can be divided into two types: communicating and non-communicating syrinxes. The most common condition of this disease – Arnold-Chiari malformation (ACM), named after the physician who first characterized it, is one of the types of communicating syringomyelia. Arnold-Chiari malformation is an abnormality in which the anatomic malformation causes the lower part of the cerebellum to protrude into the spinal canal (see Figure 1-7). A syrinx then might develop in the cervical region of the spinal cord.

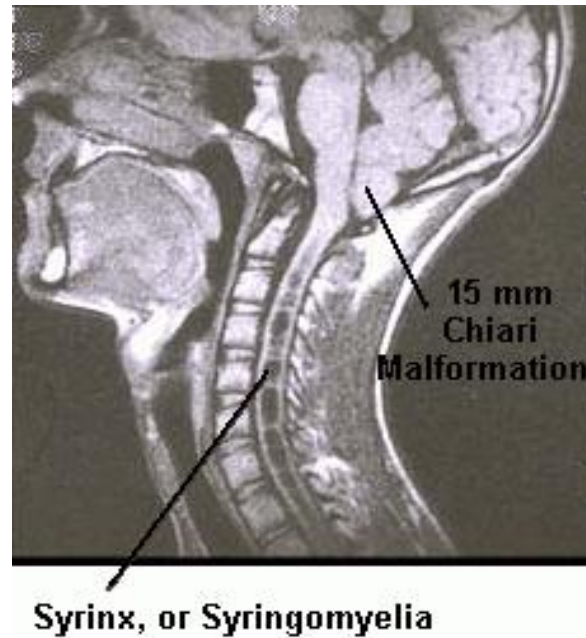


**Figure 1-7: Sagittal MRI of head of sub-cranial subarachnoid space of a patient with Arnold-Chiari malformation and Syringomyelia [14]**

Most of the cases of Arnold-Chiari malformation are congenital. ACM is delineated into four types. Types I-III are characterized by different degrees of caudal displacement of cerebellum and brainstem into the spinal canal; type IV consists of cerebellar hypoplasia. The type I Arnold-Chiari malformation (ACMI) is the most common malformation, and also the one most often associated with syringomyelia. Studies show that 75-85% of patients with ACMI will develop syringomyelia [13]. This is also the prototype of the syringomyelia model in this thesis.

Syringomyelia has been known for almost five centuries, and has been widely noticed for more than 250 years. In the USA, estimates of the number vary widely, but a conservative estimation is that about 40,000 people are affected, with symptoms usually beginning in young adulthood [15].

### **1.5.1 Symptoms and Diagnosis**

The symptoms of syringomyelia vary widely due to the various locations of the syrinx in the spinal cord that affect the localized branching nerves in different ways. Symptoms of syringomyelia usually develop slowly over time. The first symptoms tend to appear in the fingers and then spread. It is common to have a loss of sensation that spreads like a cape over the shoulders and back. Late in the condition, the affected individual may have spastic muscles or weakness of the legs. Other symptoms may include headaches, loss of reflexes, loss of sensitivity to pain and temperature. Syringomyelia may also adversely affect sweating, sexual function and bladder and bowel control [2, 15-16]

Apart from clinical analysis, modern imaging techniques such as MRI and phase-contrast cine MRI offer the opportunity to diagnose syringomyelia easily. Besides MRI, the physician may order additional tests to help confirm the diagnosis, like electromyography (EMG), which measures muscle weakness; or perform a lumbar puncture to test CSF pressure and analyze the CSF [16].

### **1.5.2 Treatment and Prognosis**

Symptoms typically begin between the age of 25 to 40, and can worsen with high activity and flexion of the spinal column that results in CSF fluid pressure fluctuation in the SAS [5, 15]. If the syringomyelia is caused by Arnold-Chiari malformation, symptoms may begin during the patient's teenage years or early adulthood. In some cases, a fall, minor trauma, coughing or straining may trigger symptoms of syringomyelia, although none of these causes syringomyelia [17].

Surgery is the only viable treatment for syringomyelia. But not all patients will advance to the stage where surgery is needed. Surgical treatment is aimed to correct the condition that allowed the syrinx to form. In some patients it may be necessary to drain the syrinx, which can be accomplished using a system known as a shunt, which includes a catheter, drainage tubes, and valves. Shunts are used in both the communicating and non-communicating forms of the disorder. However, drainage of a syrinx does not necessarily mean the elimination of the syrinx-related symptoms, but rather is aimed at stopping progression. Different treatment strategies have to be implemented for different pathophysiological entities described above. In cases involving ACMI,

a decompression surgery which is also called suboccipital craniectomy will typically be performed. The main goal of surgery is to provide more space for the cerebellum without entering the brain or spinal cord.

Recurrence of syringomyelia after surgery may make additional operations necessary; these may not be completely successful over the long term.[13, 15-16].

### **1.5.3 Causes, Theories, and Existed Engineering Models**

Over the years, various theories have been made in attempting to explain the variable manifestations and associated conditions of syringomyelia, and many of these theories overlap each other. From the etiologic aspect, the theories fall under two categories: theories of congenital origins and theories of acquired origins. However, either condition is associated with blockage in normal CSF flow within the SAS (a stenosis) .

Normally, cerebrospinal fluid flows in a pulsatile manner throughout the SAS. This pulsatile movement of the CSF within the SAS is one of the reasons for the phase difference in influx and outflow of blood within the cranial vault. Because the cranial cavity is nearly rigid, for a healthy adult, the net flow is nearly zero when the CSF pulsation moves into the more compliant spinal canal during each cardiac cycle.

However, it has been observed that, obstruction, or blockage in the normal CSF flow within SAS (stenosis) can result in the formation of syrinx. Once the syrinx is formed, pressure differences along the spine are considered to be one cause of fluid movement within the cyst and further damage to the spinal cord and connecting nerves. Obstruction of the normal CSF flow can

be caused by various pathological conditions, which are classified into two forms: congenital malformation such as most cases of Arnold-Chiari malformation, and acquired conditions including trauma to the spinal cord, meningitis, arachnoiditis, tumors, or spinal cord scarring [13, 15-16]. In the case of scarring, the spinal cord is usually said to “tether” to the adjacent dura mater, thereby blocking CSF flow in the SAS adjacent to the scar area [5, 13]. Figure 1-8 shows a rare case of temporary Arnold-Chiari malformation and syringomyelia which was caused by a car accident head injury. After the injury healed in two month, the syrinx almost disappeared. Which is one proof of the relation between the blockage and syringomyelia.

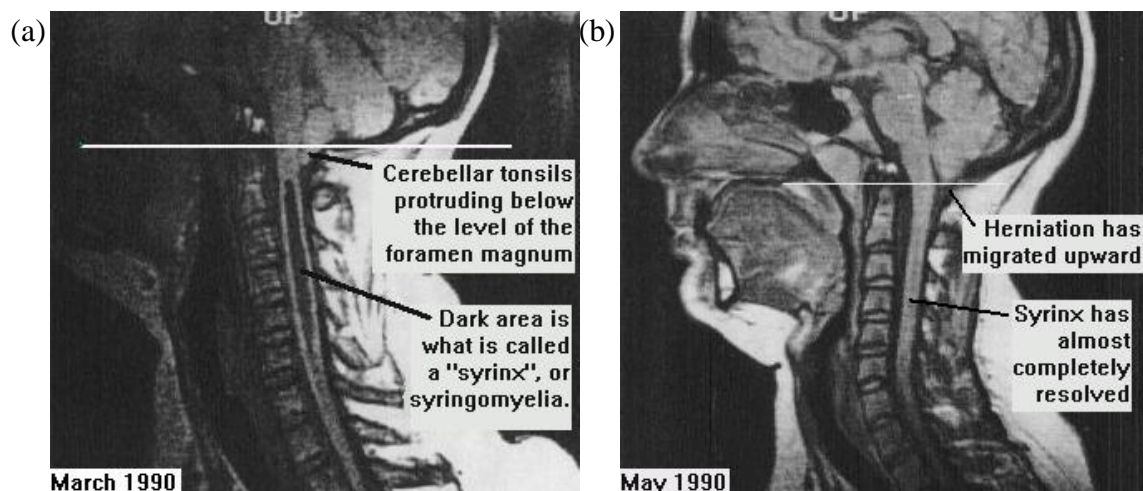


**Figure 1-8: A case of a temporary ACM/ syrinx: 28 yr old female with a car accident head injury, and after the injury healed, the ACM/syrinx almost disappeared. Source- W.C. Clivero and D.H. Dinh, Neurology, v. 30, #5, 758 (1992).Submitted by Bernie H. Meyer [18]**

In addition to the origins of syringomyelia, another question that has been raised is that if the CSF is not produced inside the spinal cord, how does it get into the syrinx? In 1862, Gull proposed a hydrodynamic theory in syringomyelia for the first time, but inadequate autopsies led Gull to give up his theory. The theory was reconsidered by Lichtenstein in 1942. And in 1956,

after examining 17 cases of the Arnold-Chiari I malformation, Gardner published an explanation associating syringomyelia and Arnold-Chiari malformation in terms of a hydrodynamic mechanism.

In Gardner's theory, he claimed that all cases of syringomyelia were due to a patent communication between the fourth ventricle and the central canal. This statement provoked a lively debate and was not fully agreed to by the majority at that time. In his theory, he studied the embryological development of the central nervous system, and then described syringomyelia as a dilatation of the central canal due to increased intracranial pressure, which forced CSF to enter the central canal via the obex. The driving force was thought to be a water hammer effect of the choroid plexus. This pathophysiological concept is similar to Arnold-Chiari's ideas on the development of subtypes of Arnold-Chiari malformation [2, 13, 19].

In 1969, Williams challenged Gardner's theory by emphasizing the important role of CSF flow obstructions in the formation of syringomyelia, which is the fundamental contribution to our present understanding of syringomyelia. In Williams' theory, he asserted that partial CSF flow obstructions led to longitudinal pressure dissociation. He proposed that a sudden increase of SAS pressure caused by coughing, sneezing, or Valsalva maneuvers will increase the intracranial pressure, which forces CSF through a patent central canal into the Syrxinx. Williams also referred to cranial-spinal pressure dissociation as "suck", which describes a dilatation of a syrxinx caused by the rebound downward movement of the CSF resulting from the pressure gradient between the intracranial and intraspinal following a valsalva maneuver. He mentioned that, when asking

patients to cough or blow into a mouthpiece, this pressure differential can be measured by recording the pressures simultaneously from both the ventricle and the SAS. He noted that in patients with hindbrain hernia, pressure differences of over 100 mmHg could be recorded between the head and the spine. And Williams also proposed a term “slosh” to describe the surges in pressure that could happen to intrasyinx, to explain the progression of the syrinx cavity in the cases of non-communication with the fourth ventricle [5, 13, 19-21].

In 1994, Oldfield et al. further modified the pressure dissociation by emphasizing the importance of a rapid downward motion during systole of cerebellar tonsils in Arnold-Chiari I malformation patients. Based on the dynamic MRI and intraoperative ultrasound studies, they demonstrated that abrupt downward movement of the cerebellar tonsils during systole was synchronous with sudden constriction of the spinal cord and syrinx. Based on these studies, they proposed that the “piston-like” effect of the movement of the impacted tonsils during systole produces an accentuated systolic pressure wave to the SAS CSF flow, abruptly constricting the surface of the cord and underlying syrinx. The CSF is therefore forced into the spinal cord expanding the syrinx. And, same as Williams’ theory, Oldfield et al. also confirmed the impact of coughing or severe straining. They emphasized that their proposed mechanism for the progression of syringomyelia required no communication with the fourth ventricle; this is different from the hydrodynamic theory proposed by Gardner [5, 13, 19].

Based on observation after intrathecal injections of water-soluble contrast media, Ball and Dayan raised another theory by proposing that flow of contrast along extracellular pathways

(so-called Virchow-Robin spaces) into the cord provided a block of CSF flow, causing a sufficient increase of SAS pressure. Pressure recordings in the SAS and syrinx cavities also resulted in higher pressure in the syrinx than in the surrounding SAS [5, 13].

Based on all of the above, various hypotheses have been made on the causes of syringomyelia. Though the theories are different from each other, it is commonly accepted that the CSF pressure in SAS plays an important role in the formation of syrinx. But without experiment and analysis based on the principles of mechanics, these hypotheses cannot be proved. In recent years, engineers began to notice the divergent theories on syringomyelia, and have developed various mathematical models, numerical models and *in vitro* models to prove and develop new theories on syringomyelia.

Motivated by Williams' "suck" and "slosh" theory, Carpenter et al. published a series of papers proposing a mathematical model to study pressure propagation in the human, intraspinal, CSF system. Their inspiration came from Williams' experiment of recording CSF pressure in the lumbar and cisternal (top of the neck) region during repeated coughs. The shape and maximum amplitude of the pressure in a healthy person did not differ much in the two locations, while in contrast, for patients with syringomyelia, the cisternal pressure was extremely weak and attenuated compared with the lumbar one. These observations suggested that the pressure wave propagation is almost non-dispersive for healthy person, but inhibited by the partial or complete blockage in the SAS present with syringomyelia.

Based on Williams' study and on the classic theory of longitudinal waves in fluid-filled elastic tubes and channels, Carpenter developed a co-axial tube system to mimic the human intraspinal CSF system, and made assumptions that allowed them to formulate an axisymmetric quasi-one dimensional theory. Then pressure wave propagation along this co-axial fluid-filled elastic tube and deformation of the elastic tubes were examined in this system. From their study, it was concluded that a compressive pressure wave due to a cough or sneeze could form a shock-like elastic jump. And the elastic jump depends on the change of the cross-section area greatly. When the compressive pressure is incident at a stenosis, where the cross-section areas of the tubes differ greatly, the elastic jump will be the greatest. The great elastic jump will then causes a transient increased pressure within the spinal cord, which forces the fluid in to the SC to form a syrinx [22-23].

Since 2005, Bertram et al. have conducted a series of numerical investigations on the pressure wave propagation in the spinal column, especially in the case of syringomyelia. Bertram's models are built with the finite element fluid/structure-interaction code ADINA (ADINA R&D Inc., Watertown, MA, USA). In these models, by motivation of Carpenter's theory, Bertram assumed the presence of a significant reflecting site at one end of the CSF flow due to arachnoiditis. In his 2005 paper, Bertram built a series models studying the wave speed in conditions of different elastic properties of dura and spinal cord, and drew a conclusion that the central canal does not influence the wave propagation significantly. Then in 2009, Bertram published another paper in studying the wave propagation in the spinal cord and SAS in the presence of a syrinx. In this

paper, Bertram built models to investigate William's "slosh" theory that SAS pressure waves move fluid along a syrinx and can thus lengthen it over time by tissue dissection. And his results suggest that "slosh" may not generate sufficient force to lengthen a syrinx [24-26].

Rather than study the pressure distribution in the spinal canal, Cirovic et al. focused their interest in the wave propagation speed in a co-axial system filled with incompressible media such as arteries and the spinal column. In 2009, Cirovic published a paper with a mathematical co-axial spinal column model, with which derived the characteristic equation to calculate the wave speed transmission in the spinal canal. And wave equations for three different conditions, elastic dura and spinal cord, rigid dura, and rigid spinal cord, were also derived in the paper [27-29].

In 2009, by building a simplified co-axial theoretical model, Martin et al. published a paper deriving new equations of wave propagation speed in the spinal column, and applied the equation to verify their *in vitro* models. Martin et al.'s equations will be used for verification of the *in silico* result of wave speed in this thesis [30-31].

Since 2005, Martin et al. have constructed a series of *in vitro* models simulating various spinal system circumstances. These experiments provide detailed and compelling evidences of the pressure distribution in the spinal system. The results of these *in vitro* experiments proved some theories above. From the results, the elastic properties of the spinal cord were proved to not play a key role in determining the wave speed in the SAS. The stenosis, blockage in CSF flow

within SAS, was proved to be one of the major reasons in causing the formation of syrinx [5, 32-34].

To study the pressure environment in the spinal cord, including the presence of a stenosis and syrinx, a series of *in silico* models will be built in this thesis to simulate the *in vitro* models built by Martin et al. But several more model types beyond the *in vitro* models were constructed in this thesis to study more pathology and for comparison. And the *in vitro* results will be used for validation in this thesis.

## CHAPTER 2

### FINITE ELEMENT MODELS CONSTRUCTION AND DEFINITION

As introduced in the last chapter, Martin et al. (2005) have built a series of *in vitro* models to mimic the spine, especially the syringomyelia system. *In vitro* models provide detailed practical information on the CSF pressure flow in SAS. However, they require construction for each specific mechanism and parameter variation. *In silico* models, on the other hand, provide detailed and comprehensive information on the CSF pressure flow as well as other parameters of interest. It also offers a much more convenient way to make analyses of various mechanisms and geometries.

In this thesis, a series of *in silico* models will be constructed with the finite element code ANSYS (ANSYS Inc., Canonsburg, PA). In order to validate the *in silico* results by Martin et al.'s *in vitro* results, the models are built to be almost identical to Martin et al.'s *in vitro* models. In this chapter, basic and general parameters, definitions, and information for these models will be introduced.

#### 2.1 Model Definition

The spinal column system as well as the syringomyelia condition can be viewed as a coaxial elastic tube system. To simplify the analysis, the models are built as 2-D axisymmetric systems. Based on Martin et al.'s *in vitro* study and different spinal canal conditions, *in silico* models are constructed in two groups. The definition, geometry and other detailed information for each

model will be introduced in the following sections. The abbreviations of the models for each group are given as the following:

**Elastic properties group:** models for investigating the influence of elastic properties of the spinal aqueduct on the pressure wave propagation in SAS:

- ***CSD (Spinal cord, SAS and Dura model):***

representative of a healthy spinal column with normal dura and spinal cord.

- ***CLSD (Cordless System with SAS and Dura model):***

hypothetical model with spinal cord removed.

- ***CRSD (Cord System with Rigid Spinal Cord and Normal Dura model):***

hypothetical model with a rigid spinal cord and normal dura.

**Post-traumatic group:** models for investigating the influence of blockage (stenosis) and/or syrinx on pressure propagation in the spinal system.

- ***CSRD (Spinal cord, SAS and Rigid Dura model):***

hypothetical model, similar to model CSD, but with rigid dura.

- ***SAE (Stenosis Alone Experiment model):***

representative of patient with a spinal stenosis formed in the spinal canal, and with a nearly rigid dura.

- ***SSE (Stenosis and Syrinx Experiment model):***

representative of a syringomyelia patient with a moderate sized syrinx formed after a spinal stenosis appeared in the spinal canal, and with a nearly rigid dura.

- ***SRE (Stenosis Removed Experiment model):***

similar to SSE, but with the stenosis removed and leave the syrinx alone in the spinal cord.

- ***SSED (Stenosis and Syrinx Experiment model with Distensible spinal column):***

similar to SSE but the dura was replaced with a flexible and thicker material.

- ***SRED (Stenosis Removed Experiment with Distensible spinal column):***

similar to SRE but the dura was replaced with a flexible and thicker material.

## **2.2 Element Definition**

In finite element analysis, the element type can be typically categorized into two groups: linear or quadratic. For the 2-D analysis, which is applied in this thesis, a 4-node quadrilateral element is a pure linear element, which is often degenerated into a 3-node triangular element for complex geometries. And, an 8-node quadrilateral element is the most popular quadratic element in which additional nodes are added at the center of each edge. For complex geometry, an 8-node quadrilateral element can also be degenerated to a 6-node triangular element. Typically, a higher order element provides a higher rate of convergence.

Based on the fundamental category of elements above, ANSYS classifies the elements in more detail, and provides hundreds of different element types for different analysis and material type. Table 2-1 gives the ANSYS element type chosen for these *in silico* models and the material used in the *in vitro* models assigned to each component.

**Table 2-1: Element Definitions and Material in the *In vitro* Models for Each Component**

Spinal Component	<i>In vitro</i> model material	Element Type	ANSYS Element Type
Dura(1)	Polymer (Sylgard)	2D 4-Node Solid	Plane 182
Dura(2)	Glass	2D 4-Node Solid	Plane 182
SC	Polymer (Sylgard)	2D 4-Node Solid	Plane 182
SAS Flow	Water	2D Contained Fluid	Fluid 79
Syrinx Flow	water	2D Contained Fluid	Fluid 79
Stenosis	Rubber	2D 4-Node Solid	Plane 182

**Note: (1): Elastic group models; (2): Post-traumatic group models.**

In the spinal system, to keep the balance of the metabolism, the volume of CSF in the spinal system always keeps constant. Thus, to simplify the calculation, ANSYS element type Fluid 79 is chosen to represent the CSF fluid in these models. Fluid 79 is a 2-D contained fluid element which is a modification of 2-D structural solid element. This element is used to model fluids contained within vessels having no net flow rate. Fluid 79 is a four node element in which two degrees of freedom are defined at each node: translation in x and y direction. The geometry, node locations and the coordinate system of Fluid 79 is shown in Figure 2-1 [35].

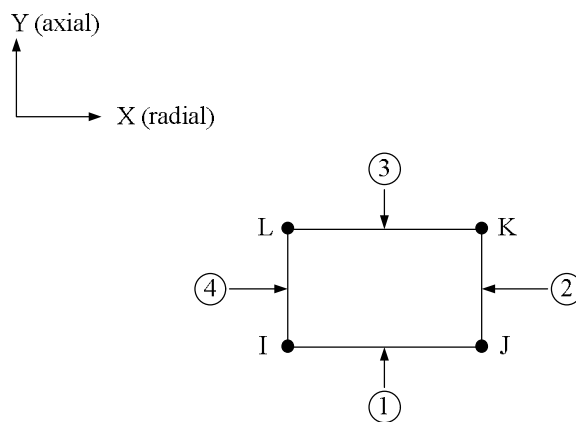


**Figure 2-1: Geometry, node locations, element face index and coordinate system of element Fluid 79[35]**

In finite element analysis, to ensure the analysis results converge to the exact solution, the finite element method should be both compatible and complete. Therefore, although a higher or-

der element with eight nodes has a higher rate of convergence, only four node solid elements can be assigned to the solid components in these models because the already defined fluid element Fluid 79 is a four node element. Otherwise, when meshing a 4-node element with an 8-node element (which has additional nodes in the center of the edges) together, a gap can occur, as shown in Figure 2-2, because the displacement interpolation is quadratic on one side and linear on the other side. Such a gap is a discontinuity in the displacement field.

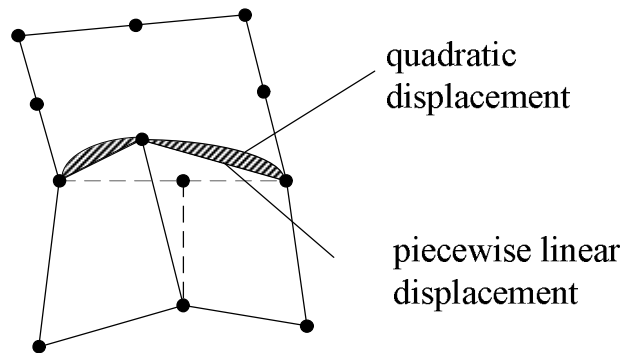


**Figure 2-2: A gap could occur when an 8-node element meshes with 4-node element, because a deformed mesh may be curved along the 8-node element edge, while the 4-node elements have linear edges.**

Both the dura and spinal cord are viscoelastic materials. Especially the spinal cord, which is soft tissue, can be viewed as nearly incompressible. So, the ANSYS element type Plane 182 is chosen for the solid components in these models. Plane 182 is a 2-D 4-node structural solid element. Same as Fluid 79, Plane 182 has two degrees of freedom at each node: translation in the x and y directions. The geometry and node locations for this element are shown in Figure 2-3. Plane 182 has plasticity, hyperelasticity, stress stiffening, large deflection, and large strain capabilities. It also has mixed formulation capability for simulating deformations of nearly incompressible elastoplastic materials, and fully incompressible hyperelastic materials [35].

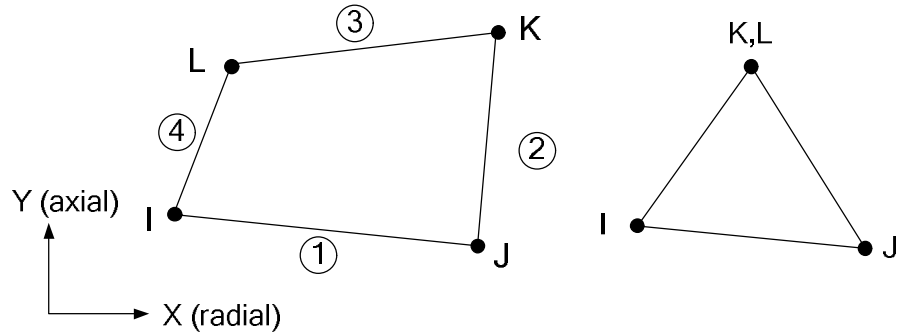


**Figure 2-3: Geometry, node locations, element face index and coordinate system of Plane 182**

### 2.3 Material Properties

In order to match Martin et al.'s (2005) *in vitro* experiments, the material properties are defined based on the *in vitro* models, shown in Table 3-2 in Section 3.2 and Table 4-2 in Section 4.2.

#### Cerebrospinal Fluid

CSF is contained within the SAS in the spinal system and also within the syrinx in syringomyelia. CSF is a clear Newtonian fluid having viscosity nearly that of water [5]. Thus, in the *in vitro* experiments, water was used to represent CSF. So the physical properties of CSF, including bulk modulus, viscosity, and density, are as same as water. For a healthy human, a normal body temperature is 37 °C; the dynamic viscosity of water at certain temperature can be calculated with equation:

$$\mu(\text{Pa} \cdot \text{s}) = A \times 10^{\frac{B}{T-C}}$$

where  $A = 2.414 \times 10^{-5} \text{ Pa} \cdot \text{s}$ ,  $B = 247.8 \text{ K}$ , and  $C = 140\text{K}$  [36]. So the dynamic viscosity of water at 37°C (or 310.15 K) is  $6.90 \times 10^{-4} \text{ Pa} \cdot \text{s}$ . From <http://www.wikipedia.org>, the density of water at 37°C is  $996 \text{ kg/m}^3$ , and the bulk modulus of water is  $2.2 \times 10^9 \text{ Pascal}$ .

## **Spinal Cord**

The spinal cords in Martin et al.'s *in vitro* models are constructed with a two part polymer mixture (Sylgard 184). Because each spinal cord was cast separately using Sylgard mixed in separate batches, the Young's modulus of the spinal cord in each model has some difference. To be consistent with Martin's models, the material properties of the *in silico* models are defined the same as the *in vitro* materials accordingly. The density of Sylgard 184 is  $1060 \text{ kg/m}^3$  [5]. The Poisson's ratio and damping value of spinal cord material in the *in vitro* models are not given in Martin's previous paper. Because spinal cord is soft tissue, which is nearly incompressible; the Poisson's ratio for the SC was set to 0.495. The damping value of the Sylgard was estimated based on the damping value of glass and a value known material – CF11. CF11 is glue has similar properties of Sylgard but softer and more viscid. The damping value of CF11 is known as 0.003. For a viscoelastic material, the damping value is proportional to the ratio of the viscosity to the stiffness of the material, so damping value of Sylgard should be lower than CF11 but higher than glass. The damping value of typical glass ranges from  $6 \times 10^{-4}$  to  $2 \times 10^{-3}$  [37]. Different combination of damping value of glass and Sylgard has been tried in this range, and the damping value 0.002 for Sylgard and 0.001 for glass has the most similar amplitude to the *in vitro* result.

## **Dura**

In all of the elastic property group models and two of the post-traumatic hydrodynamic models SRED and SSED, dura was also constructed with Sylgard 184, but with a different mix-

ture ratio from that in constructing spinal cord. So the same material properties can be applied to dura in these models. The density of dura is  $1060 \text{ kg/m}^3$ , and the Poisson's ratio of dura is set to be 0.495. The damping value in the material is independent of the mixture ratio, so the damping value of dura in these cases is same as spinal cord, which is 0.002.

In the other four post-traumatic group models CSRD, SAE, SSE and SRE, the dura was constructed with glass. Exact physical properties are not provided, but the Young's Modulus is given in range of 64~90 GPa from Martin's paper [5], so the value is chosen to be 80 GPa for the *in silico* models. For typical glass, the density is  $2400\text{--}2800 \text{ kg/m}^3$  [38], and the Poisson's ratio is 0.18~0.3 [39]. So an average value of density  $2600 \text{ kg/m}^3$ , Poisson's ratio 0.25 are chosen for the *in silico* models. And as discussed above, damping value for glass was chosen to be 0.001.

### **Stenosis**

The stenosis, which is an obstruction or blockage in the normal CSF flow, was created by a tough rubber material (part # 14-150-2F,  $\frac{1}{2}$ "ID  $\times$   $\frac{1}{8}$ "W  $\times$   $\frac{3}{4}$ "OD, Fischer Scientific). This rubber material is more rigid than the material used for the spinal column in SSED, and not as rigid as the glass used for SSE etc.[32]. But no exact physical properties are given from the *in vitro* models. For typical rubber material, Young's modulus is ranging from 0.01 GPa to 0.1 GPa [14], Poisson's ratio is nearly 0.5 [39], the damping value is about 0.05 [40], and density is  $1200 \text{ kg/m}^3$  for hard rubber [41]. According to these, an average Young's modulus value of 50 MPa, Poisson's ratio of 0.45, damping value of 0.01, and density of  $1200 \text{ kg/m}^3$  are chosen for the *in silico* models.

## 2.4 Dimensions

As a quasi-coaxial system, the spinal system is built into an axisymmetric geometry in ANSYS to simplify analysis. The models are constructed almost identical to the *in vitro* models built by Martin et al., and the dimensions are defined based on Martin's *in vitro* models.

Based on statistical data and MR images of the sagittal view of patients used for obtaining *in vitro* model geometry, in Martin et al.'s models, the length of the spine is defined as 48 cm, corresponding to the average length of healthy adults' spine. The diameter of spinal cord is 10 mm, the outer diameter of the SAS (the inner diameter of dura) is 15.6 mm. The syrinx in syringomyelia cases is a tapered structure, whose diameter ranges from 7 mm to 3.2 mm, referred to the average value of the MR image. The length of the syrinx is 132 mm in the *in vitro* models, with a straight part of 103 mm and a tapered part of 29mm long. The stenosis blocked more than 90% area of the SAS [5], from equation  $\frac{\pi(R_{dura}^2 - R_{stenosis}^2)}{\pi(R_{dura}^2 - R_{SC}^2)} > 0.9$ , the inner diameter of the stenosis should be less than 5.346 mm, so a value 5.3 mm was chosen here for the inner diameter of stenosis, which blocked 91.4% of the SAS area. More detailed geometries and dimensions for each model can be found in Table 3-1 in Section 3.2 and Table 4-1 in Section 4.2.

## 2.5 Mesh

In ANSYS, Fluid 79 has to be meshed in a rectangular shape [35]. The length of the model is long relative to the radial dimensions. Three different element size were examined in the samTo examine the models more precisely, an element size of 0.5 mm is chosen for all components in the models. For models with stenosis (SAE, SSE and SSED) the length between stenosis

and spinal cord is only 0.3 mm. To examine the models better, the element in this region was meshed in dimension 0.1 mm x 0.5 mm. Figure 2-1 gives an example of mesh in region stenosis in model SSE, which includes the mesh in the following components: dura, spinal cord, CSF in syrinx, stenosis, and CSF flow in SAS.

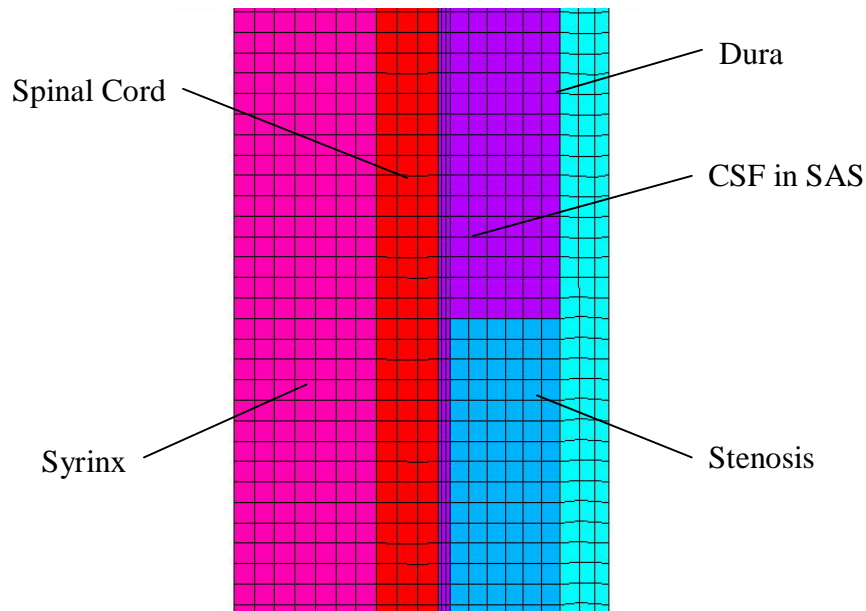


**Figure 2-4: An example of mesh in region of stenosis in model SSE.**

## **2.6 Boundary Conditions**

In ANSYS, 2-D elements must lie in an X-Y plane. Additionally, to do an axisymmetric analysis, the Y-axis must be the axis of symmetry, and an axisymmetric structure should be modeled in the +X quadrants, and usually, the Y-axis is oriented in the vertical direction with the top surface at  $Y=0$  [35]. So the models are built in the (+X, -Y) quadrants, and symmetric about the vertical axis on the left-hand side (Y-axis). That means on the symmetric axis (Y-axis), there's no normal displacement, nodes locations on Y-axis are fixed radially.

In addition, in Martin's *in vitro* models, the diameter of the spinal cord is 10 mm; the inner diameter of the dura is 15.6 mm. When assembling the models, each end of the model was blocked off entirely by two larger diameter semi-rigid plastic pipes (19 mm OD, 8 mm ID, ~2 cm length) which were pressure fit within each end of the spinal column [5]. The boundary conditions of the *in silico* models are set to be fixed for axial displacement of solid components (SC and dura) segments at the ends. In the *in vitro* models, at the ends the inlet and outlet ports (see Figure 4-1) allow the fluid flow in and out. Thus, no constraint is set on the ends of the fluid. A scale-exaggerated plot for the simplest model, CSD, is shown in Figure 2-5 to illustrate the boundary conditions defined for these *in silico* models. Boundary conditions will also be denoted on each model's geometry plots in the corresponding chapters.

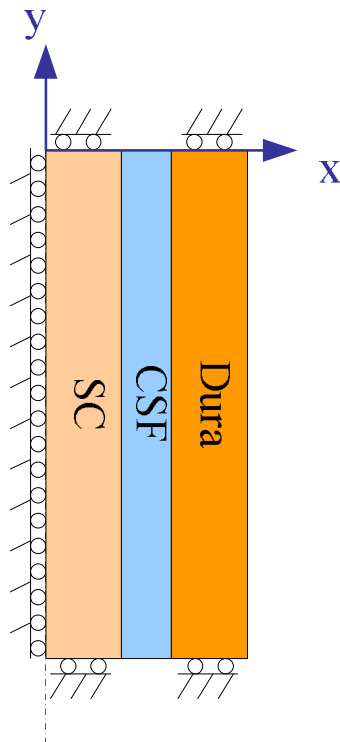


**Figure 2-5: Boundary conditions defined in the *in silico* models. The model in this figure is a scale-exaggerated CSD model. The nodes located on the Y-axis are fixed radially, and both ends of solid (dura and SC) are fixed axially.**

## CHAPTER 3

### INFLUENCE OF ELASTIC PROPERTIES OF THE SPINAL AQUEDUCT

#### 3.1 Introduction

The human body, as an organism, contains various biological tissues and biofluid conveyed inside, which interact with each other. Changes in elastic properties of biological tissues often coincide with certain diseases. So the assessment, especially non-invasive measurement, of material properties of the biological plays a key role in diagnosis as well as treatment in various pathologies. There are diverse non-invasive methods to assess material properties of biological tissues. In the case of biological systems conveying fluid, elastic property changes can influence the pressure environment, including the speed of pressure wave propagation within the fluid conduit. For example, in the vascular system, when the vessels are stiffened, pressure wave speed increases. Wave speed measurement has been used to estimate elastic properties in the aorta and femoral arteries, for example [5].

In case of the spinal cord, which is one of the bio-fluid systems mentioned above, elastic properties of the spinal aqueduct may also accompany pathology. The relation of CSF system compliance to intracranial hypertension, Arnold-Chiari malformation, syringomyelia, and other craniospinal disorders has been the subject of many studies. And in the case of syringomyelia, it has been documented that significant tissue edema, which may be caused by diseases such as sarcoidosis, occurs preceding the formation of syrinx [5]. Thus, one might expect that edema of tis-

sue (both dura and/or cord) would also be accompanied by a change in elastic properties of the tissue, and therefore would change the wave propagation speed in the spinal aqueduct.

In order to examine the influence of elastic properties of the spinal canal components on the pressure wave propagation, Martin et al. constructed a series of *in vitro* models and have made the conclusion that only the physical properties of the encasing component (dura) play a significant role in determining the wave propagation speed through the system. The wave speed was also found to be related best to the dura thickness [5].

To further understand the influence of elastic properties, similar models are constructed in ANSYS. The same conclusions are obtained from the *in silico* analysis. And, the wave speed obtained from the *in silico* result complies with the *in vitro* results.

### **3.2 Methodology**

Three groups of *in silico* elastic models are constructed in ANSYS as follows:

- ***CSD (Spinal cord, SAS and Dura model):***  
representative of a healthy spinal column with no syrinx and no stenosis present.
- ***CLSD (Cordless System with SAS and Dura model):***  
hypothetical model with spinal cord removed.
- ***CRSD (Cord System with Rigid Spinal Cord and Normal Dura model):***  
hypothetical model with a rigid spinal cord and normal dura.

CSD and CLSD are constructed based on the *in vitro* models, and CRSD is a hypothetical case. Because a conclusion was made in the *in vitro* result that the spinal cord physics properties

do not play a key role in determining the wave speed through the spine, two extreme hypothetical models CLSD, which ignored the spinal cord, and CRSD, which assumed a rigid spinal cord, are constructed to verify the conclusion. And in each model, four sub-models with different dura thickness and stiffness are built to examine how the properties of dura influence the wave propagation. Geometries and dimensions are almost the same as the *in vitro* models. General dimension information has been introduced in section 2.4, and detailed dimensions are given in Table 3-1.

**Table 3-1: Dimensions for Models in Elastic Properties Group: CSD, CLSD, and CRSD**

Model Types		Dimensions (mm)			
		Length	SAS Diameter	Dura Thickness	SC Diameter
CSD	Model 1	480	15.6	17.9	10
	Model 2			12	
	Model 3			5.2	
	Model 4			2.3	
CLSD	Model 1			17.9	/
	Model 2			12	
	Model 3			5.2	
	Model 4			2.3	
CRSD	Model 1			17.9	10
	Model 2			12	
	Model 3			5.2	
	Model 4			2.3	

The definition of the overall material properties was introduced in Section 2.3. For models in elastic properties group in this chapter, damping values are ignored to simplify the theoretical verification in Section 3.4. Detailed material properties for each model are given in Table 3-2.

**Table 3-2: Material Properties for Models in Elastic Properties Group: CSD, CLSD, and CRSD**

Model Type		Dura Thickness	Young's Modulus (Pascal)	Poisson Ratio	Density (kg/m <sup>3</sup> )	Bulk Modulus (Pascal)	Viscosity (Pa·s)
Dura	CSD, CLSD, CRSD	M1	1.99E+06	0.495	1060	/	/
		M2					
		M3	6.32E+05	0.495			
		M4					
CSF (CSD, CLSD, CRSD)			/	/	996	2.20E+09	6.90E-04
SC	CSD	M1	4.66E+05	0.495	1060	/	/
		M2					
		M3					
		M4					
	CRSD	M1	1.00E+12	0.1	1.00E+04	/	/
		M2					
		M3					
		M4					

Geometries of CSD, CRSD, and CLSD models are given in Figure 3-1. The 2-D axisymmetric models are built in the quadrant (+X, -Y), and symmetric about the Y-axis. Boundary conditions and how the excitation was applied on the models can also be found in the figure. In these models, both ends of the solid components (dura and spinal cord) are fixed axially, while ends of the fluid are set free. The models are excited by a transient pressure impulse applied at the caudal end of CSF in the SAS (Y=0). Various analyses with different excitation waveforms and time-step sizes are conducted to validate the numerical investigation.

In Martin et al.'s *in vitro* models, 10 pressure sensors are set up at 10 pressure ports along the spine with intervals of 4 and 6 cm distance to the ends to monitor the pressure. In order to be consistent with the *in vitro* models, 10 elements are selected at the same locations to obtain pressure for comparison. The location of the elements can also be found in Figure 3-1.

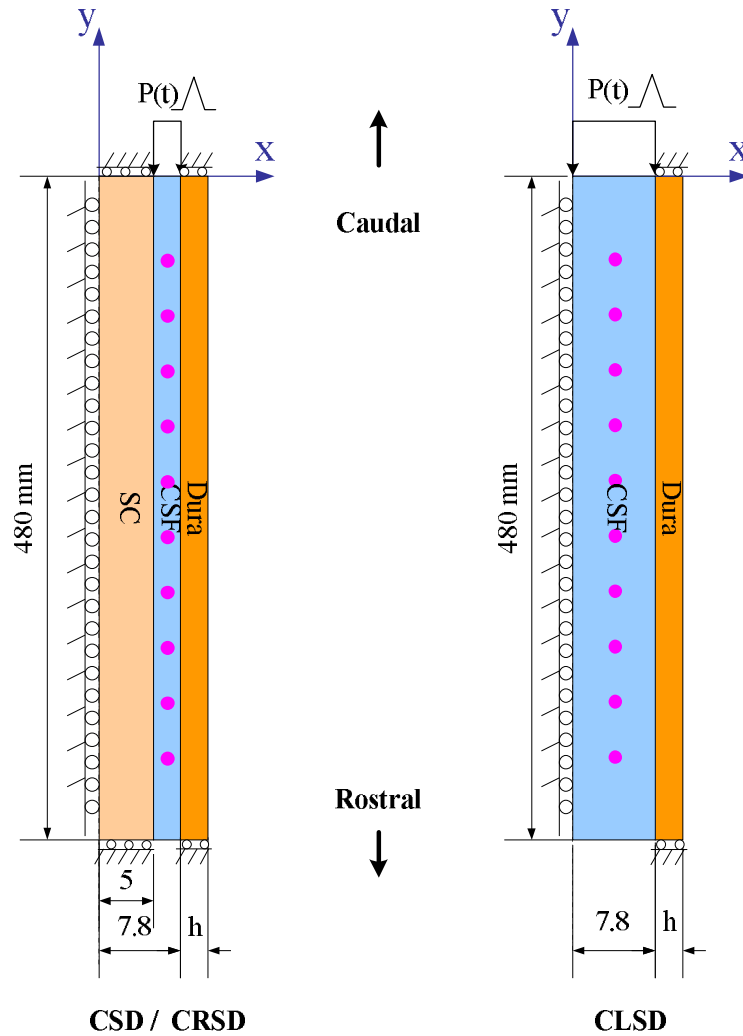


**Figure 3-1: Geometries for Model: CSD and CLSD. The horizontal to vertical scale is exaggerated. The dimensions and boundary conditions are defined based on the *in vitro* models.**

### 3.3 Results

#### 3.3.1 The influence of dura material properties on the spinal system (CSD)

First of all, to examine whether a different excitation also has a different impact on the wave propagation, CSD model 4 (CSD\_M4) is selected to be considered. CSD model 4 has a normal spinal cord and a normal dura with normal stiffness (Young's Modulus 0.632 MPa) and normal thickness 2.3 mm.

Consider first excitation of the model with a sinusoidal transient. Figure 3-2(a) shows the pressure waveform at pressure port 1 (6 cm to the excited end, solid line) and at pressure port 10 (36 cm to pressure port 1 and 6 cm to the rostral end of spine, dashed line) when a half sinusoidal excitation with duration of 100 ms (or 10 Hz frequency) was applied on the caudal end of the SAS. The input excitation transient waveform with amplitude 100 mmHg is also given in the figure (green dash line). The result was calculated at a time-step of 1 ms. From the plot, it can be found that the pressure attenuated greatly along the spine, and the pressure amplitude is about 85 mmHg lower than the input after the end of the transient input. Figure 3-2(b) shows the result (calculated at time-step of 1 ms) when the duration of the transient was reduced to 50ms (20 Hz). This time, the pressure attenuated less than the one with 10 Hz, and the pressure amplitude difference between input and after the transient end is about 55 mm Hg.

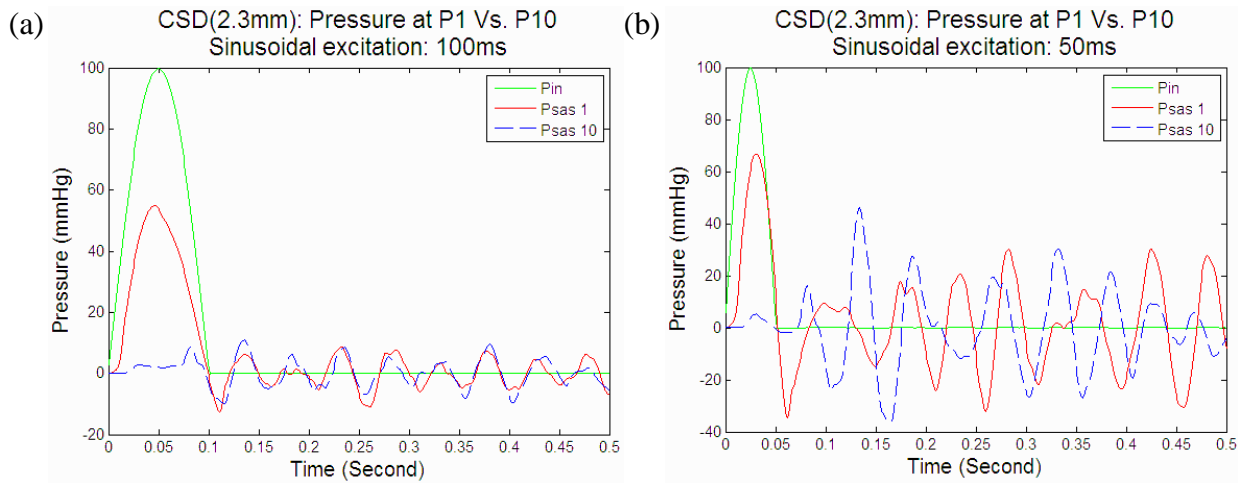


**Figure 3-2: Pressure vs. time at the pressure port 1 (close to the excited end) of the model (solid line) and at the pressure port 10 (dash line) in response to a smooth sinusoidal excitation transient of duration 100 ms (a) and 50 ms (b). Pressure transient input with amplitude of 100 mmHg is plotted as a green dash line.**

Examining the plots further, the wave propagation speeds in the two situations are same. The wave propagation speed can be calculated by dividing the distance between two points by the time interval of the wave arrives at the points, or  $c = \Delta x / \Delta t$ . From Figure 3-2, the wave arrived at the pressure ports in each excitation at the same time, although the excitation time is different. By comparing the pressure arrival time at the two pressure ports, the wave speed is about 9 m/s for both.

By plotting the pressure distribution along the spine for the whole time range, the pressure propagation can be seen much more clearly. Figure 3-3 gives the spatial vs. temporal pressure contour plots in gray level for the two excitations with duration of 100 ms and 50 ms. The pressure distribution along the SAS is meshed as a function of position and time:  $p(y, t)|_{x=k}$ , where  $p$  is pressure,  $t$  is time,  $y$  and  $x$  are radial and axial coordinates, respectively, and  $k$  is constant. In the contour plot of the pressure distribution, the pressure propagation can be seen clearly, where the shaded contours represent higher pressure. By connecting the most left edge of the shaded contour (which is the foot of wave) at the two ends of the spine, the slope of the straight line is the wave propagation speed. Comparing the two spatial vs. temporal plots of different excitation, 100 ms and 50 ms, it's not difficult to find the wave propagation speeds are almost identical. Both the strongest pressure waves left the excited end (rostral end of the spine) at 0 second, and arrived at the other end (rostral end of the spine) at about 0.085s, which means the wave speed is  $c = \frac{480\text{mm}}{85\text{ms}} = 5.65\text{m/s}$ . Therefore, the different excitation duration time changes only the width of the shaded contour, or the duration of the pressure wave.

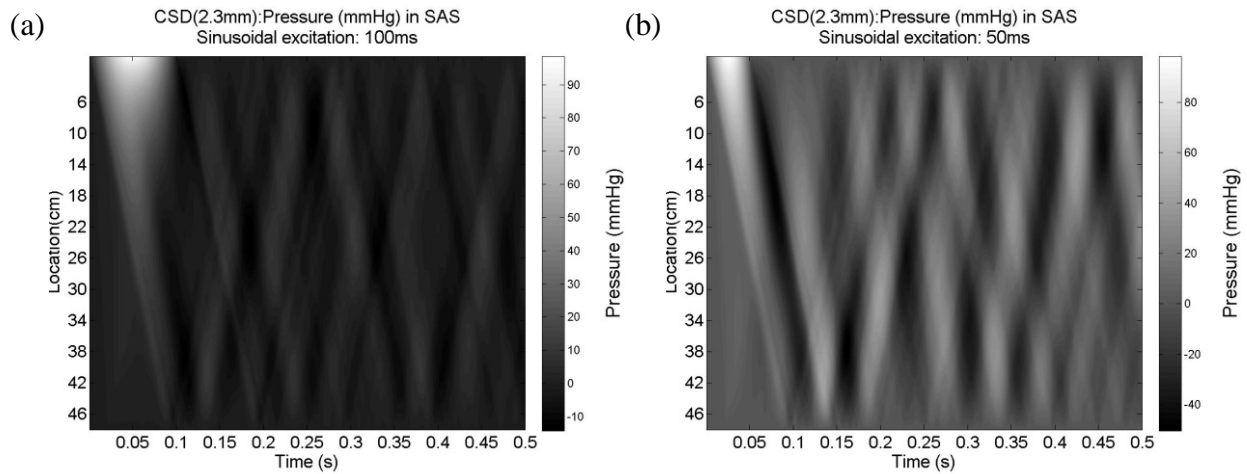


**Figure 3-3: Spatial vs. temporal pressure in SAS during the first 500 ms after the start of a sinusoidal excitation transient of duration 100 ms (a) and 50 ms (b).**

Rather than continue with sinusoidal excitation, a symmetric triangular impulse, which is easier to set up, is taken for consideration now. A transient with duration of 50 ms (20Hz) is considered first to make a comparison with the sinusoidal excitation made before. Figure 3-4 (a) gives the pressure waveform results for this excitation; the result is also calculated at a time-step of 1 ms. Comparing it with the sinusoidal result in Figure 3-2 (b), it can be found that the waveform response to triangular and sinusoidal excitation with same duration are almost identical. Next, the excitation duration is reduced to a much shorter triangular impulse of 5 ms (20 Hz) and time-step of 0.5 ms correspondingly. Figure 3-4 (b) give the resulting pressure in SAS in this case. The pressure response now is much more complicated than that with 50 ms excitation. The first pressure peak at pressure port 1 happened at about 0.006 second; the second and also the predominant peak happens at about 0.015 second with a pressure difference of about 30 mmHg to the excitation pulse. After then, the pressure at pressure port 1 became nearly flat. The predominant pulse at pressure port 10 happens quite late relatively at about 0.085 ms.

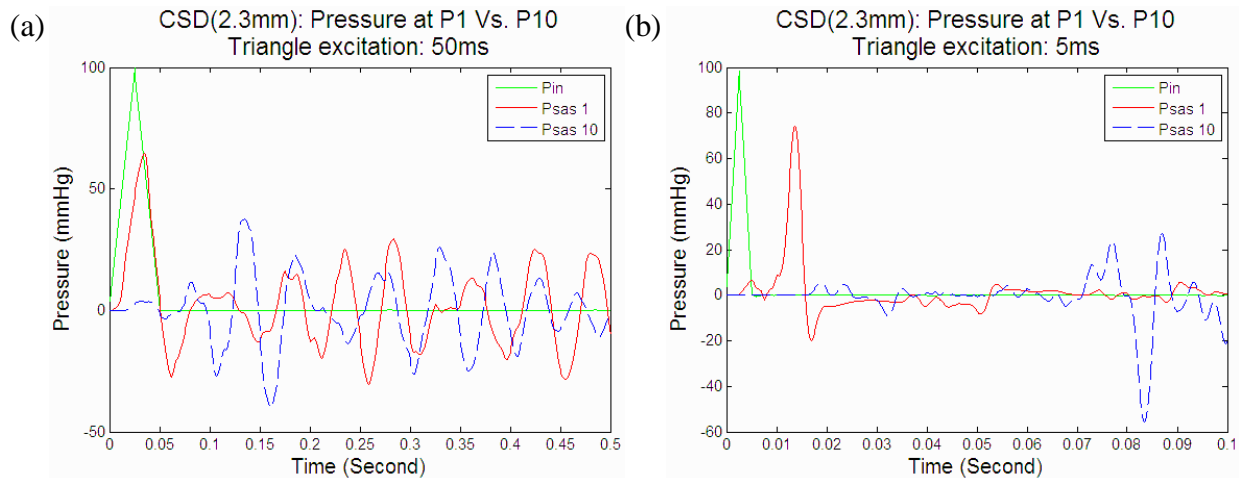


**Figure 3-4: Pressure vs. time at the pressure port 1 (close to the excited end) of the model (solid line) and at the pressure port 10 (dash line) in response to a symmetric triangular impulse of duration 50 ms (a) and 5 ms (b). Pressure transient input with amplitude of 100 mmHg is the green dash line.**

Same as before, the spatial vs. temporal plot of pressure distribution in the SAS in these two cases are given in Figure 3-5. The wave speeds in the two cases are same as in the cases excited by the sinusoidal transient. In Figure 3-5 (b), a clearer view of how pressure propagates along the spine can be seen. Three primary pressure waves can be distinguished in the plot. The fastest wave, which is also the weakest one, arrives at the other end (rostral end) of the spine at about 0.02 s, which means the wave speed of this pressure wave is 24m/s. The second fastest wave, which is also the strongest one, arrives at the rostral end of the spine at about 0.085 s, which means the wave speed of this wave is 5.65m/s. The third fastest wave is also a stronger pressure wave, which arrived at the rostral end only 5 ms later than the second wave. These results comply with both the theory and *in vitro* result, which are listed for comparison in Table 3-3. The reflection of the pressure waves can also be seen clearly in Figure 3-5 (b).

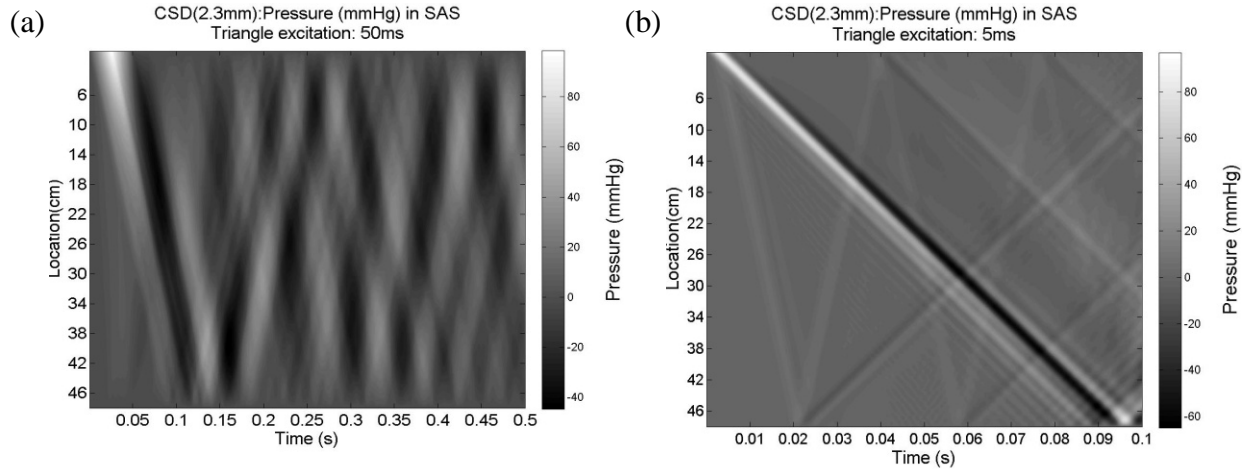


**Figure 3-5: Spatial vs. temporal pressure result in SAS after a triangular excitation is applied. (a) Pressure during the first 500 ms after the start of a triangular transient of duration 50 ms. (b) Pressure during the first 100 ms after the start of a triangular transient of duration 5 ms.**

From analysis above, the wave propagation, especially the wave speed does not change as a result of different excitation waveforms. So, a symmetric triangular transient with duration of 5 ms will be used for the following analysis.

To examine how the material properties of the dura influence the spinal system more CSD models are constructed with different stiffness and thickness. Figure 3-6 gives the pressure result when increasing the dura thickness to 5.2 mm, but with no changes in the stiffness (Young's Modulus 0.632 MPa). Figure 3-6 (a) shows the pressure changes over time at the pressure port 1 and pressure port 10. The maximum pressure reached at about 78 mmHg at port 1 and -60 mmHg at port 10. Figure 3-6 (b) is the spatial vs. temporal pressure result along the spine. The fastest wave arrived at the other end of the spine at about 0.017 ms, and the second fastest wave arrived at the spine at about 0.06 ms. So the wave speeds in this case is  $c_1 = \frac{480}{17} = 28.2 \text{ m/s}$ , and  $c_2 = \frac{480}{60} = 8 \text{ m/s}$ .

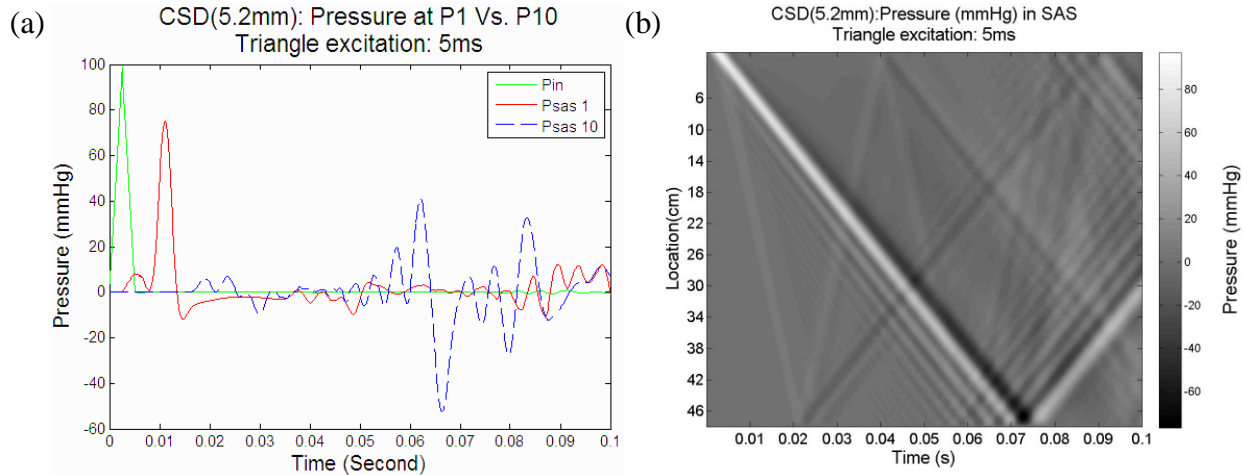


**Figure 3-6: Pressure result for CSD model with 5.2 mm dura in response to a 5 ms triangular impulse during the first 100 ms. (a) Pressure vs. time result at pressure point 1 (solid line) and pressure point 10 (dash line). (b) Spatial vs. temporal pressure result in SAS along the spine.**

From the two excitation results above, it can be found that the dura thickness does impact the wave speed: a thicker dura causes faster wave propagation. But, what happens when increasing both stiffness and thickness of the dura? Figure 3-7 shows the result when the dura thickness was increased to 12 mm, and the stiffness was increased to 1.99 MPa. From Figure 3-7 (a) the maximum pressure amplitude in this case was decreased to 50 mmHg, which is almost 1/3 decreased from the case when dura thickness was 5.2 mm, and the Young's modulus was 0.632 MPa. The wave speed can be calculated from Figure 3-7 (b). Three primary waves can be found in this plot. The fastest wave became too weak to be seen clearly; it arrived at the rostral end of the spine at about 0.012 second. The second and the third wave became the strongest waves, and arrived at the rostral end of the spine at about 0.021 second and 0.042 second respectively. Therefore,  $c_1 = 40 \text{ m/s}$ ,  $c_2 = 24 \text{ m/s}$ , and  $c_3 = 11.4 \text{ m/s}$ . An interaction of the reflected wave from the fastest wave and the second fastest wave can be found at position 44 cm, 0.02

second. Similarly, more interaction of reflected waves and transition waves can be seen at 36 cm, 0.038 second etc.

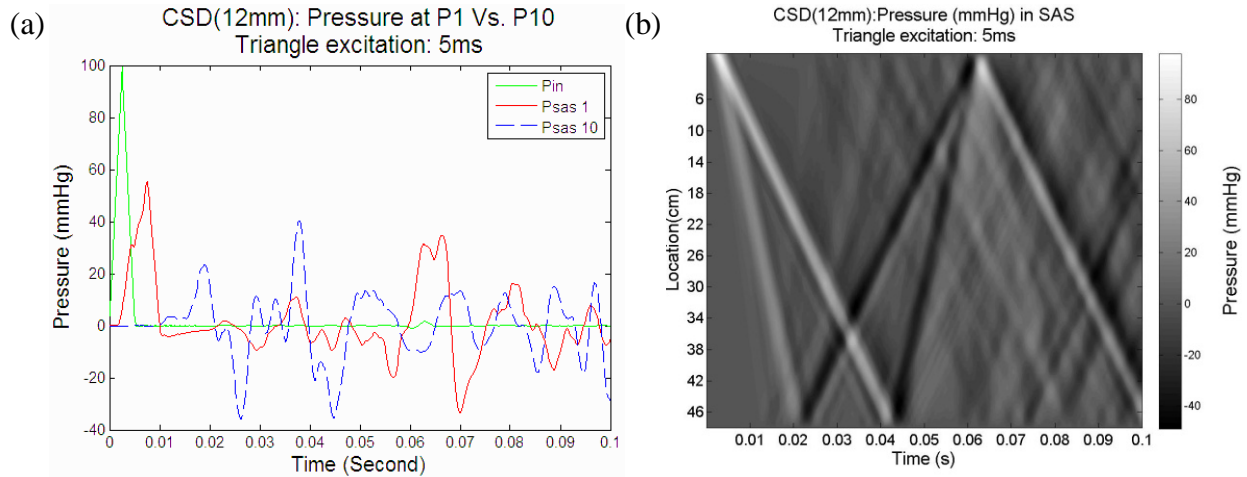


**Figure 3-7: Pressure result for CSD model with 12 mm dura in response to a 5 ms triangular impulse during the first 100 ms. (a) Pressure vs. time result at pressure point 1 (solid line) and pressure point 10 (dash line). (b) Spatial vs. temporal pressure result in SAS along the spine.**

Now, results are shown in Figure 3-8 when increasing the dura thickness to 17.9 mm but keeping the same stiffness. The maximum pressure amplitude decreased comparing to the case with the 12 mm dura, and now the weakest wave can barely be seen in Figure 3-8 (b). But, an interaction of its reflected wave and the second fastest wave can still be seen at about 0.02 s, 46 cm. The second and third waves can still be seen clearly in this case, arriving at the rostral end of the spine at 0.019 and 0.041 seconds. To see the first wave more clearly, the pressure plot in the first 20 ms is extracted and shown in Figure 3-9. Three primary waves can be seen in the plot now, where the fastest one is the weakest one arriving at the rostral end of the spine at about 0.012 second. Therefore, the first two wave speeds in this case are  $c_1 = 25.26 \text{ m/s}$ , and  $c_2 = 40 \text{ m/s}$ .

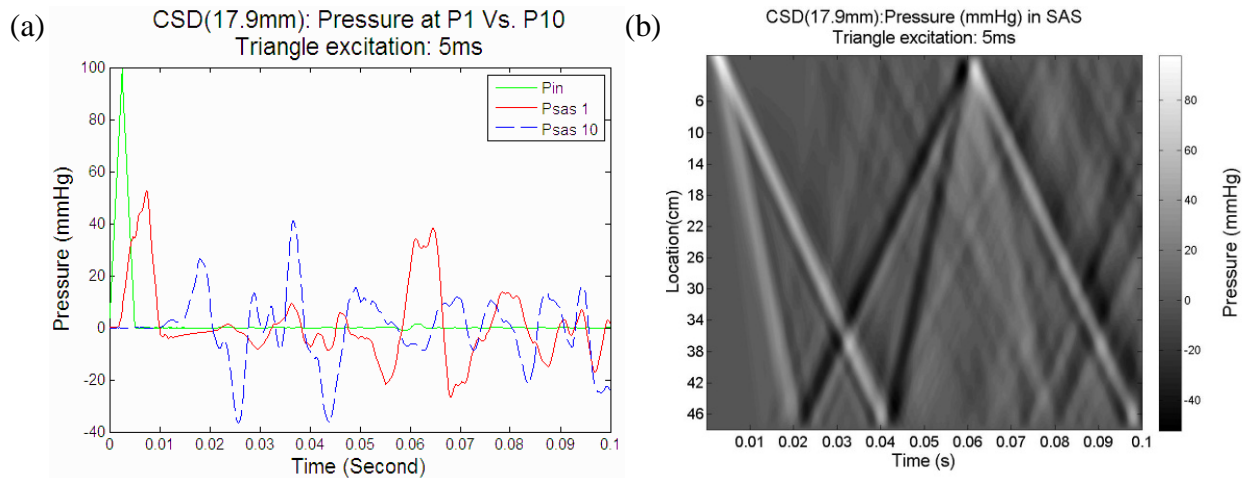


**Figure 3-8: Pressure result for CSD model with 17.9 mm dura in response to a 5 ms triangular impulse during the first 100 ms. (a) Pressure vs. time result at pressure point 1 (solid line) and pressure point 10 (dash line). (b) Spatial vs. temporal pressure result in SAS along the spine.**

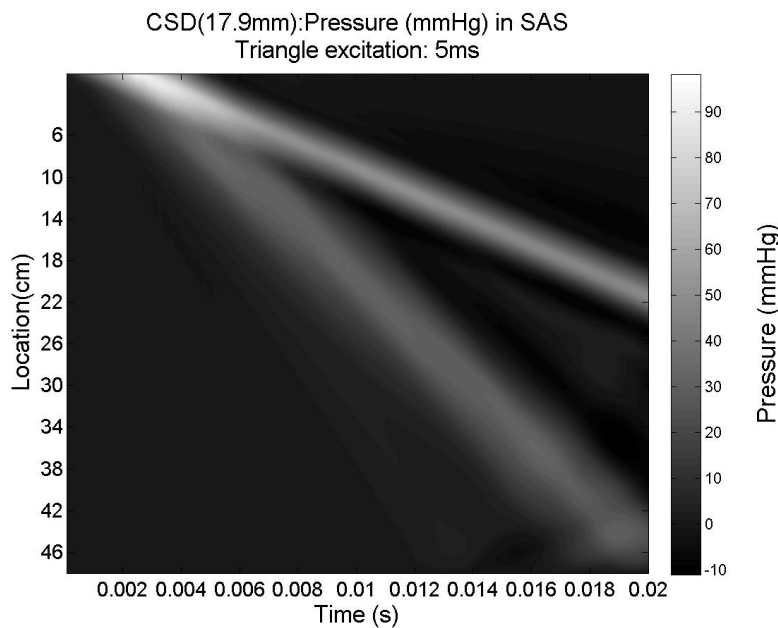


**Figure 3-9: Pressure result for CSD model with 17.9 mm dura in response to a 5 ms triangular impulse during the first 20 ms. The first three waves can be seen in the figure; the fastest wave is the weakest one arriving at the rostral end of the spine at about 0.012 second. Interaction of the reflection of the first wave and the second wave can also be seen in the plot.**

Comparison of the wave speeds in different cases is found in Table 3-3. From the results above, the wave speed is related to the stiffness and the thickness of the encasing material (dura).

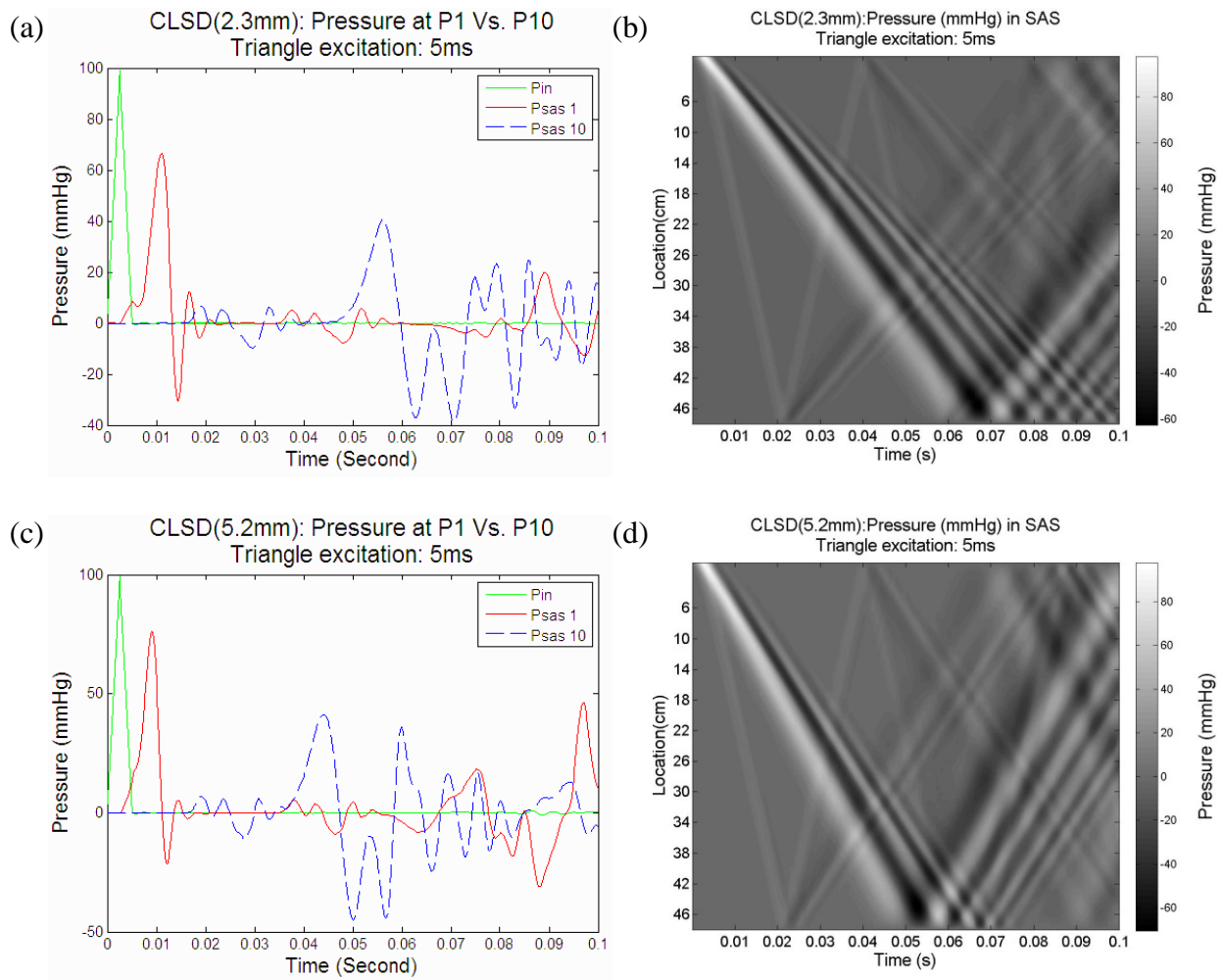
The thicker and the stiffer the material is, the faster the wave speed will be. On the other hand, the pressure amplitude in the flow aqueduct is related to the stiffness of the encasing material more. In cases of the 2.3 mm dura and 5.2 mm dura, which have the same stiffness, the maximum pressure amplitudes don't have much difference. However, when the stiffness increased, the maximum pressure amplitude decreased about 20 mmHg, while there was not much difference between the 12 mm dura and 17.9 mm dura cases, which had the same stiffness.

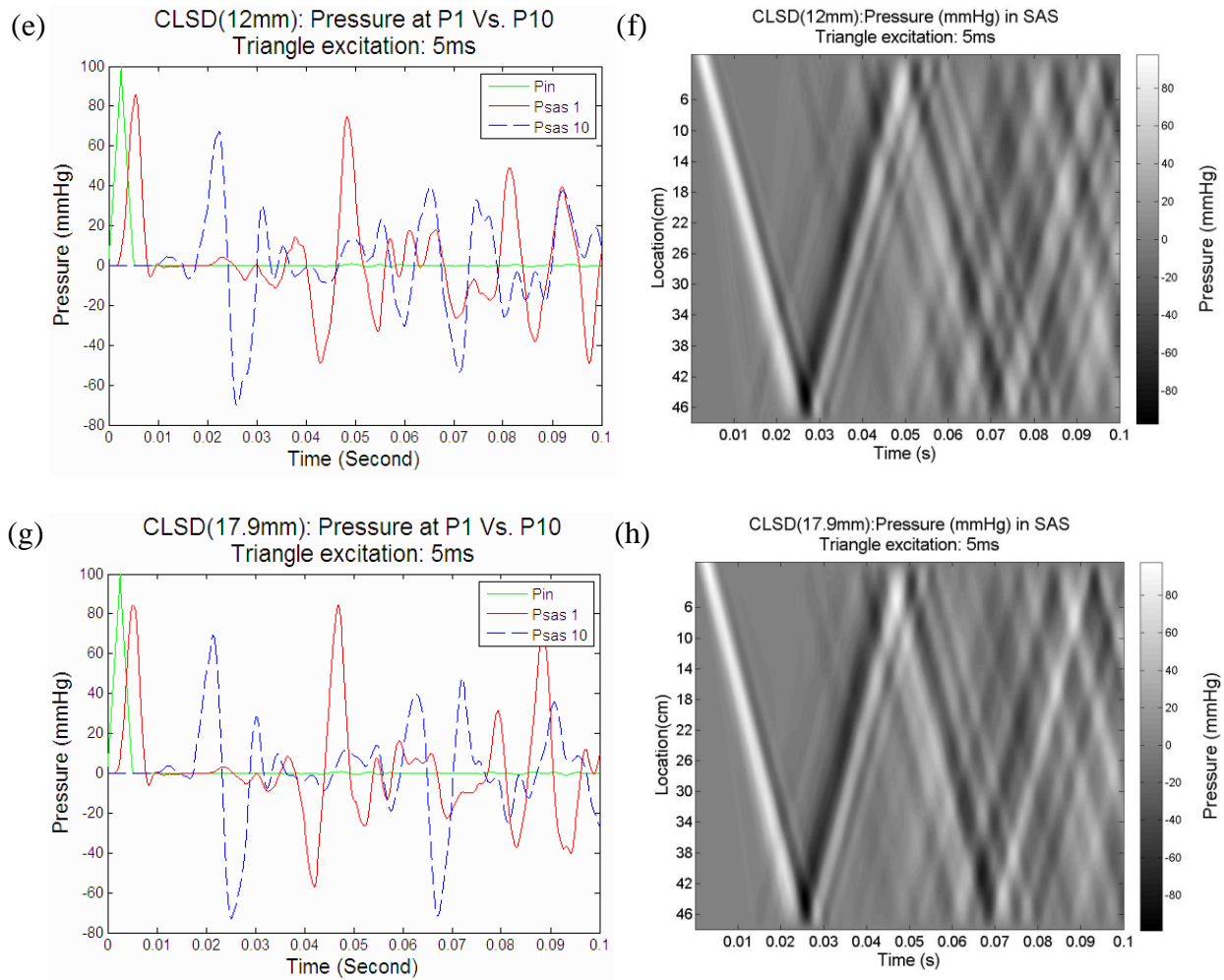
### **3.3.2 The influence of spinal cord on the spinal system (CLSD and CRSD)**

The influence of the dura properties has been shown in the above analysis. In this section, the influence of spinal cord properties on the spinal aqueduct will be examined. Two extreme assumptions of cordless and with rigid cord will be made to show that spinal cord does not play a key role in determining the wave propagation speed in the SAS.

First of all, the whole spinal cord is completely removed from the system (CLSD models). Figure 3-10 gives the pressure result for cordless models with the same dura thickness and stiffness assumption as the CSD models. Figure 3-10 (a), (c), (e), and (g) are the pressure vs. time result at pressure port 1 and port 10 for different dura assumptions. The pressure amplitude does not change much when the dura became thicker, which is same as the result above, but increased when the dura is stiffer, which is opposite from the result with spinal cord above. Figure 3-10 (b), (d), (f), and (h) are the spatial vs. temporal results in the SAS along the spine. The wave speed is faster when the dura became thicker and/or stiffer, which can be found from both the pressure vs. time result and spatial vs. temporal result. The fastest wave is always the weakest wave, whose

speed is 25.26 m/s, 25.26 m/2, 48 m/s and 48 m/s for dura thickness and stiffness (2.3 mm, 0.632 MPa), (5.2 mm, 0.632 MPa), (12 mm, 1.99 MPa) and (17.9 mm, 1.99 MPa), respectively. The second fastest wave is always much stronger than the first one, with a speed of 8.73 m/s, 11.43 m/s, 21.82 m/s and 25.26 m/s for the four thickness cases, respectively. More wave oscillation, especially the oscillation of the stronger waves, can be seen in the cordless cases. Wave reflection at the rostral end of the spine can also be seen clearly in these plots.

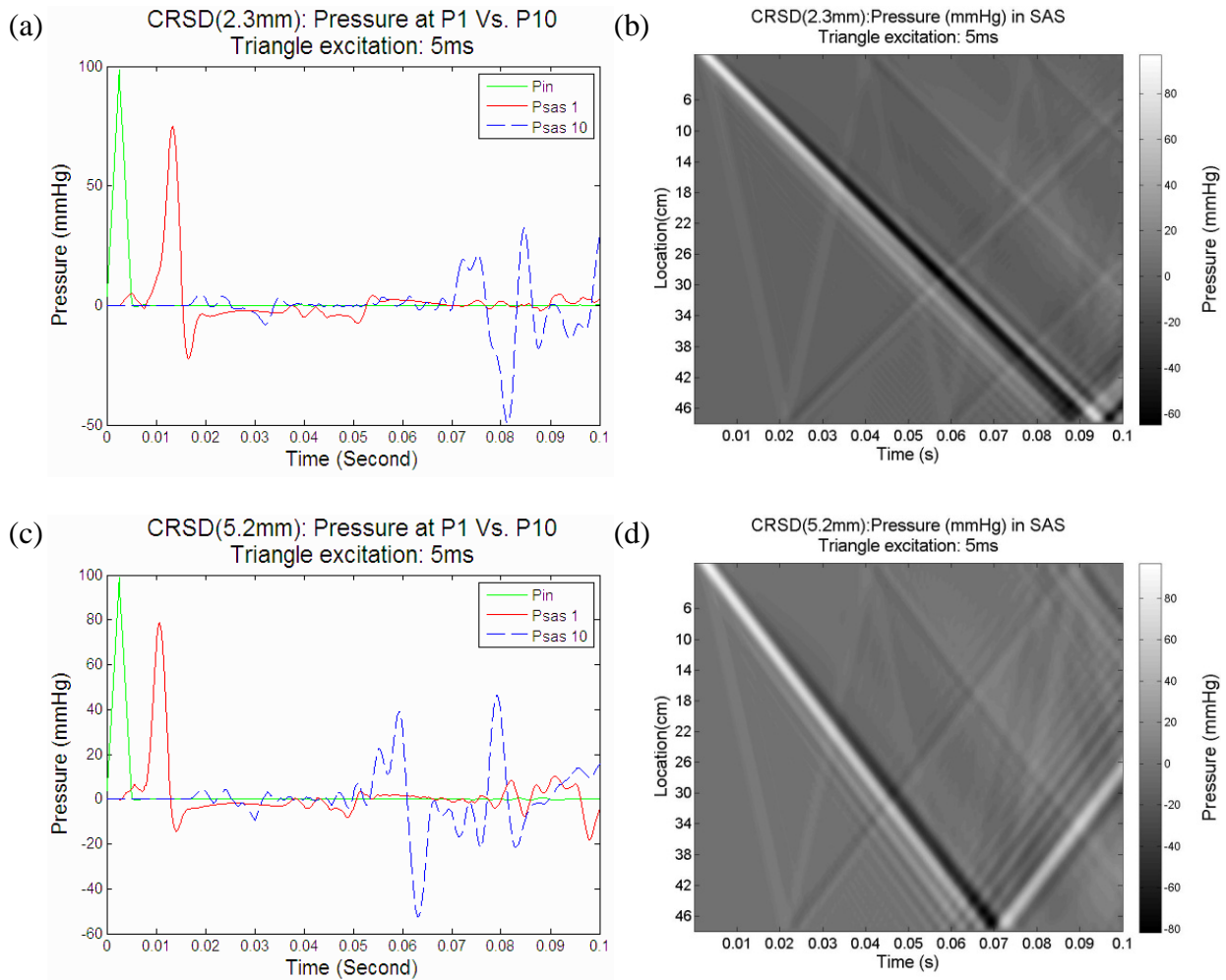




**Figure 3-10: Pressure result for cordless model (CLSD) with different thickness dura in response to a 5 ms triangular impulse during the first 100 ms. (a), (c), (e),(g): Pressure vs. time result at pressure point 1 (solid line) and pressure point 10 (dash line) for dura thickness 2.3 mm, 5.2 mm, 12 mm, and 17.9 mm, respectively. (b), (d), (f), (h): Spatial vs. temporal pressure result in the SAS along the spine for dura thickness 2.3 mm, 5.2 mm, 12 mm, and 17.9 mm, respectively.**

Another extreme assumption is to restore a rigid spinal cord. Hypothetical models CRSD are constructed based on this assumption. Figure 3-11 shows the pressure result for CRSD models in response to a 5 ms duration symmetric triangular impulse at the rostral end of the SAS. This is the same as the CSD and CLSD results; the wave speeds are elevated with the increase of the dura stiffness and thickness. From Figure 3-11, the fastest wave speeds in the four models are

25.26 m/s, 24 m/s 32 m/s, and 32 m/s for dura thickness and stiffness (2.3 mm, 0.632 MPa), (5.2 mm, 0.632 MPa), (12 mm, 1.99 MPa) and (17.9 mm, 1.99 MPa), respectively. And, the second wave speeds in the four models are 6 m/s, 8.14 m/s, 17.78 m/s, and 19.2 m/s for the four cases, respectively. Although similar to CLSD model, the increase of dura thickness and stiffness also elevated the pressure amplitude in the SAS, but the amplitude difference is much smaller than in the CLSD case. Pressure wave oscillation is reduced in CRSD models compare to CLSD models.



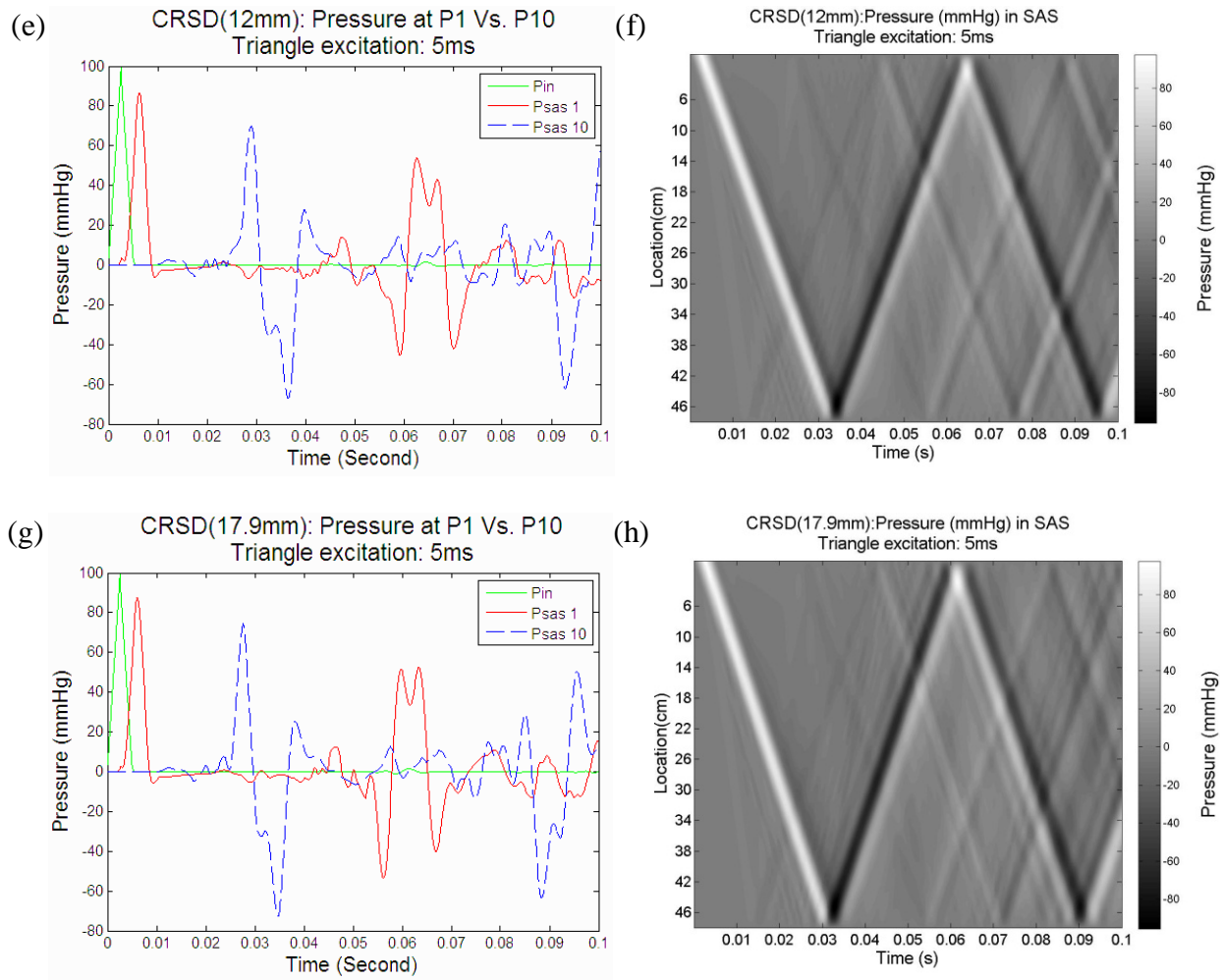


**Figure 3-11: Pressure results for rigid cord model (CRSD) with different thickness dura in response to a 5 ms triangular impulse during the first 100 ms. (a), (c), (e), (g): Pressure vs. time result at pressure point 1 (solid line) and pressure point 10 (dash line) for dura thickness 2.3 mm, 5.2 mm, 12 mm, and 17.9 mm, respectively. (b), (d), (f), (h): Spatial vs. temporal pressure result in SAS along the spine for dura thickness 2.3 mm, 5.2 mm, 12 mm, and 17.9 mm, respectively.**

### 3.4 Theory

The simplest situation examined above is the cord-less model (CLSD), in which the elastic dura enclosed only CSF. For an isotropic cylindrical tube with inner radius of the tube “ $a$ ”, where material with Young’s Modulus “ $E$ ”, density “ $\rho_s$ ”, and a thickness “ $h$ ”, encasing incom-

compressible fluid with density “ $\rho$ ” inside, the wave propagation speed can be calculated by Moens-Korteweg equation:

$$c = \sqrt{\frac{Eh}{2\rho a}}$$

To make the result more accurate, the result can be improved by computing the strain on the midwall of the tube:

$$c = \sqrt{\frac{Eh}{2\rho(a + \frac{h}{2})}}$$

However, the Moens-Korteweg equation cannot solve the cases with the spinal cord (CSD and CRSD models) directly. To calculate the wave speed in such cases, Martin et al. (2009) derived equations with assumptions of an incompressible fluid and thin encasing solid. In their derivation, they considered an isotropic cylindrical tube, having a radius “ $a$ ” (inner radius of the tube), thickness “ $h$ ”, where material with Young’s modulus “ $E$ ”, Poisson’s ratio “ $\nu$ ”, and density “ $\rho_s$ ” encasing fluid with density “ $\rho$ ”. Along the tube central axis is a rod of radius “ $a_c$ ”, representative of an assumed rigid SC. From their derivation making certain assumptions detailed in the reference, the lowest two wave speed can be calculated by[31]:

$$c_1 = \sqrt{\frac{Eh}{2\rho(a + \frac{h}{2})}} \sqrt{1 - \frac{a_c^2}{a^2}}$$

$$c_2 = \sqrt{\frac{E}{\rho_s(1 - \nu)^2}}$$

Here, when the  $a_c$  goes to zero (the cordless cases CLSD),  $c_1$  is consistent with the Moens-Korteweg equation. And,  $c_2$  is the expression for longitudinal (extensional in plane) wave motion in a thin walled shell [31].

At the same time, Cirovic et al. were also working on deriving the equation to calculate the wave speed in a coaxial tube of the cerebrospinal fluid pulse propagation in the spinal column. They derived a characteristic equation to calculate the wave speed transmission in the spinal canal. And, wave equations for three different conditions, elastic dura and spinal cord, rigid dura, and rigid spinal cord, are also derived in the following papers [27-29].

### **3.5 Result and Conclusion**

From analysis in section 3.3.1, a different excitation type and duration do not influence the speed of the wave propagated in SAS.

Complementary to the *in vitro* experiments, the *in silico* analysis presented above provides a more comprehensive understanding of the viscoelastic fluid-filled coaxial system of the spine. Not only the wave speeds can be calculated via the plots above, but how the pressure distributed along the spine and how oscillation and/or reflection happened in the SAS can also be seen from the plot explicitly.

A summary of wave speeds for models CSD, CLSD, and CRSD with different dura thicknesses, measured in the *in silico* and *in vitro* models, and calculated by theory are listed in Table 3-3. What should be noticed is that the wave speeds measured in the *in vitro* results were calculated by dividing the distance between two pressure ports by the time delay of the pressure waves

arrived at the two ports. The delay time was visually estimated from the distance between the feet of the waveforms[5]. Because the fastest waveforms were too weak to be noticed, as shown in figures in section 3.3.1 and 3.3.2, the wave speed calculated in the *in vitro* models are the second waveform, which is also the strongest pressure wave in SAS.

**Table 3-3: Summary of wave speeds for different models measured in the *in silico* and *in vitro* models, and calculated by theory**

Model		Thickness (mm)	Young's Modulus	In silico		In vitro	Martin et al. Theory	
				c <sub>1</sub> (m/s)	c <sub>2</sub> (m/s)	c (m/s)	c <sub>1</sub> (m/s)	c <sub>2</sub> (m/s)
CSD (2 trails for in vitro)	Model 1	17.9	1.99E+06	25.26	40.00	40, 51	25.1	50.1
	Model 2	12		22.86	40.00	28, 30	22.6	50.1
	Model 3	5.2	6.32E+05	8.00	28.24	24, 24	9.7	28.2
	Model 4	2.3		5.65	24.00	14, 16	6.9	28.2
CLSD	Model 1	17.9	1.99E+06	25.26	48.00	36	32.7	50.1
	Model 2	12		21.82	48.00	45	29.5	50.1
	Model 3	5.2	6.32E+05	11.43	25.26	26	12.6	28.2
	Model 4	2.3		8.73	25.26	18	9	28.2
CRSD	Model 1	17.9	1.99E+06	19.20	32.00	/	25.1	50.1
	Model 2	12		17.78	32.00		22.6	50.1
	Model 3	5.2	6.32E+05	8.14	24.00		9.7	28.2
	Model 4	2.3		6.00	25.26		6.9	28.2

The results indicate that the wave speed measured in the *in silico* models consist with both the *in vitro* result and the predicted wave speed for all the systems. From the result, it can be concluded that although the elastic properties of the spinal cord do related to the waves propagation speed, it is the properties of the spinal aqueduct's outer wall that influence the wave speed the most. On the other hand, the thickness of the outer wall also has influence on the wave speed. These consist with the *in vitro* conclusion.

## CHAPTER 4

### INFLUENCE OF STENOSIS AND/OR SYRINX

#### 4.1 Introduction

Blockage, or obstruction, in a biological system conveying fluid might cause various diseases. A common occurrence is blockage in a blood vessel system (thrombus or blood clot). When a thrombus occupies a relatively large percentage of cross sectional area of the lumen of the vessel, blood flow to the tissue supplied will be reduced and thus various symptoms will appear. There have been numerous studies on issues related to thrombus.

However, blockage can also happen to the spinal CSF flow system, which will be called a stenosis in this thesis. CSF flow obstruction can result in elevated intracranial pressure, which was proposed by many neurosurgeons to be a hydrodynamic mechanism for syrinx formation [5, 13]. Congenital syringomyelia, such as Arnold-Chiari malformation introduced in chapter 1.5, correlates with blockage caused by protrusion or enlargement of the cerebellar tonsils into the suboccipital region of the spinal subarachnoid space see Figure 1-7.

Intraspinal inflammations such as arachnoiditis or meningitis, a tumor, or a tether of spinal cord, which usually involved spinal cord scarring, can also cause blockage in the spinal canal. Post-traumatic syringomyelia was first described by Bastian in 1867 and by Strümpell in 1880. And, during World War I the experience of gunshot wounds to the spinal cord received a more extensive report in 1915 by Holmes. The development of syringes as a delayed complication of

traumatic spinal cord injuries was being noted with increasing frequency. In a study by Schurch et al. in 1996, a group of 449 patients were followed prospectively with yearly MRIs; 20 (4.4%) developed symptoms of post-traumatic syringomyelia, occurring as early as two months and as late as 30 years after injury [19, 42].

As introduced in Section 1.5.2, in case of ACMI syringomyelia, a decompression surgery that is also called suboccipital craniectomy will typically be performed. The main goal of surgery is to remove the flow blockage in the hindbrain of the patient to provide more space for the cerebellum without entering the brain or spinal cord. In order to understand how the blockage in the spinal canal impacts the pressure environment in the spinal subarachnoid space, how the syrinx can be caused by blockage in CSF flow, and how the pressure can be relieved after the decompression surgery, six *in silico* models representative of various spinal canal conditions were constructed and are discussed in this section. Four of the models are constructed almost identical to the *in vitro* models built by Martin et al. in 2005. Two additional hypothetical *in silico* models are defined to represent more conditions for comparison.

## **4.2 Methodology**

Martin et al. had constructed several models in simulating four different spinal canal conditions (SAE, SRE, SSE, and SSED). Three of these models have a “rigid” dura constructed with glass. The other model had a much thicker but distensible dura. In this thesis, two additional *in silico* models (CSRD and SRED) are constructed for comprehensive comparison. The abbreviation and definition of the six *in silico* models are given as follows:

- ***CSRD (Spinal cord, SAS and Rigid Dura model):***

hypothetical model, similar to model CSD, but with rigid dura.

- ***SAE (Stenosis Alone Experiment model):***

representative of patient with a spinal stenosis formed in the spinal canal, and with a nearly rigid dura.

- ***SSE (Stenosis and Syrinx Experiment model):***

representative of a syringomyelia patient with a moderate sized syrinx formed after a spinal stenosis appeared in the spinal canal, and with a nearly rigid dura.

- ***SSED (Stenosis and Syrinx Experiment model with distensible spinal column):***

similar to SSE but the dura was replaced with a flexible and thicker material.

- ***SRE (Stenosis Removed Experiment model):***

similar to SSE, but with the stenosis removed leaving the syrinx alone in the spinal cord.

- ***SRED (Stenosis Removed Experiment with Distensible spinal column):***

similar to SRE but the dura replaced with a flexible and thicker material.

Detailed structure and dimensions of the glass encasing tube of the *in vitro* models are given in Figure 4-1 [5]. Ten pressure ports are set up along the tube at intervals of 4 cm, and the end two ports are the input port and out flow port. The two ends of the SAS would be blocked after the spinal cord and syrinx were positioned in place.

The geometry and dimensions of the *in silico* models are defined based on the *in vitro* models, shown in Figure 4-2. Detailed dimensions are listed in Table 4-1.

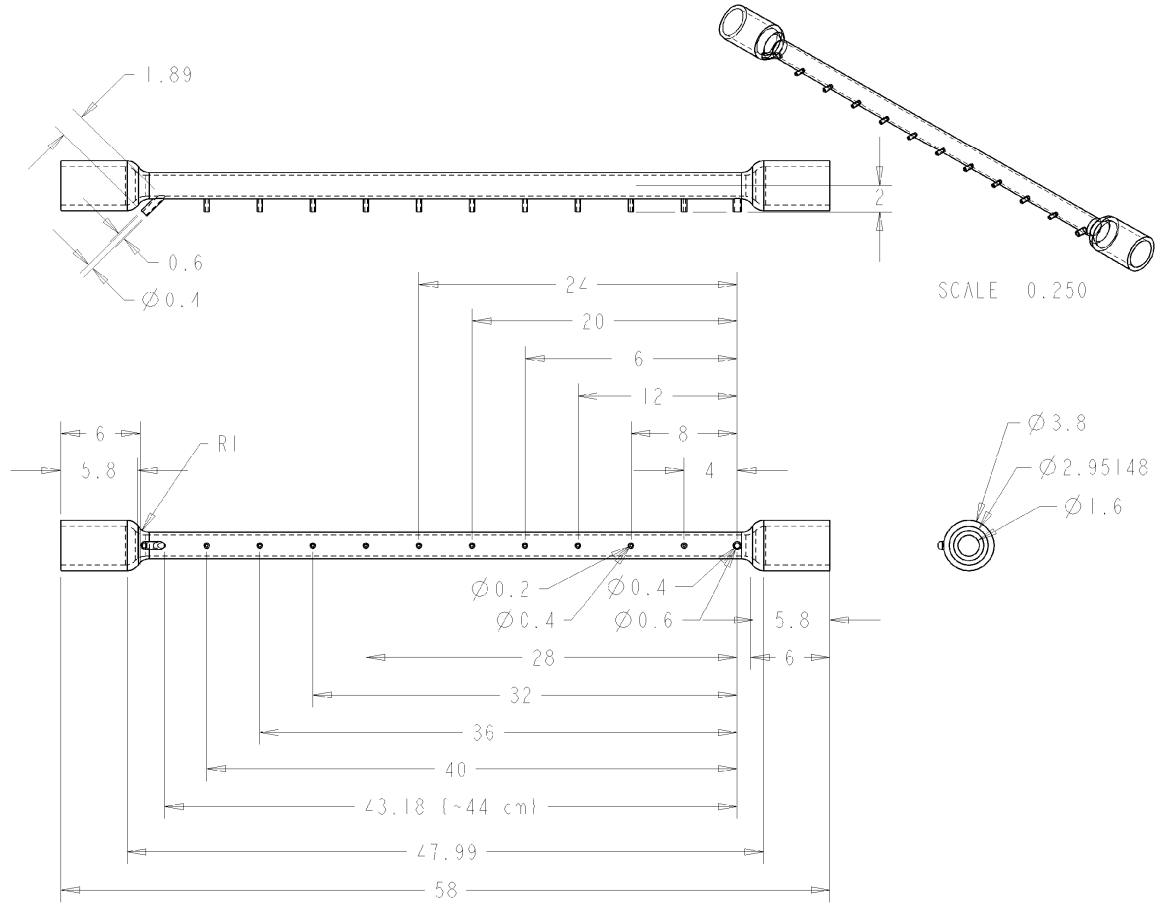


**Figure 4-1: Detailed structure and dimensions of the glass encasing tube for the *in vitro* models.[5]**

**Table 4-1: Dimensions of the Six Models Examining Influence of Blockage in CSF Flow and/or Syrxin in Spinal Cord on the Spinal system**

Model Types	Dimensions (mm)							
	Length	Dura Thickness	SAS Diameter	SC Diameter	Syrinx		Stenosis	
					Length	Diameter	Length	Diameter
CSRD	480	1.2	15.6	10	/	/	/	/
SAE					/	/	20	10.6
CSE					132	7 → 3.2	/	/
SRE					(103 straight part + 29 tapered part)		20	10.6
SSE							/	/
SSED							/	/
SRED		12						

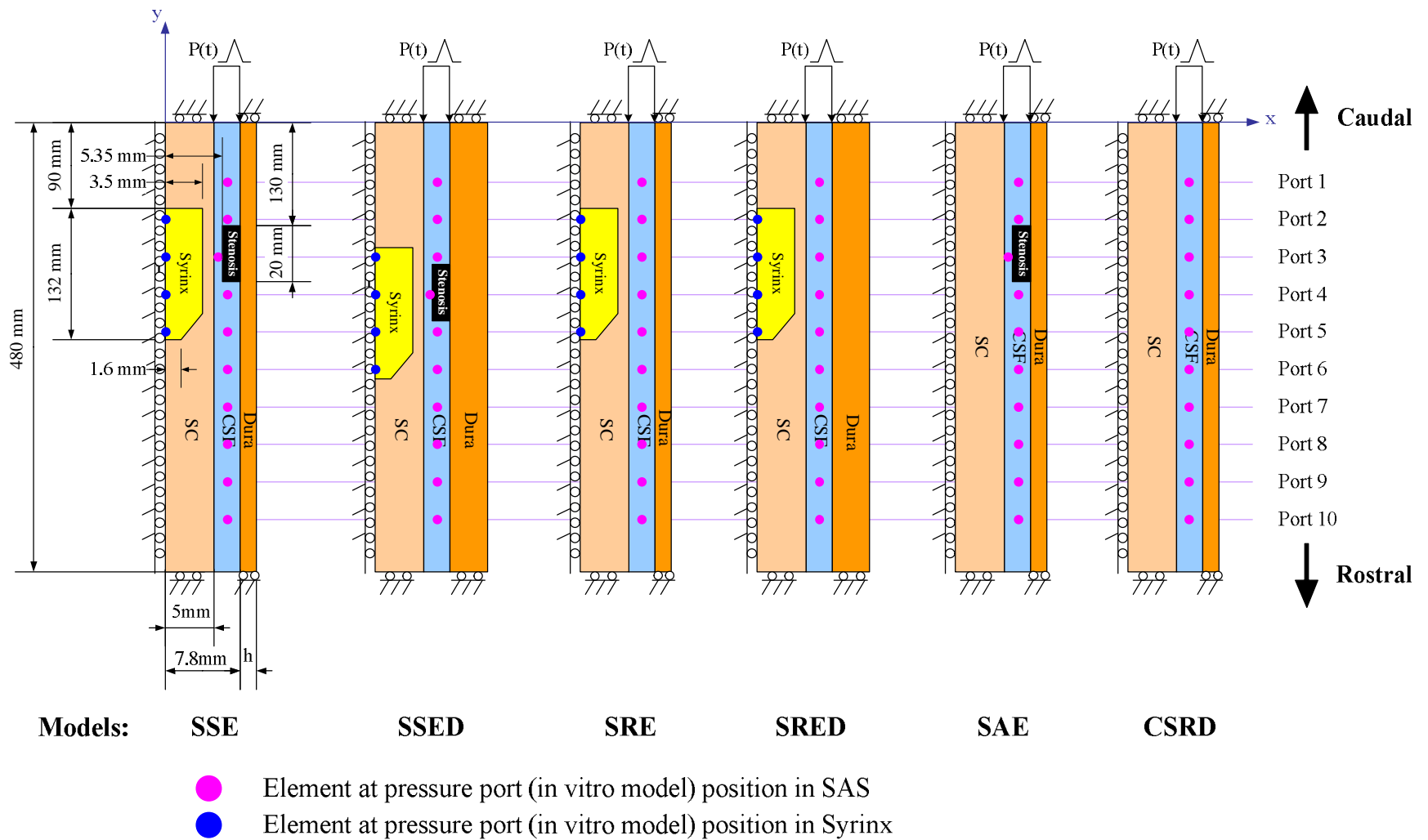


**Figure 4-2: Geometries of the seven 2-D axisymmetric models set up in ANSYS. The horizontal to vertical scale is exaggerated. The dimensions and boundary conditions are defined based on the *in vitro* models. Position of pressure sampled element in SAS and Syrinx can be found in the figure**

The models are built in quadrant (+X,-Y), and axisymmetric about the Y axis. Major dimensions and boundary conditions are given in Figure 4-2. Similar to the elastic properties group models, normal displacement on the symmetric axis (Y axis) is forbidden, and both ends of the solid components (dura and spinal cord) are fixed axially. The movements of the fluid ends are set to be free.

Four models -- CSRD , SAE, SSE, and SRE – have a rigid encasing dura, which was made of glass with a thickness of 1.2 mm. SSE and SRE models have distensible dura, which was thicker (12 mm) than the other five models. The material for the dura in SSE and SRE is the same material as for the spinal cord (Sylgard) but with different mix ratio, and thus has slightly different mechanical properties. Positions of the stenosis and syring in each model are also indicated in the figure. The syring is a tapered structure, whose diameter ranges from 7 mm to 3.2 mm with a total length of 132 mm. According to Martin et al., the dimensions of the syring are defined based on MRI of a patient. The stenosis in the *in vitro* models was created by a tough rubber material which blocked more than 90% of CSF flow in the SAS area [5]. Ten elements in the SAS and four elements in the syring are selected at the same location of the pressure ports in the *in vitro* models. To simplify the *in silico* analysis, the input and out flow ports are set to be the two ends of SAS at  $y = 0$ , and  $y = -480$  mm parallel to the symmetric axis, which is different from the *in vitro* models.

Major material properties are defined based on the *in vitro* definition [5], and the ones that were not given in the *in vitro* data are estimated according to general properties of the material

from some references (see section 2.3). Material properties for the two additional models CSRD and SRED are defined based on the most similar models. Detailed material properties of the components in each model are given in Table 4-2.

**Table 4-2: Material properties of the six Post-Traumatic group models.**

Materials		Models					
		CSRD	SRE	SAE	SSE	SRED	SSED
Dura	Material	Glass			Sylgard		
	Young's Modulus (Pascal)	8.00E+10			2.00E+06		
	Poisson Ratio	0.25			0.495		
	Density (kg/m <sup>3</sup> )	2600			1060		
	Damping Value	0.001			0.002		
CSF	Material	Water					
	Bulk Modulus (Pascal)	2.20E+09					
	Viscosity (Pa·s)	6.90E-04					
	Density (kg/m <sup>3</sup> )	996					
SC	Material	Sylgard					
	Young's Modulus (Pascal)	8.30E+05	5.20E+05	3.20E+05	5.20E+05		
	Poisson Ratio	0.495					
	Density (kg/m <sup>3</sup> )	1060					
	Damping Value	0.002					
Syrinx	Material	/	Water	/			
	Bulk Modulus (Pascal)		2.20E+09				
	Viscosity (Pa·s)		6.90E-04				
	Density (kg/m <sup>3</sup> )		996				
Stenosis	Material	/			Rubber		
	Young's Modulus (Pascal)				5.00E+07		
	Poisson Ratio				0.45		
	Density (kg/m <sup>3</sup> )				1200		
	Damping Value				0.01		

### 4.3 Results

There are two sources of pulsation in CSF pathways: arterial pulse wave and the venous changes consequent upon change of posture, respiration, coughing, muscular exertion and so on

[21]. Both of these two pulsations will be conducted on the models separately to examine the influence of stenosis and /or syrinx under different pulsation types. A continuous, periodic waveform will be applied to the models in simulating the arterial pulse wave, and a short triangular symmetric impulse will be input to the model in mimicking the venous changes caused by coughing etc. Because the CSF and venous blood are in a state of balance across venous membranes, the venous pressure is transmitted to the CSF pathways easier than through the arterial system [21]. Thus, more discussion will be conducted in the coughing effect analysis.

#### **4.3.1 Normal CSF Flow Waveform Input Result**

In order to examine the influence of arterial pulse wave on the CSF pressure, a continuous, sinusoidal-like waveform in mimicking a normal CSF flow was input to the models. The waveform of the CSF flow was plotted based on the CSF flow waveform with period of 0.87 second from Martin et al.'s *in vitro* experiments in Figure 4-3, which was obtained from an actual CSF flow waveform measured at C2 level [5].

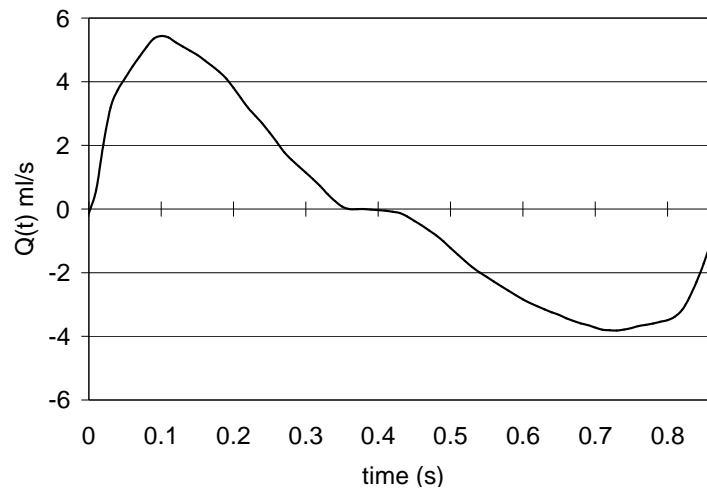


**Figure 4-3: CSF flow waveform in the *in vitro* models which was obtained based on *in vivo* measurement at C2 level [5].**

The input flow can be converted to a valid pressure input in the *in silico* analysis by:

$$\text{Pressure (Pascal)} = \frac{F \text{ (N)}}{A \text{ (m}^2\text{)}} = \frac{M(\text{kg}) * a \left(\frac{\text{m}}{\text{s}^2}\right)}{A \text{ (m}^2\text{)}} = \frac{Q \left(\frac{\text{m}^3}{\text{s}}\right) * 1 \text{ (s)} * \rho \left(\frac{\text{kg}}{\text{m}^3}\right) * a \left(\frac{\text{m}}{\text{s}^2}\right)}{A \text{ (m}^2\text{)}}$$

In realistic cases, the spine is vertical most of the time, and in Martin et al.’s *in vitro* models, the flow was input via a vertical tube, so the acceleration “a” can be replaced by the acceleration of gravity “g: here, which is 9.8 m/s<sup>2</sup>. To mimic a continuous CSF pulsation, the waveform was replicated and expanded to fill through the whole sampling time (5 seconds), shown as Figure 4-4. To simplify the analysis, the time-step was set to be 10 ms, thus 500 steps will be calculated in these cases. Pressure distribution and the displacement along the spine will be examined in this section.

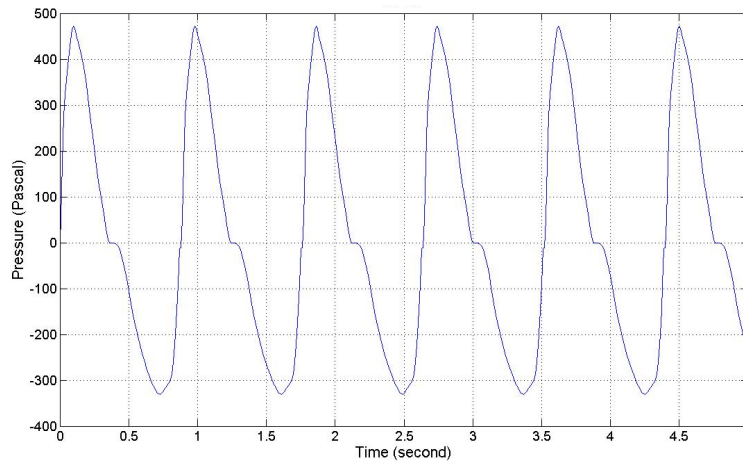


**Figure 4-4: CSF flow waveform applied at the *in silico* models, which is a replication of the *in vitro* input.**

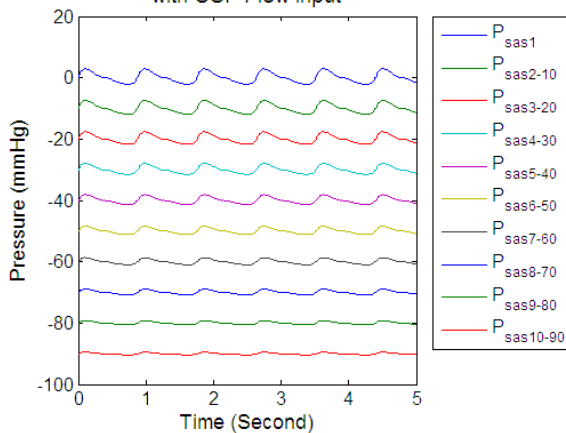
#### 4.3.1.1 Pressure changes over time

Figure 4-5 gives the pressure results within the first 5 seconds at the ten elements that have the same coordinates as the pressure ports in the *in vitro* models. The pressure value at each port has 10 mmHg deductions from the anterior one to distinguish them from each other. Stenosis and

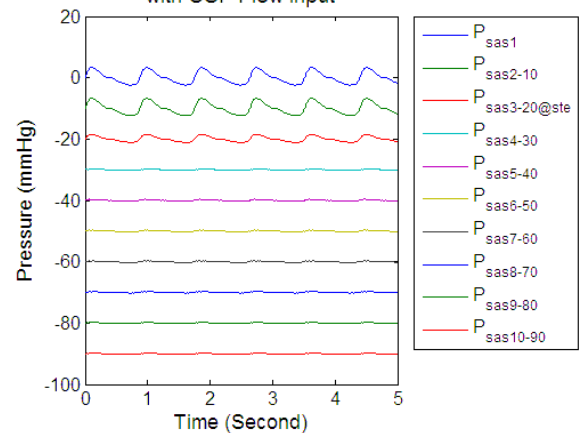
syrix are moved 4 cm rostral together in SSED as compared to the other models. The relative location of the syrix and stenosis for each model are also denoted in the legend of the plots.

In order to understand the influence of the syrix and/ or stenosis, it's better to first compare the four rigid dura models (CSRD, SAE, SRE and SSE) which simulate different pathologies with/without syrix and/or stenosis. The CSRD model can be regarded as a criterion representing a healthy spinal system with neither syrix nor stenosis, while SSE is the final pathology with both syrix and stenosis present. SAE and SRE are models with stenosis or syrix alone in the spinal system representing the case before the formation of the syrix and the case after surgery.

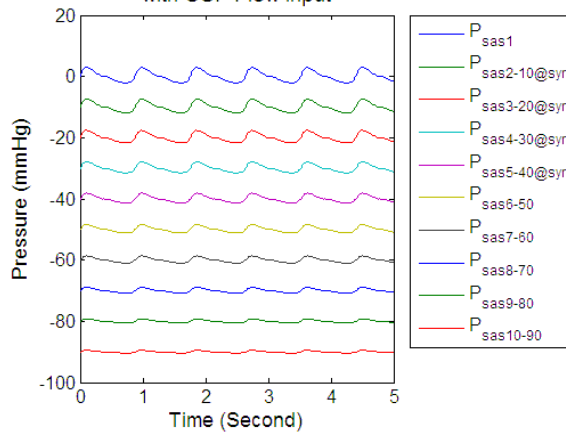
(a) CSRD(1.2mm):Pressure at SAS Pressure Ports with CSF Flow input



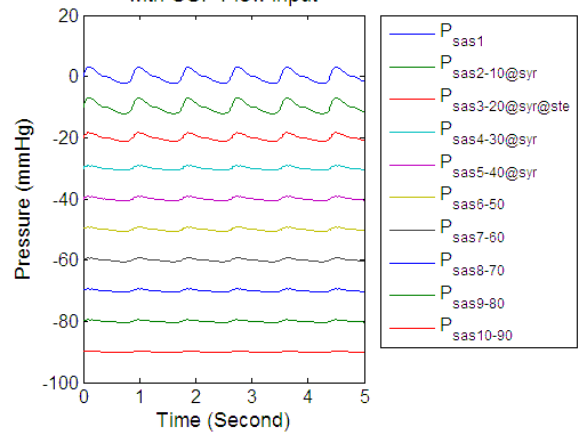
(b) SAE(1.2mm):Pressure at SAS Pressure Ports with CSF Flow input



(c) SRE(1.2mm):Pressure at SAS Pressure Ports with CSF Flow input



(d) SSE(1.2mm):Pressure at SAS Pressure Ports with CSF Flow input



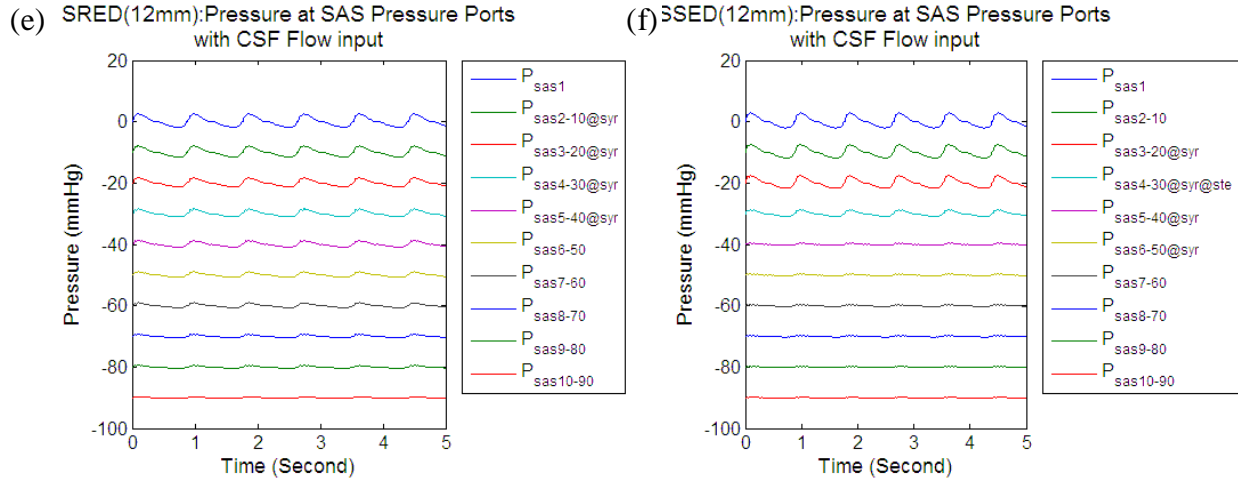


**Figure 4-5: Pressure in SAS at the ten pressure port positions in the first 5 seconds in response to excitation of continuous normal CSF pulsation for the six models. Pressure at each port has 10 mm Hg deductions from the anterior port.**

From Figure 4-5 (a) to (d), it can be found that for a healthy spinal system in CSRD, the pressure amplitude attenuated smoothly along the spine. However, when a stenosis appeared in the CSF pathway in SAE, pressure appeared to be higher ahead of the stenosis (port 1 and 2) and then decreased at the stenosis position (port 3) as compared to CSRD. Little pressure wave passed the stenosis so that pressures were around zero at ports behind the stenosis. After the syrinx formed in the spinal cord in SSE model, same as that in SAE, pressure ahead of the stenosis was still high, and a pressure decrease can also be found at the stenosis, but pressure amplitude at port 4 to 6 behind stenosis was higher as compared to SAE. After the stenosis was removed (SRE model), pressure attenuated along the spine similar to that in CSRD model with no sudden change, and the amplitude is higher than that in SSE model.

Influence of dura material property changes has been discussed in CHAPTER 3; a question is how will the dura material properties influence the system when a syrinx is present alone or

present with a stenosis? Figure 4-5 (e) and (f) give the pressure in the SAS for SRED and SSED models. Compared to the rigid dura model, pressure amplitude in SRED and SSED were smaller, and more oscillation appeared in the SSED model.

To further examine the impact of a stenosis and/ or syrinx, pressure in the syrinx for models SRE, SRED, SSE and SSED are given in Figure 4-6. The stenosis location is also denoted in the plots.

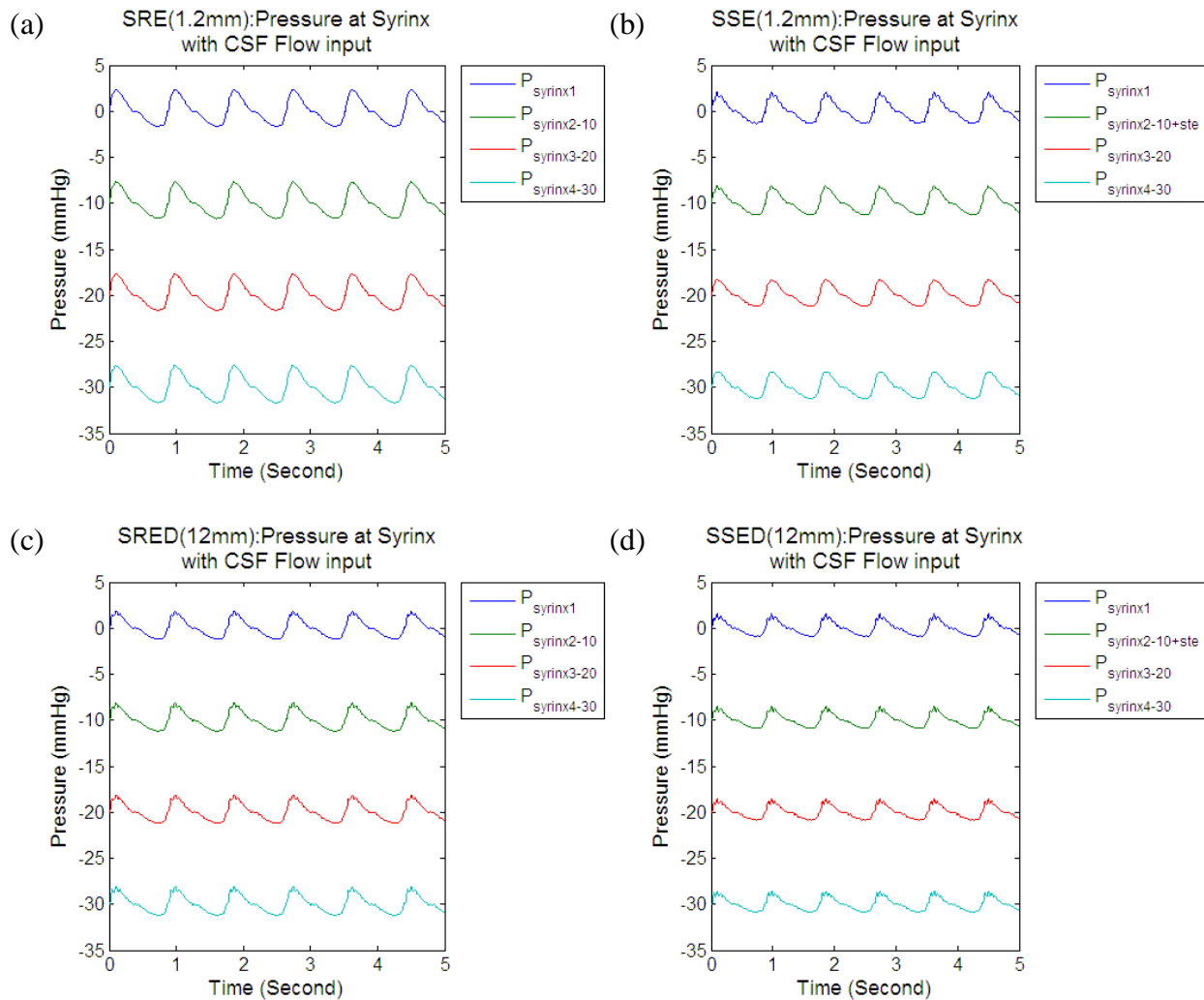


**Figure 4-6: Pressure in syrinx at pressure port positions in the first 5 seconds in response to excitation of continuous normal CSF pulsation for the six models. Pressure at each port has 10 mm Hg deductions from the anterior port.**

With a stenosis present in the SSE model, minor oscillation can be observed at syrxinx port 1, which is ahead of the stenosis. Pressure everywhere in the syrxinx was lower than that in the SRE model. And, a minor attenuation can also be found along the spine. After the removal of stenosis in the SRE, the waveform was smooth and rare attenuation can be observed at the pressure ports.

When we replace the rigid dura with a distensible and thicker material in SRED and SSED models, oscillation can be observed in both models, but more severe in SSED. Pressure amplitudes were lower in both distensible dura models (SRED and SSED) than those in models with a rigid dura (SRE and SSE).

#### 4.3.1.2 Pressure distribution and wave propagation speed

Same as what has been done for elastic group models, spatial vs. temporal result will be meshed in the following. The input CSF flow was a continuous periodic waveform; thus, the spatial vs. temporal result in the first 5 seconds kept in the periodic characteristic with a same period (see Figure 4-7).

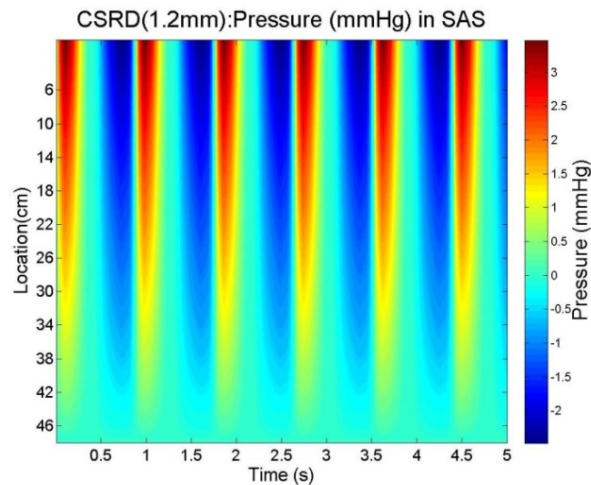


**Figure 4-7: Spatial vs. temporal pressure result of CSR in the first 5 seconds in response to periodic excitation of CSF flow.**

Thus, in order to distinguish the contour shade easier, the spatial vs. temporal results in the first 1 second for each model were plotted in Figure 4-8. Due to the free output of CSF flow and nonzero damping values for materials in this analysis, no reflection can be observed in either model because the pressure wave was attenuated completely before it reached the rostral end of the spine, and dissipation and oscillation was so severe that the shape of the contoured shade cannot be determined exactly. On the other hand, wave speeds in these models are too fast to be measured here. But from these plots, the influence of stenosis, syrinx, and dura properties on the pressure wave propagation can be observed clearly in a perspective other than the analysis in section 4.3.1.1.

Same as conclusion in above section, for a healthy spinal system CSRD, pressure attenuated smoothly along the spine. When a stenosis appeared in the spinal canal in SAE model, the majority of pressure was reflected by the stenosis, so that the magnitude of pressure ahead of the stenosis was stronger than that in the CSRD. Little pressure wave passed through the stenosis and wave speed in the stenosis region (13 to 15 cm) was decreased significantly. After a syrinx formed in the spinal cord in the SSE model, less pressure wave was reflected and more passed through the narrowed region; thus, pressure intensity appeared to be weaker ahead of the stenosis, while more pressure could be observed behind the stenosis. And the wave propagation was slowed down at the stenosis region from 13 cm to 15 cm, which is same as the SAE model. After stenosis removal in the SRE model, pressure distribution along the spine over time returned to be similar as that in CSRD. With a distensible dura in SRED and SSED, obviously dissipation and

oscillation of pressure could be found in both models. And though it was difficult to calculate the exact value, wave speed appears slower than that in rigid dura models.

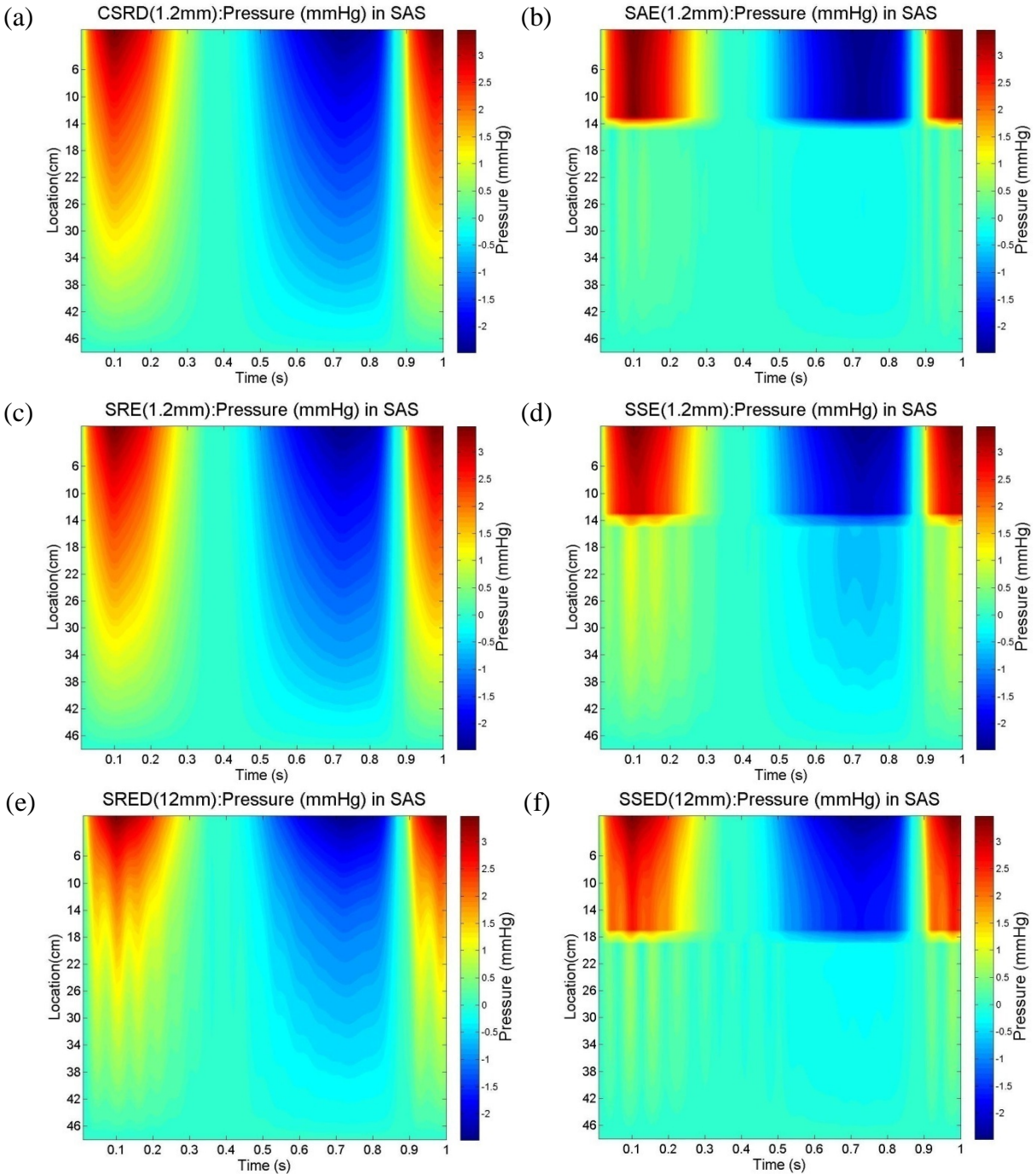


**Figure 4-8: Spatial vs. temporal pressure in SAS result of for the six models in the first 1 second in response to periodic excitation of CSF flow.**

Figure 4-9 shows the spatial vs. temporal pressure result in the syringe for model SRE, SSE, SRED, and SSED. The pressure in the syringe was almost constant at the same time along the syringe in SRE and SRED model. But with the presence of stenosis in SSE and SSED model, attenuation could be found near the stenosis at 13 cm, and the wave speed were slower than SRE and SRED. And, with a distensible dura in SRED and SSED, severe dissipation and oscillation can be observed in both models, and wave speeds were slower than that in the rigid dura models.

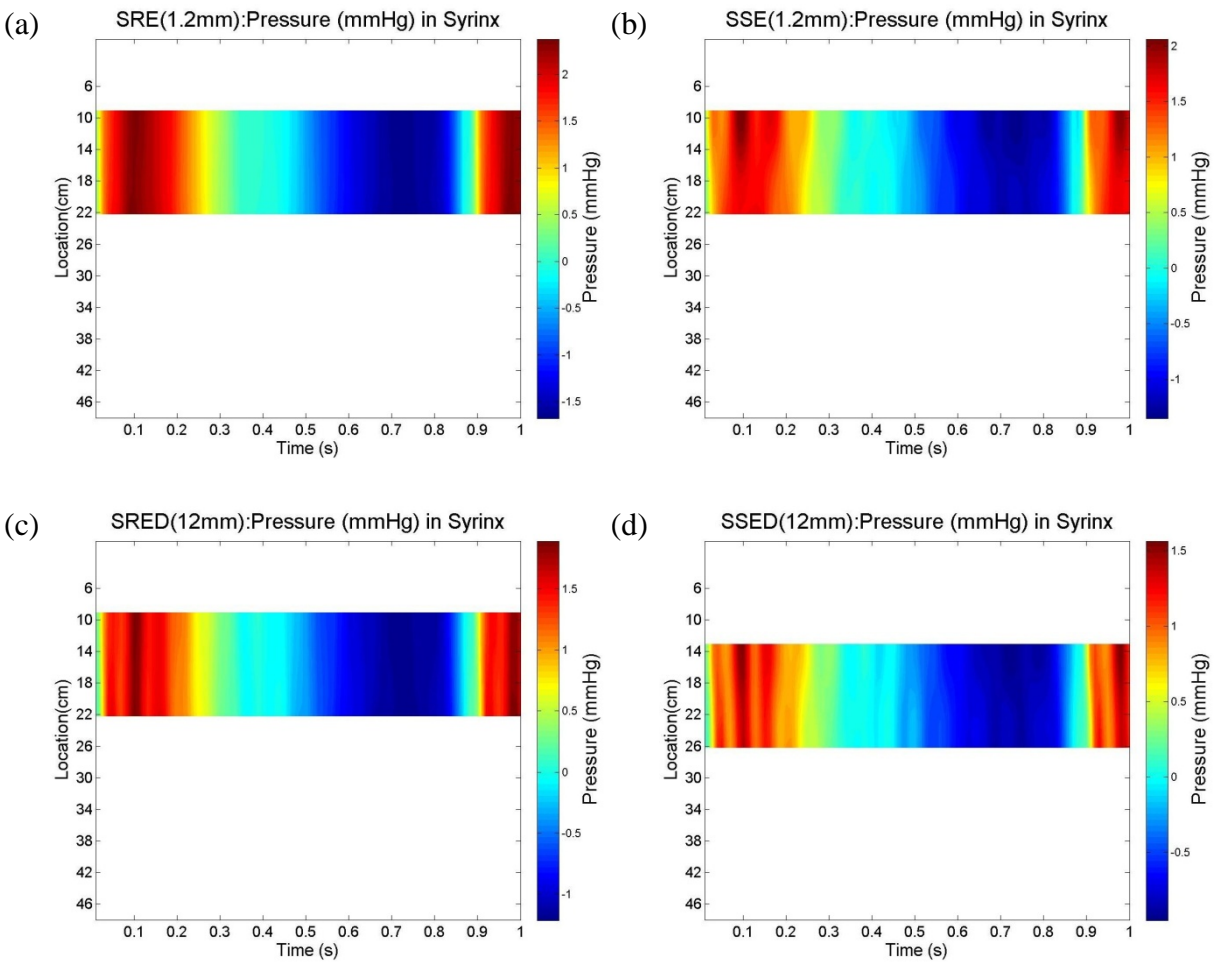


**Figure 4-9: Spatial vs. temporal pressure in syringe result of for the six models in the first 1 second in response to periodic excitation of CSF flow.**

### 4.3.1.3 Pressure and displacement at different times

The influence of stenosis on the pressure environment in the SAS and syrinx has been introduced in the above sections. Other than continuing to focus the attention on the pressure environment of the spinal system, displacements of the spinal cord and syrinx at different times, combined with the pressure at the same time, will be examined in this section. As discussed in the last section, because the input CSF flow is a periodic input with a period of 0.87 seconds, the pressure in the SAS and syrinx is also a periodic wave. So, pressure and displacement in the first 1 second with a 100 ms interval will be examined here. Figure 4-10 to Figure 4-15 give pressure in the SAS (and syrinx) along the spine, and displacement of the spinal cord (and syrinx) for the six models at 100 ms, 200 ms, ..., 1second. Regions of syrinx and stenosis are denoted as different gray areas. The influence of stenosis and syrinx on the pressure in SAS is much more obvious, and same conclusion can be made as in the above Sections 4.3.1.1 and 4.3.1.2.

For a healthy spinal cord in the CSRD model in Figure 4-10, pressure attenuated smoothly to zero along the spine due to the free end of CSF flow. The radial displacement in the CSRD model traveled along the spine with a very long wavelength so that the radial displacement along the spine looks linear. Meanwhile, the spinal cord also moved axially in the direction of the distended spinal cord.

With a stenosis presents in the SAE model in Figure 4-11, pressure was reflected majorly by the blockage and decreased remarkably at the stenosis site, with only a little pressure wave passing the stenosis. The radial displacement of the spinal cord was split into two opposite phases by

the stenosis. Within the first 400 ms, the spinal cord shrank ahead of the stenosis and distended behind the stenosis. Then, from the 500 ms, the spinal cord distended ahead of the stenosis and shrank behind it. The same is observed for the CSRD model simulation; the spinal cord moved axially to the direction of the distended spinal cord at the same time. This situation repeated at around 900 ms, which is after the first period of the input pulsation.

After a syrinx formed in the SSE model in Figure 4-12, pressure in the SAS reflected at the stenosis, but with a larger pressure wave passing it. The decrease of pressure amplitude at the stenosis was reduced significantly compared to that in SAE model. Pressure in the syrinx has a smaller amplitude than that in the SAS, and was changed at the stenosis site, increased or decreased. The radial displacement of the spinal cord in the SSE model became more complicated. Although like in the SAE model, the radial displacement of the spinal cord was split into two opposite phases by the stenosis, deformation at the syrinx region was boosted because of the synchronous deformation of the syrinx, which is also given in Figure 4-12. On the other hand, the transmural pressure is positive at the distended area, and negative at the compressed region. And still, both the spinal cord and the syrinx moved axially to the direction of the distended part at the same time.

Due to the increasing spinal cord cross-sectional area caused by the tapered end of the syrinx from 20.3 to 22.2 cm, radial displacement of both the spinal cord and syrinx in this region has a significant decrease in this area, while the axial displacement does not have a substantial change.

After the stenosis was removed in the SRE model in Figure 4-13, the solo existence of the syrinx does not appear to have a noticeable influence on the pressure, neither in the SAS nor in the syrinx. The radial displacement of the spinal cord was similar to that in the CSRD model, but with a boost in the syrinx region due to the synchronous deformation of the syrinx. The transmural pressure along the syrinx changed consists with the change of the radial displacement. And like in the SSE model, the tapered end of the syrinx relieved the radial deformation of the spinal cord and syrinx, and both the spinal cord and the syrinx moved axially to the direction of the distended part.

With a distensible dura in the SRED model in Figure 4-14 and the SSED models in Figure 4-15, both the pressure and displacement were similar to that in the SRE and SSE models, but with a faster pressure attenuation ahead of the syrinx. The radial deformation in the SRED model was bigger than in the SRE model due to the distensible dura, especially in the non-syrinx region. And, the radial deformation in the SSED model was smaller than in the SSE model because of the 4 cm rostral moved syrinx and stenosis.

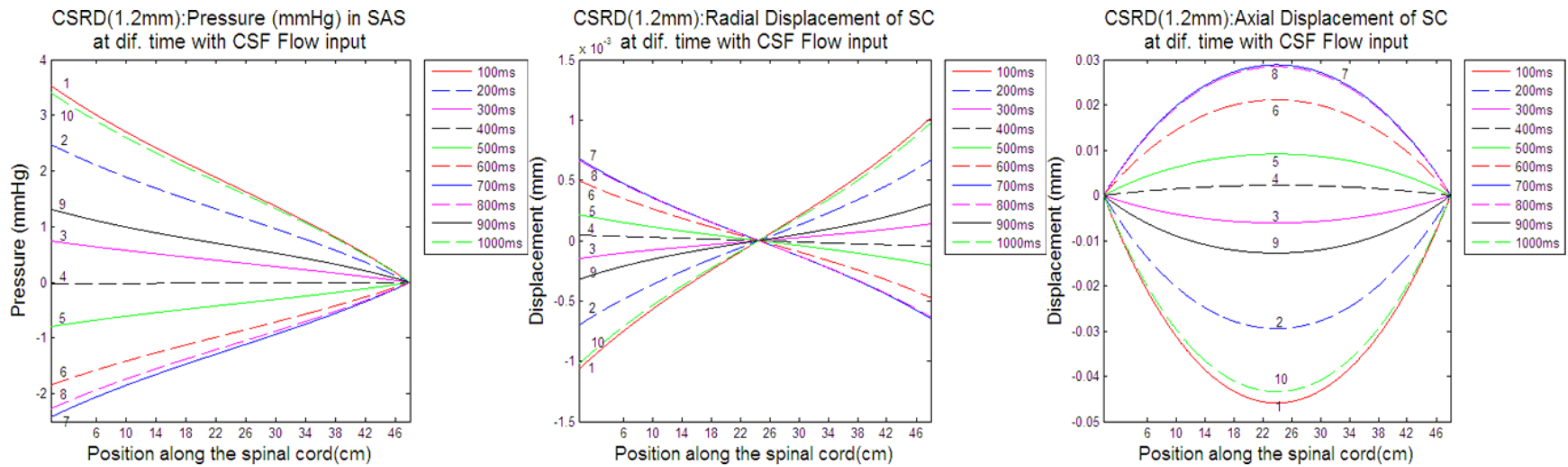


**Figure 4-10: Pressure in SAS along the spine and displacement of spinal cord in response to excitation of continuous normal CSF pulsation for CSR models at  $t = 0.1, 0.2, \dots, 1$  second, identified as curves 1, 2, ..., 10.**

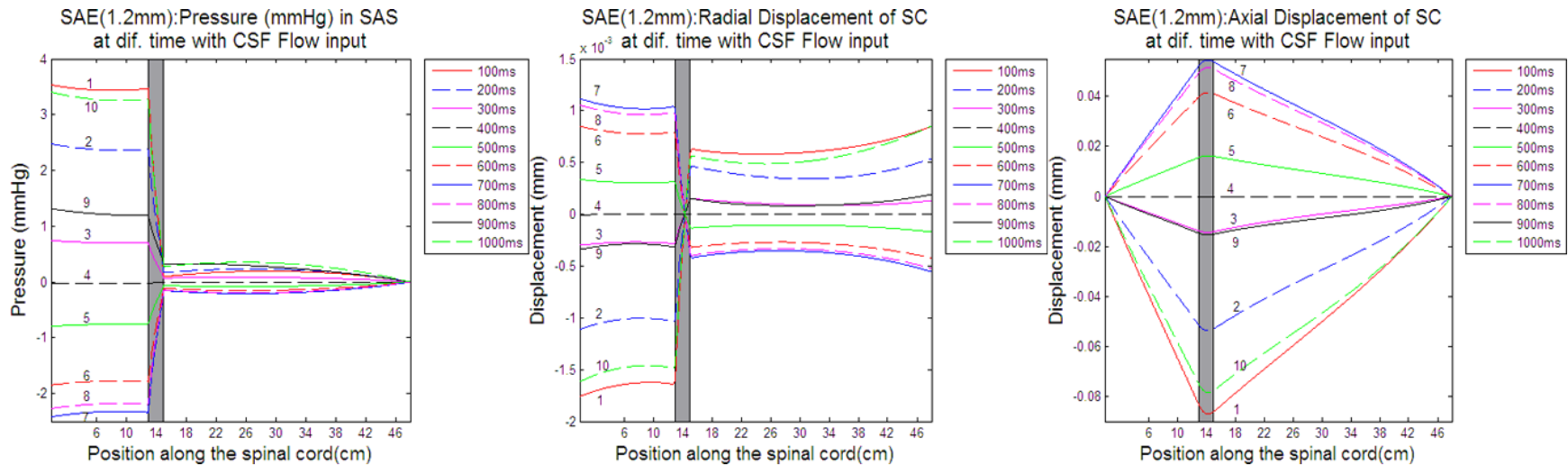


**Figure 4-11: Pressure in SAS along the spine and displacement of spinal cord in response to excitation of continuous normal CSF pulsation for SAE models at  $t = 0.1, 0.2, \dots, 1$  second, identified as curves 1, 2, ..., 10.**

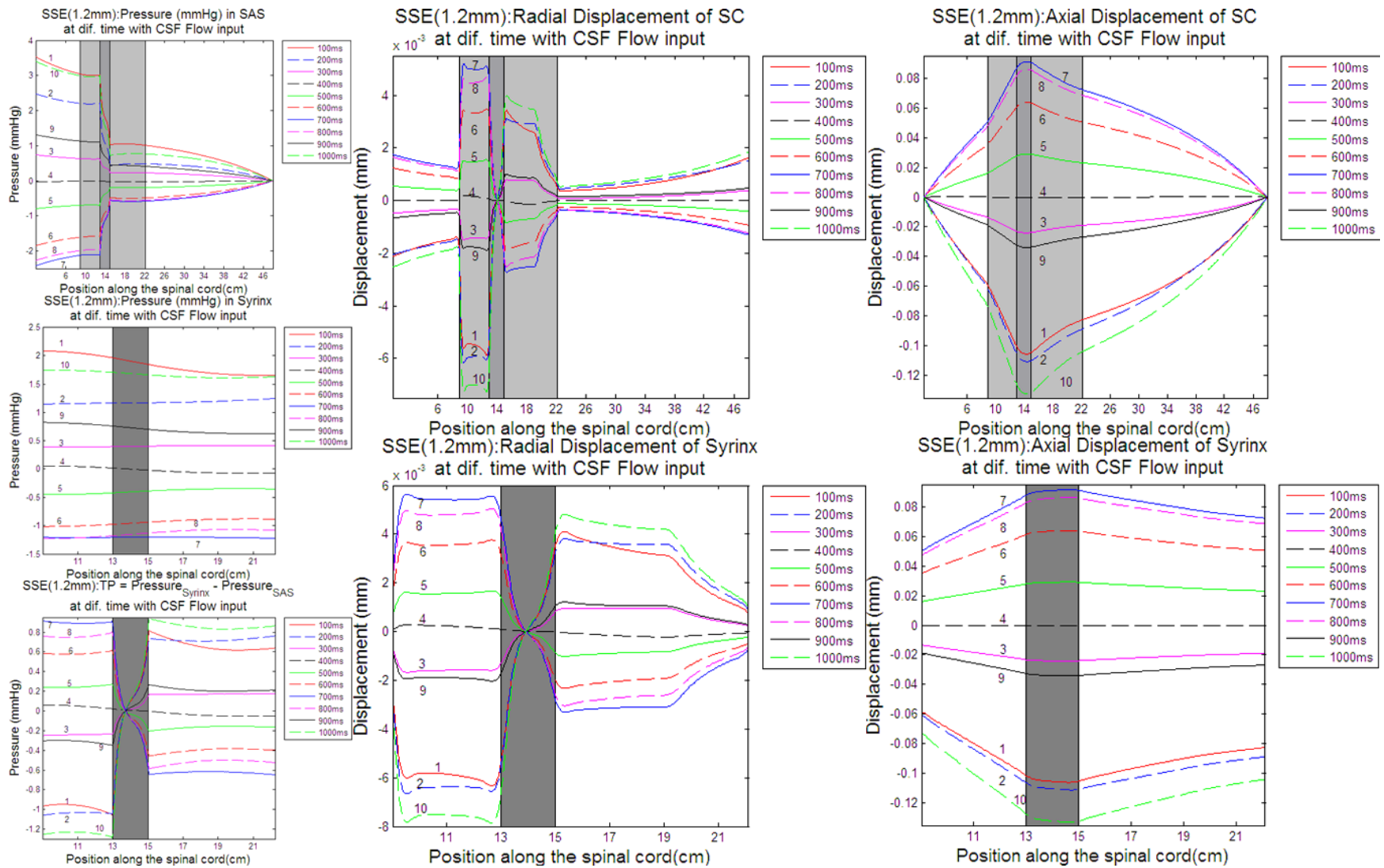


**Figure 4-12: Pressure in SAS and syringe along the spine, transmural pressure in the system and displacement of spinal cord and syringe in response to excitation of continuous normal CSF pulsation for SSE model at  $t = 0.1, 0.2, \dots, 1$  second, identified as curves 1, 2, ..., 10. Syringe and stenosis are denoted in different gray area.**

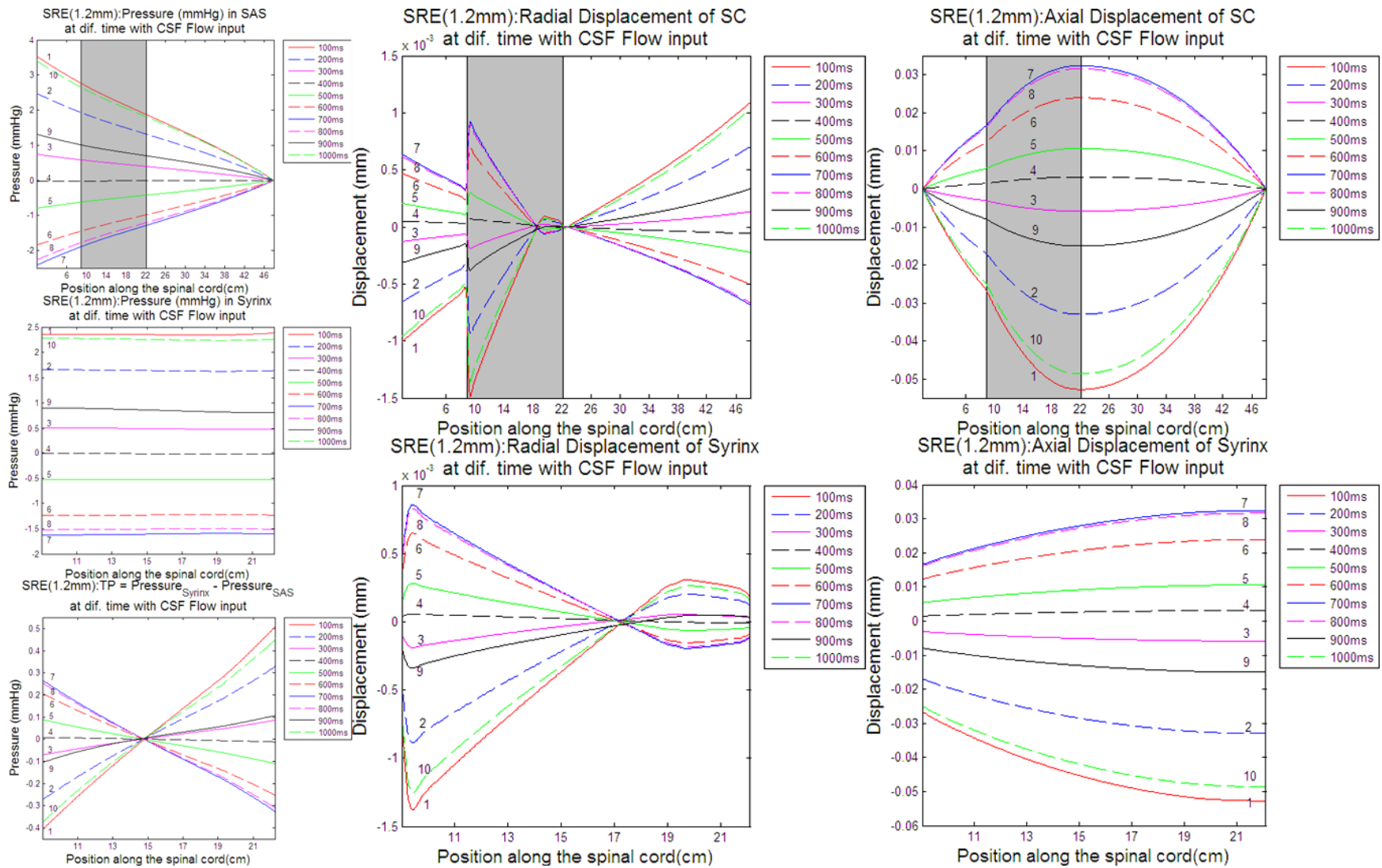


**Figure 4-13: Pressure in SAS and syring along the spine, transmural pressure in the system and displacement of spinal cord and syring in response to excitation of continuous normal CSF pulsation for SRE model at  $t = 0.1, 0.2, \dots, 1$  second, identified as curves 1, 2, ..., 10. Syring is denoted in gray area.**

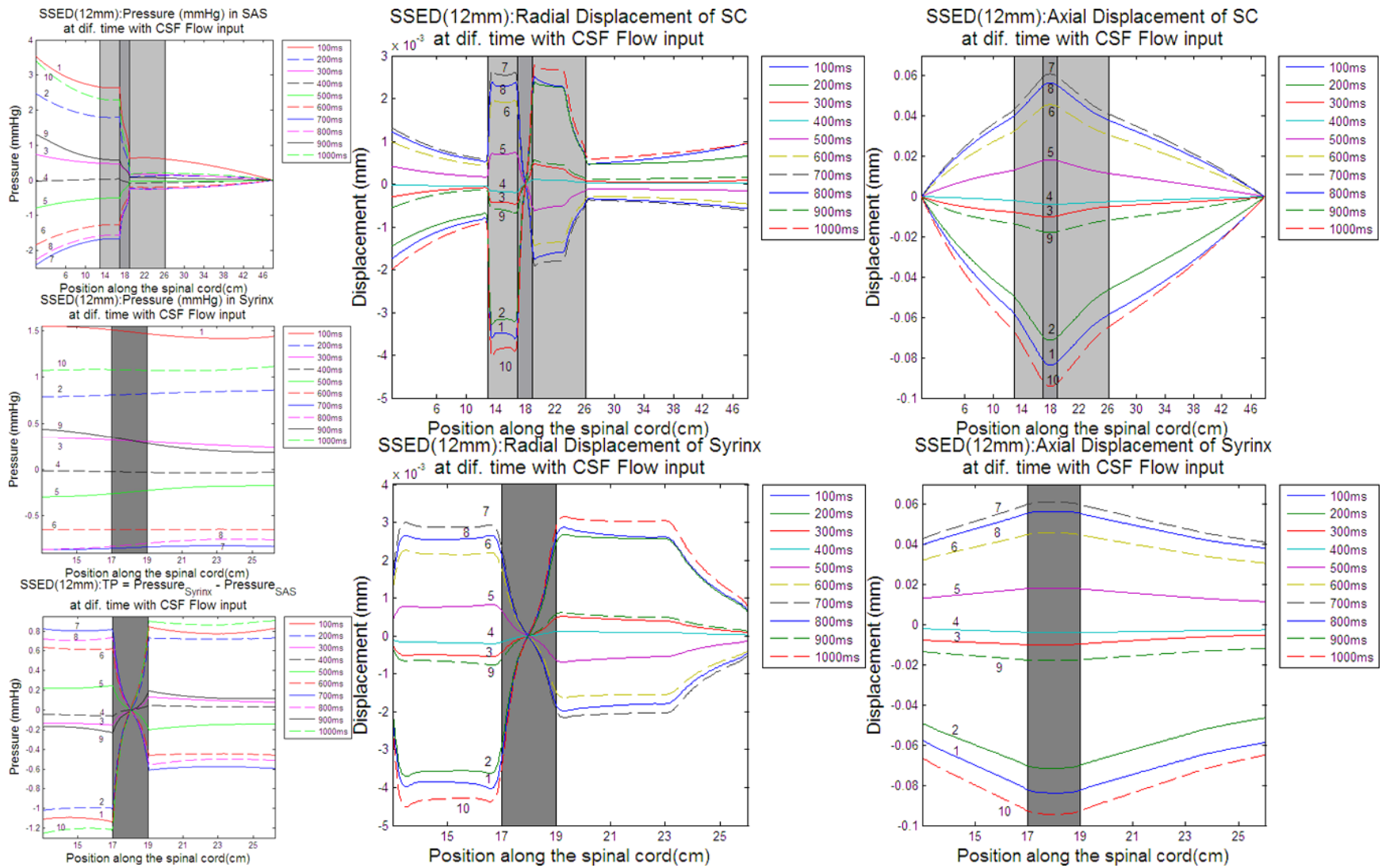


**Figure 4-14: Pressure in SAS and syring along the spine, transmural pressure in the system and displacement of spinal cord and syring in response to excitation of continuous normal CSF pulsation for the SSED model at  $t = 0.1, 0.2, \dots, 1$  second, identified as curves 1, 2, ..., 10. Syring and stenosis are denoted in different gray area.**

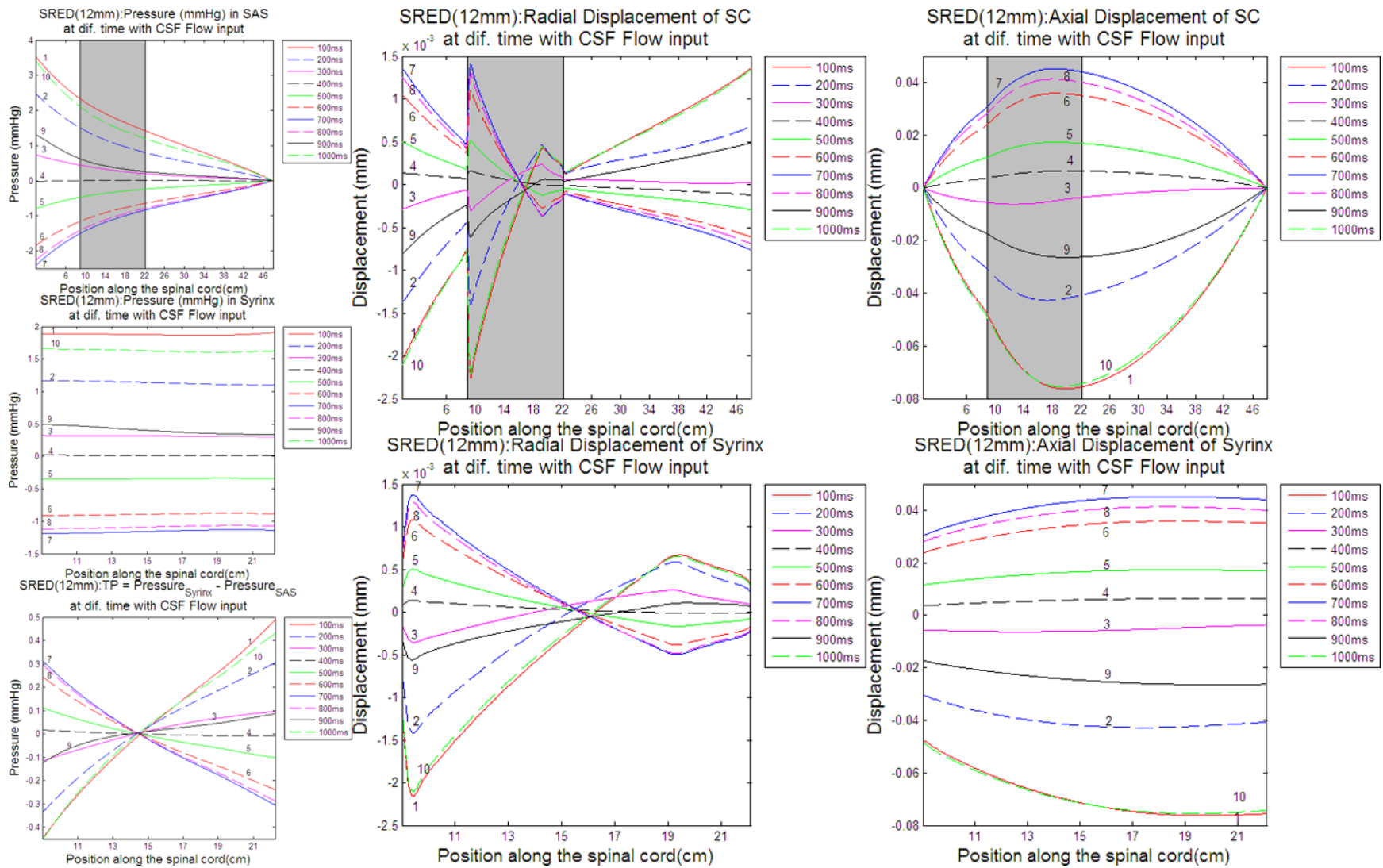


**Figure 4-15: Pressure in SAS and syrx along the spine, transmural pressure in the system and displacement of spinal cord of syrx in response to excitation of continuous normal CSF pulsation for SRED model at  $t = 0.1, 0.2, \dots, 1$  second, identified as curves 1, 2, ..., 10. Syrx is denoted in gray area**

### **4.3.2 Coughing Effect Results**

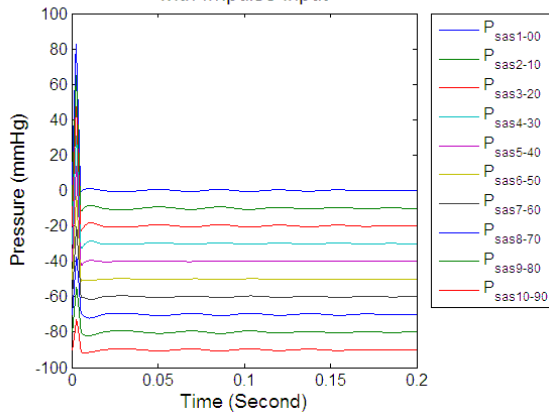
In the above section, the influence of the arterial pulse wave has been discussed. The venous changes caused by coughing will be examined in this section. As introduced in CHAPTER 1, coughing or straining may trigger symptoms of syringomyelia, although none of these causes syringomyelia. Williams et al. had proposed that a sudden increase of SAS pressure caused by coughing, sneezing or Valsalva maneuvers will increase the intracranial pressure, which forces CSF through a patent central canal into the Syrinx. To examine this hypothesis, another separate excitation of a symmetric triangular impulse with duration of 5 ms mimicking a coughing effect was conducted on the models to obtain the pressure distribution and wave propagation through the system. The excitation was applied on the caudal end ( $Y=0$ ) of the CSF flow in the SAS. Pressure in the SAS and syrinx, and displacement of the SC are calculated in the first 200 ms. The time-step is decreased to 0.1 ms (10k Hz sample rate and 2000 time steps) for the coughing effect examination.

#### **4.3.2.1 Pressure changes over time**

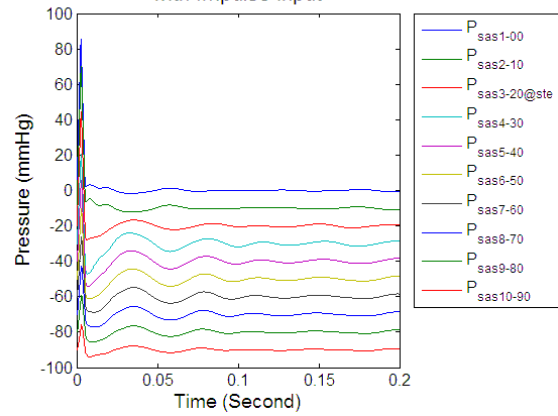
Figure 4-16 shows the pressure in SAS in the first 200 ms at the ten pressure ports for these models. For a healthy spinal system with a rigid dura (CSRD), the transient impulse did not cause too much fluctuation. Pressure attenuated normally and quickly along the spine. When a stenosis appeared in CSF flow in the SAE model, pressure fluctuated before it attenuated, especially at the location near the stenosis. The first boosted peak happened at about 40 ms. However, when a syrinx was present in the stenosis spinal system in the SSE model, although the fluctua-

tion still existed, the pressure amplitude of the fluctuation decreased by a large magnitude compared to that in the SAE model. The fluctuation amplitude near the stenosis location is still the highest in the SAS. And, the first pressure peak after the impulse also was delayed to around 60 ms. Then, after the stenosis was removed from the system with only the syring present in the SRE model, the pressure fluctuation was almost eliminated similar to the CSRD model. Replacing the rigid dura with a distensible material in SRED and SSED models, both wave speeds and pressure amplitude in the first impulse were reduced tremendously, and the attenuation was also slowed down. It can also be noticed that the wavelength of the first impulse along the spine became longer because of the damping value designated in this analysis.

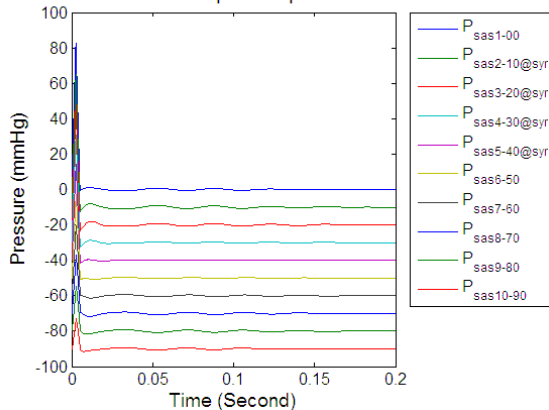
(a) CSRD(1.2mm):Pressure at SAS Pressure Ports with Impulse input



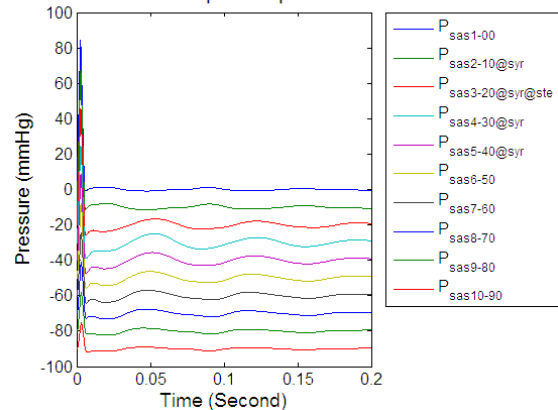
(b) SAE(1.2mm):Pressure at SAS Pressure Ports with Impulse input



(c) SRE(1.2mm):Pressure at SAS Pressure Ports with Impulse input



(d) SSE(1.2mm):Pressure at SAS Pressure Ports with Impulse input



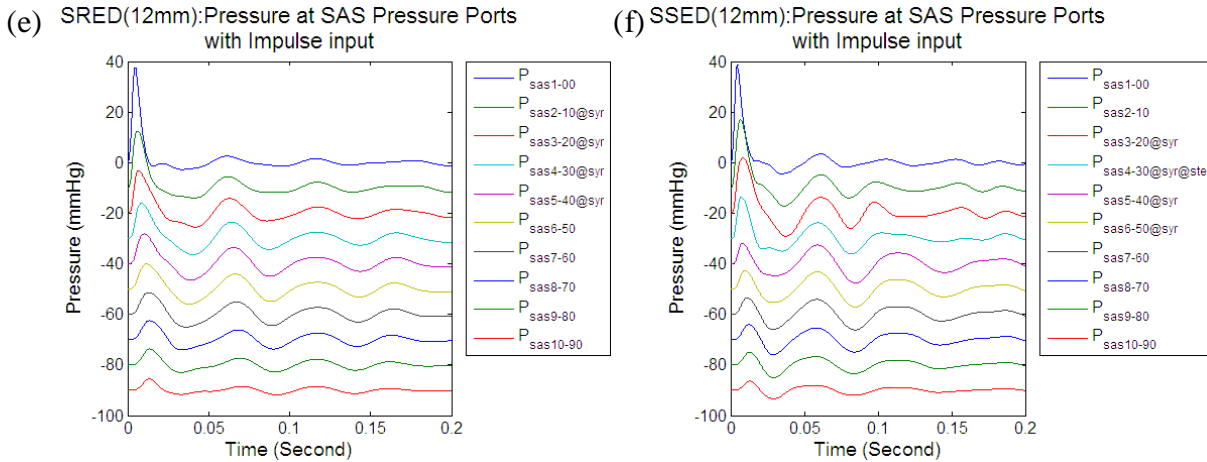


**Figure 4-16: Pressure in SAS at the ten pressure ports position in the first 200 ms in response to 5 ms pressure transient. Pressure at each port has 10 mmHg deductions from the anterior port.**

Figure 4-17 is the plots of pressure in the syrinx within the first 200 ms for models SRE, SSE, SRED and SSED. When the stenosis was present in the spinal canal in the SSE model, the pressure in the syrinx fluctuated and had higher amplitudes after the end of the impulse, especially at the syrinx ports 1 and 2, which are ahead of and at the stenosis location. After the stenosis was removed in the SRE model, the pressure in the syrinx was attenuated almost immediately after the end of the impulse, except at port 4, which is at the tip of the tapered end with a much smaller syrinx cross-sectional area. With a distensible dura in the SRED and SSED models, pressure amplitude was reduced significantly from around 75 mmHg to 24 mmHg at the syrinx port 1. Wave speeds were reduced in both models.

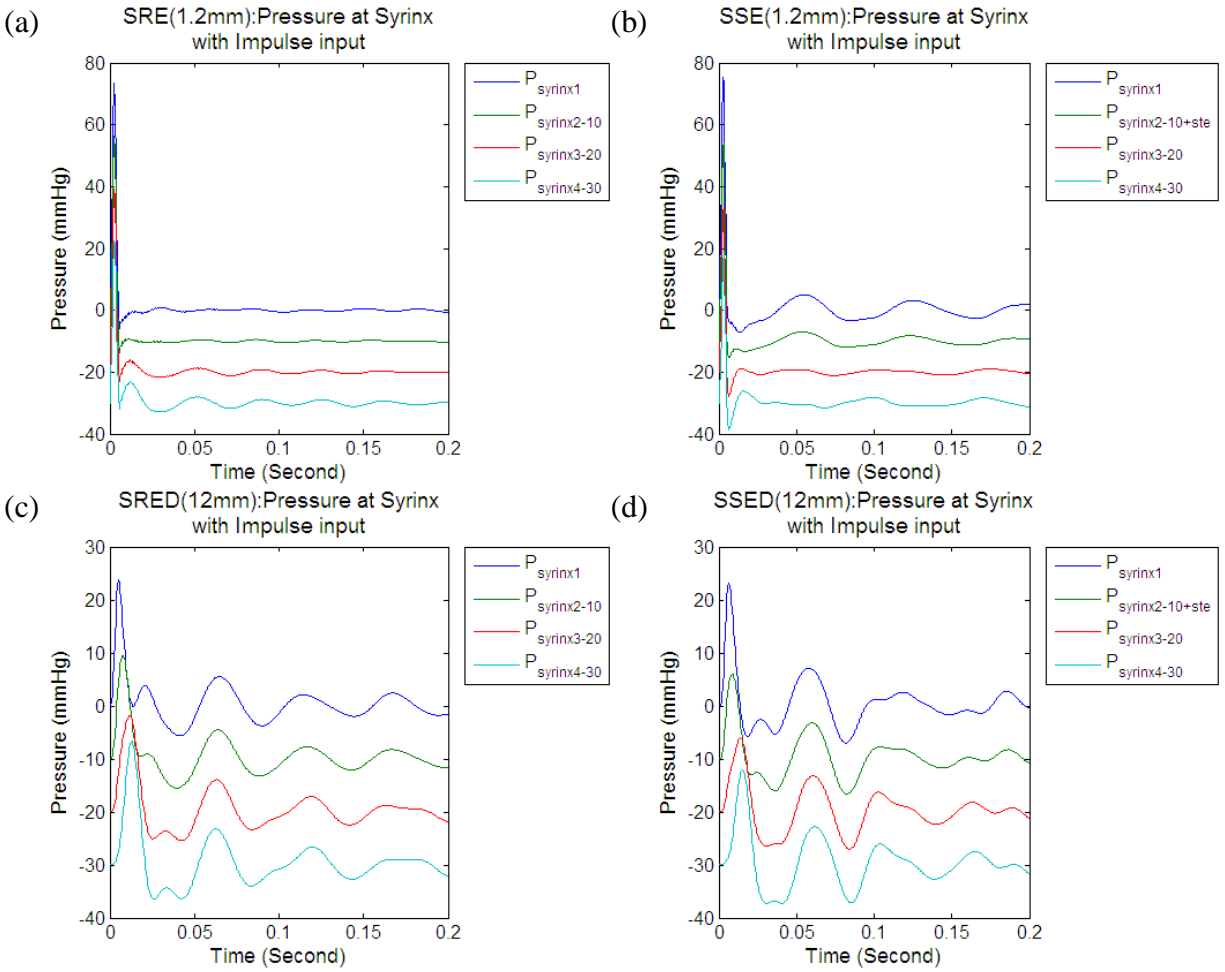


**Figure 4-17: Pressure in syrinx at the ten pressure port positions in the first 200 ms in response to 5 ms pressure transient. Pressure at each port has 10 mmHg deductions from the anterior port.**

#### 4.3.2.2 Longitudinal pressure dissociation (LPD)

Williams had recorded pressure at the lumbar region and the cisterna magna when testing sixteen patients with sharp cough of short duration and limited amplitude. The pressure difference between the two regions suggested that the pulse wave produced by coughing would be attenuated during its travel within the spinal canal, and blockage or narrowing of the pathway would reflect the pressure wave more effectively than that undergoing normal CSF flow [21].

To examine Williams' conclusion, longitudinal pressure dissociation (LPD) was calculated by subtracting the cervical from the lumbar SAS pressure located at the 8<sup>th</sup> pressure port and 1<sup>st</sup> pressure port respectively:

$$LPD(t) = P_{SAS,port 1}(t) - P_{SAS,port 8}(t)$$

Figure 4-18 (a) gives the LPD for the four models with rigid dura in the first 200 ms. To distinguish the difference in the highest pressure time range, the LPD in the first 20 ms is shown in Figure 4-18 (b). The models with stenosis (SAE, SSE) have a higher LPD, where the SAE model has the highest one. The LPD in CSRD and SRE models have almost identical waveform, which attenuated quickly after the end of the impulse. Though both SAE and SSE models have a slower attenuation, LPD attenuated faster in SAE but has higher amplitude.

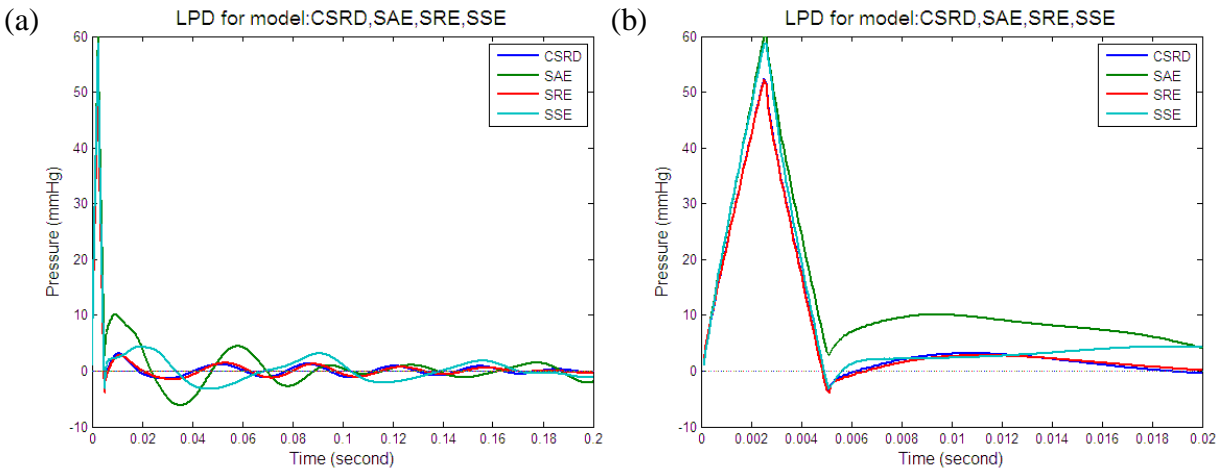


**Figure 4-18: Longitudinal pressure dissociation (LPD) for models with rigid dura. (a): LPD in the first 0.2 second. (b): zoomed in plot of LPD in the first 20 ms.**

Figure 4-19 (a) and (b) are LPD comparison for SRE and SRED, SSE and SSED models in pair, respectively. With a flexible dura, LPD in both models were decreased significantly. Same

as before, with a stenosis presents in the system, the SSED model has higher LPD amplitude than that in SRED.

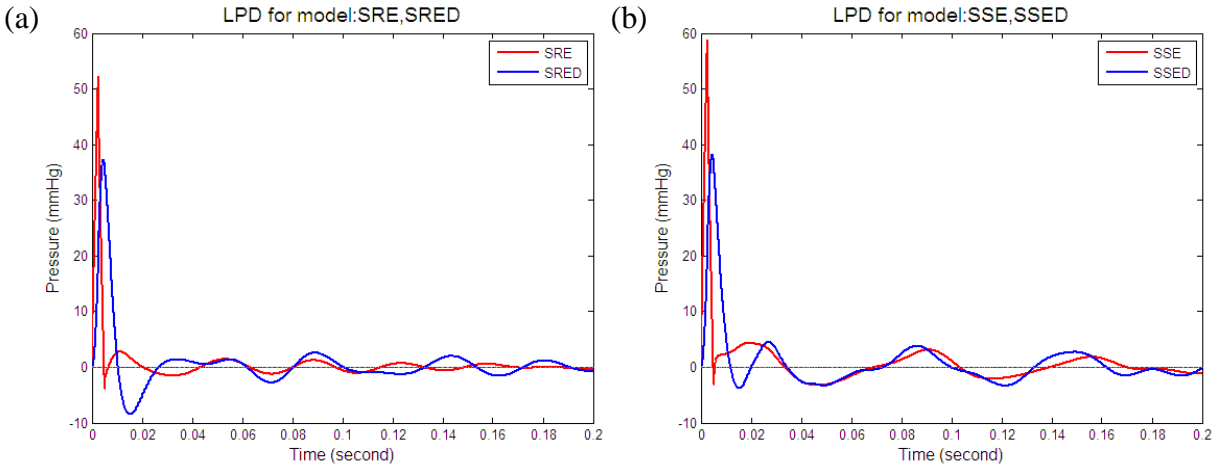


**Figure 4-19: Longitudinal pressure dissociation (LPD) for models with distensible dura. (a): LPD in the first 0.2 second. (b): zoomed in plot of LPD in the first 20 ms.**

#### 4.3.2.3 Transmural pressure (TP)

As introduced in Section 1.5.3, most neurosurgeons agree that an increased intracranial pressure would force CSF to enter the central canal via the obex, which could then form and expand the syrinx. To examine this hypothesis, transmural pressure (TP) in the models with syrinx (SRE, SSE, SRED, and SSED) will be discussed in this section. Transmural pressure (TP) across the syrinx wall was obtained by subtracting pressure in the syrinx from pressure at the same location in the SAS.

$$TP(t) = P_{r,syrinx}(t) - P_{r,SAS}(t)$$

Figure 4-20 shows the TP results for the four models. With a stenosis, TP in the SSE model attenuated slowly with higher amplitude than that in the SRE model. In the SSE model, TP has the highest amplitude at the location ahead of the stenosis, and has the lowest amplitude at steno-

sis location which was around zero. After the stenosis was removed in the SRE model, the TP attenuated fast after the end of impulse. TP at the tapered end of syringe ( $P_{SAS5}$ ) has the highest peak due to the higher pressure in syringe at that location. Similar situation happened in distensible dura models SRED and SSED, except for the TP amplitude is much higher. In addition, frequency of attenuated waveform can be found higher in these two distensible dura models.

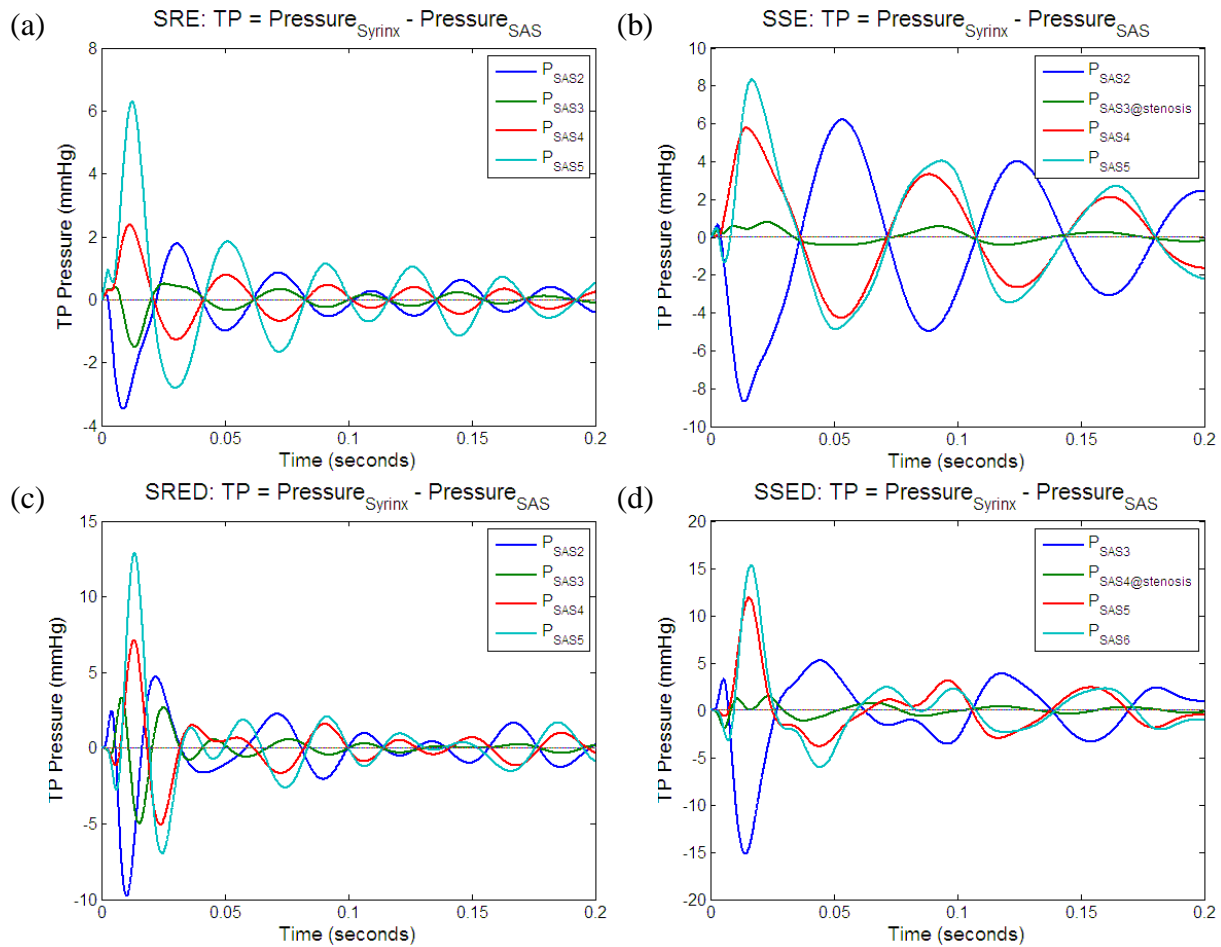


**Figure 4-20: Transmural pressure (TD) for models with syringe in the first 200 ms.**

#### 4.3.2.4 Pressure distribution and wave propagation speed

Same as before, spatial vs. temporal results of the pressure distribution will be examined in this section. Figure 4-21 shows the spatial vs. temporal pressure results in the SAS for the six

models in the first 20 ms. Due to the free output of CSF flow and nonzero damping values for materials in this analysis, no reflection can be observed in either model because pressure wave was attenuated completely before it reached the rostral end of the spine. And, dissipation and oscillation was so severe that the shape of the contoured shade cannot be determined precisely. So the wave speed calculated from these plots has a much bigger error. An arrowed line was marked in each plot to indicate the slope for the wave speed calculation.

By calculating the slope of the contoured shade, wave speed was calculated to be 343 m/s in the CSRD model. With the stenosis present in the SAE model, pressure appeared to be stronger due to the reflection by the stenosis. At the stenosis region from 13 cm to 15 cm, wave speed was decreased significantly, and increased immediately after it passed this region. Wave speed in the SAE model was calculated to be 266 m/s, which was slower than that in the CSRD model. When the syrinx formed in the system in SSE model, pressure ahead of the stenosis was weaker, and the wave speed was 218 m/s. After the stenosis was removed in the SRE model, wave propagation was boosted due to the cleared SAS pathway. The wave speed in the SRE model was calculated to be 369m/s, which is similar to that calculated in the CSRE model. On the other hand, the pressure in the SRE also has a similar distribution as that in the CSRD model.

With a distensible dura in the SRED and SSED models, pressure dissipation and attenuation became more severe. And wave speed in both models slowed down significantly to 32.4 m/s and 30 m/s, respectively, due to the absorption of the soft material. Pressure reflection at the stenosis site can be observed in the SSED model.

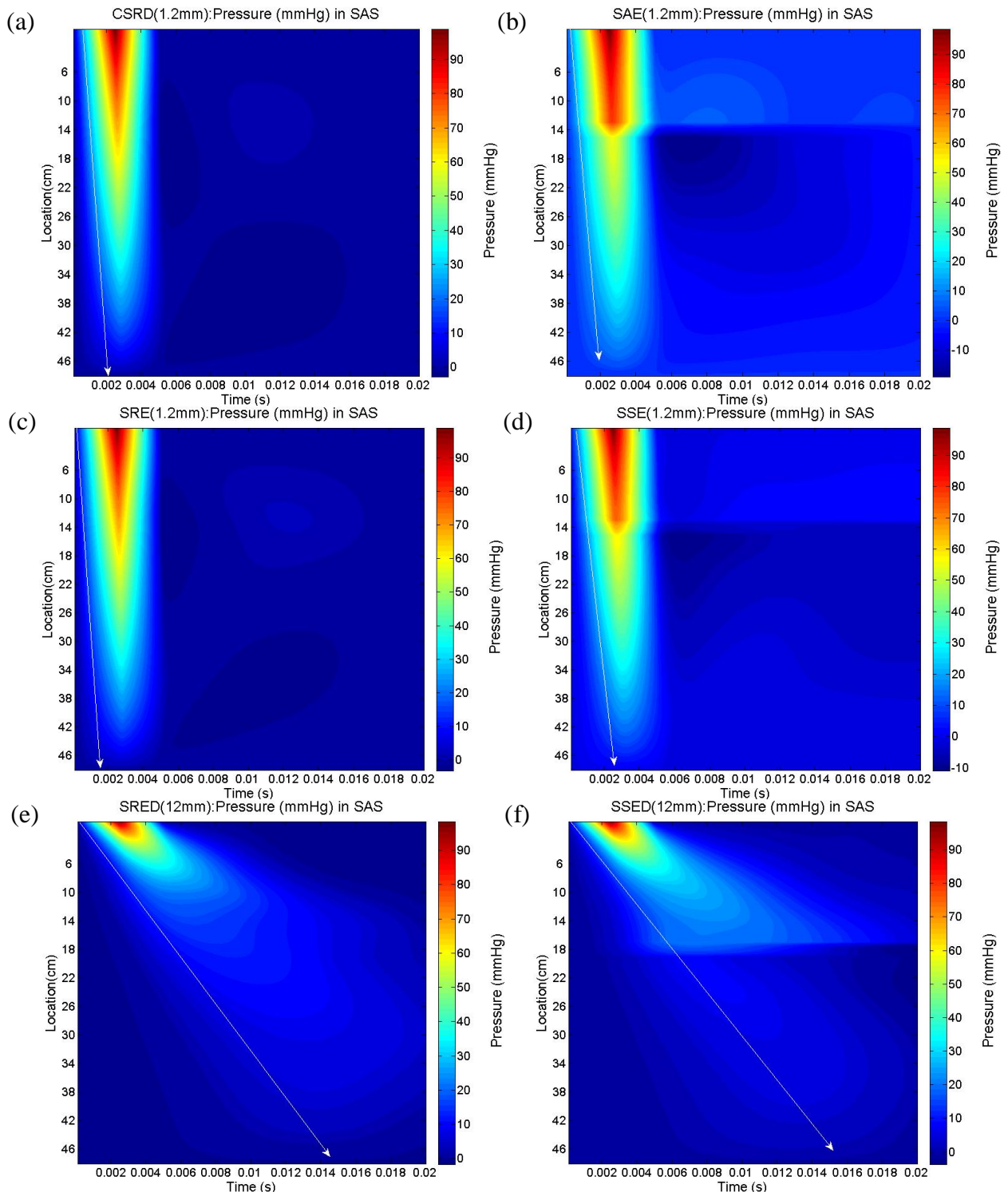


**Figure 4-21: Spatial vs. temporal pressure in SAS results in the first 30 ms in response to transient impulse.**

Figure 4-22 shows the spatial vs. temporal pressure in the syringe for mode SRE, SSE, SRED and SSED. The wave speed in the syringe in the SSE model is 220 m/s, which is slower than that in the SRE model 330 m/s. The wave speed in the SSE model has a decrease at the stenosis site at 13 cm to 15 cm, and pressure ahead of the stenosis was stronger due to the reflection by the stenosis. A distensible dura also decreased the wave speed in the syringe, which became 33 m/s and 25.4 m/s for SRED and SSED models, respectively. Wave speed was decreased at the stenosis site at 17 to 19 cm in the SSED model, and reflection caused by the further end of the syringe can be observed in both models.

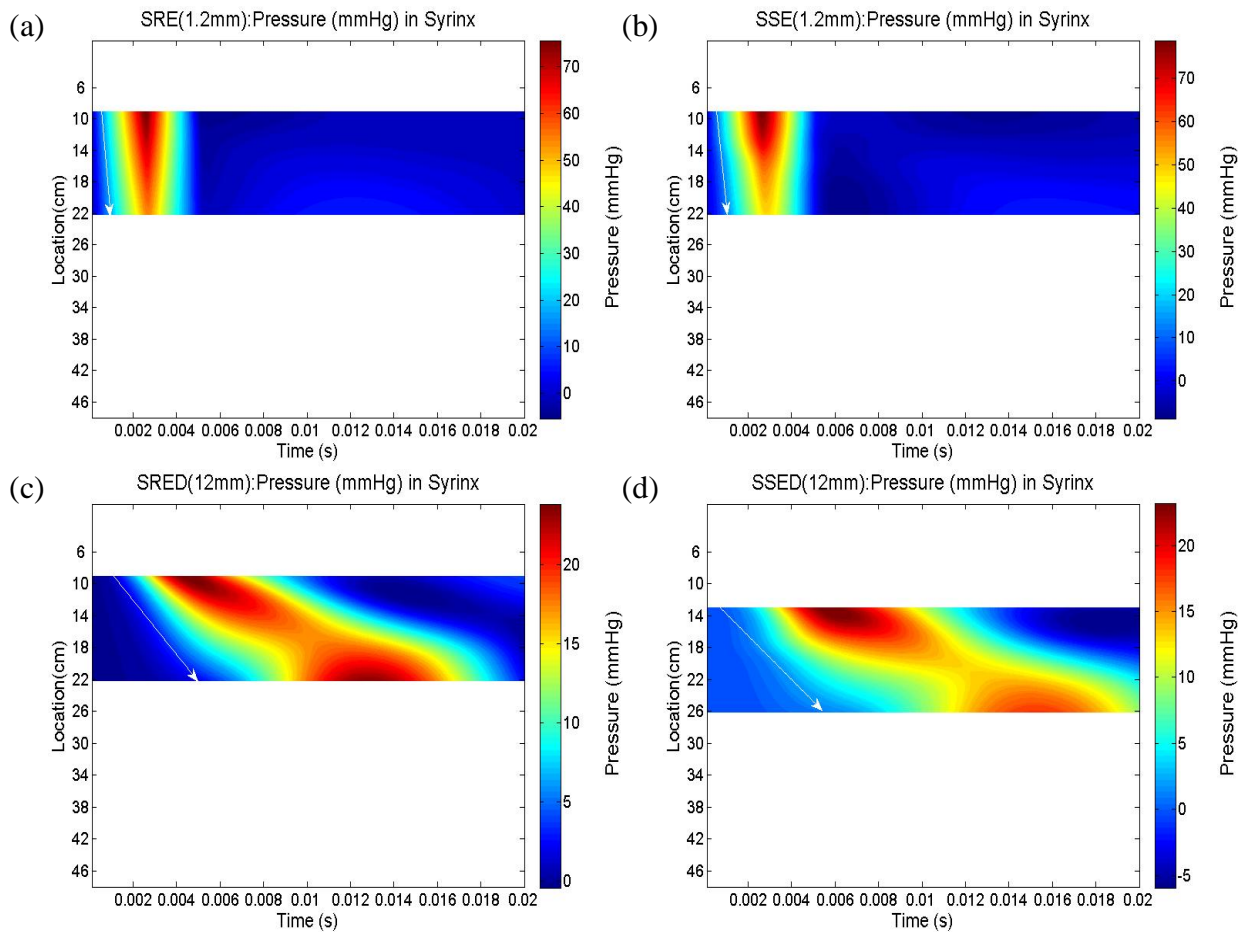


**Figure 4-22: Spatial vs. temporal pressure in syringe result in the first 30 ms in response to transient impulse.**

#### 4.3.2.5 Pressure and displacement at different times

Same as the arterial pulse analysis in Section 4.3.1, pressure in the SAS and syrxinx and displacement of the spinal cord and syrxinx will be examined in this section. Pressure and displacements in the first 50 ms for the rigid dura models and in the first 100 ms for the distensible dura models are given in Figure 4-23 to Figure 4-28.

For a healthy spinal system in the CSRD model in Figure 4-23, the sudden shock attenuated quickly after the end of the impulse, then the pressure distributed along the spine in the SAS sinusoidally. A similar thing happened to the radial displacement of the spinal cord.

However, when a stenosis formed in the spinal canal in the SAE model in Figure 4-24, the pressure in the SAS model along the spine didn't attenuate immediately and had higher amplitude in the first 50 ms as compared to the CSRD model. The deformation of the spinal cord is similar to that influenced by the arterial pulse as discussed in 4.3.1.3. The radial displacement moved into two opposite phases about the stenosis. Within the first 25 ms, the spinal cord ahead of the stenosis shrank, while the part behind the stenosis distended, and the displacement reversed after then to around 100 ms.. Meanwhile, the spinal cord also moved axially to the direction of spinal cord shrank region

When the syrxinx was formed in the spinal cord in the SSE model in Figure 4-25, the deformation of the spinal cord at syrxinx region was boosted due to the synchronous distension or contraction of the syrxinx. Displacement in the SSE model was much higher than in the SAE model. Same as in the SAE model, the transmural pressure is positive at the distended area, and negative

at the compressed region. Both spinal cord and syrinx moved axially to the direction of shrank area. The tapered end of syrinx relieved the deformation of the spinal cord and the syrinx.

After the stenosis was removed in the SRE model in Figure 4-26, pressure distribution in the SAS became similar to that in the healthy spine model CSRD. The deformation of the spinal cord became similar to the CSRD model, except for the boosted radial displacement within the syrinx area, due to the synchronous deformation of the syrinx.

With a distensible dura in SRED in Figure 4-27 and SSED models in Figure 4-28, both the pressure and displacement were similar to that in the SRE and SSE models, but with a slower attenuation and a higher pressure amplitude within the first 100 ms.

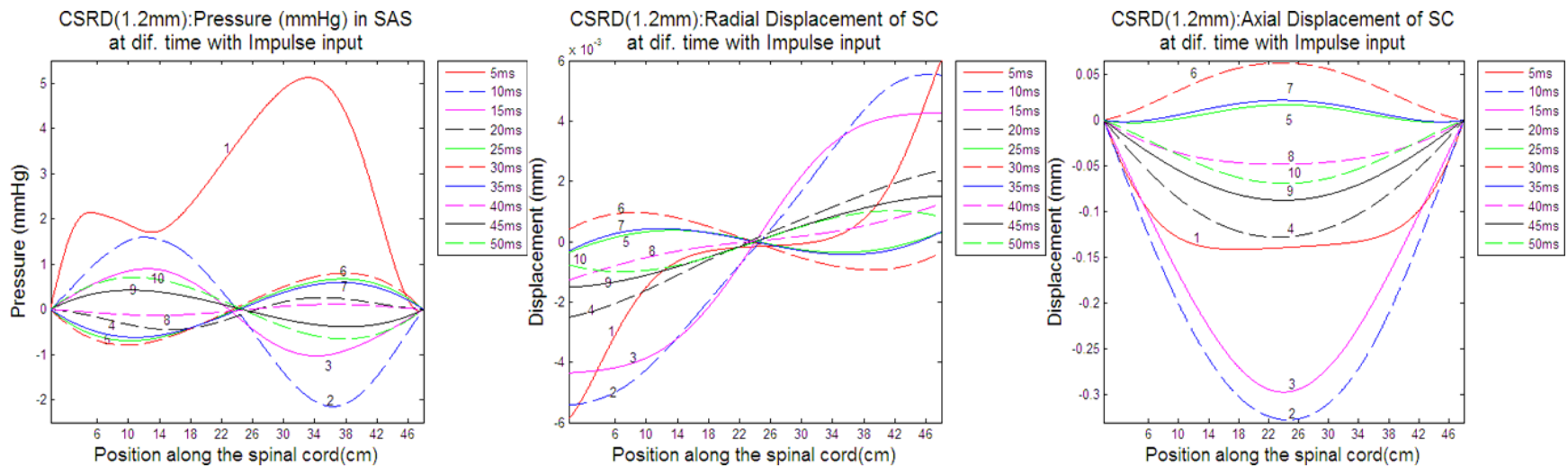


**Figure 4-23: Pressure in SAS along the spine and displacement of spinal cord in response to excitation of 5 mm triangular impulse for CSR models at t = 5, 10, ..., 50 ms, identified as curves 1, 2, ..., 10.**

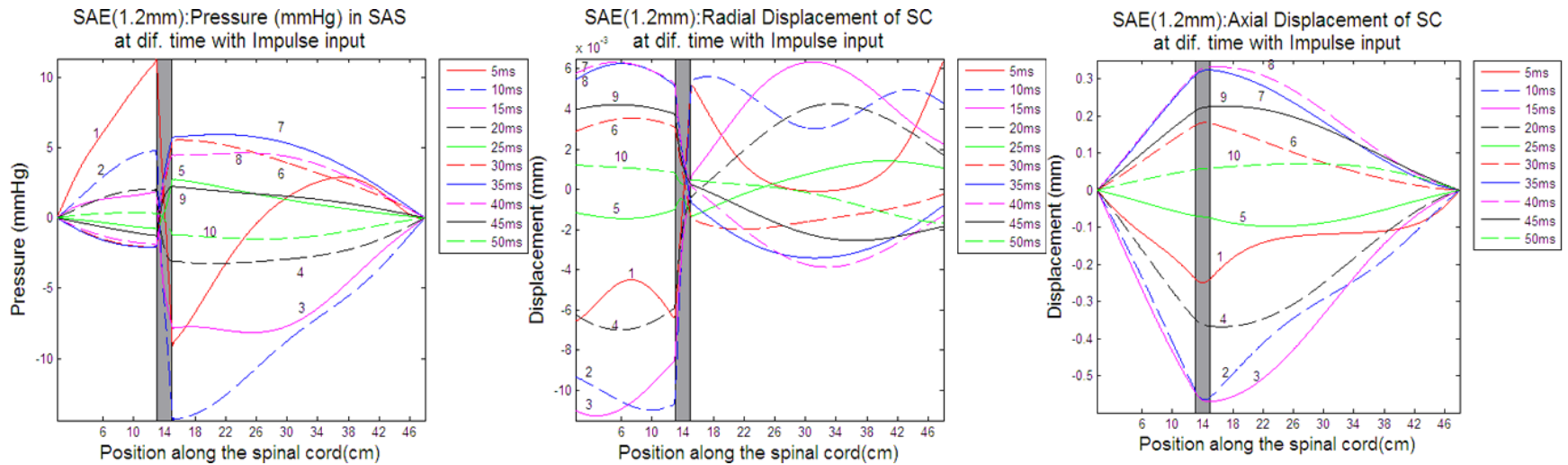


**Figure 4-24: Pressure in SAS along the spine and displacement of spinal cord in response to excitation of 5 mm triangular impulse for SAE models at t = 5, 10, ..., 50 ms, identified as curves 1, 2, ..., 10.**

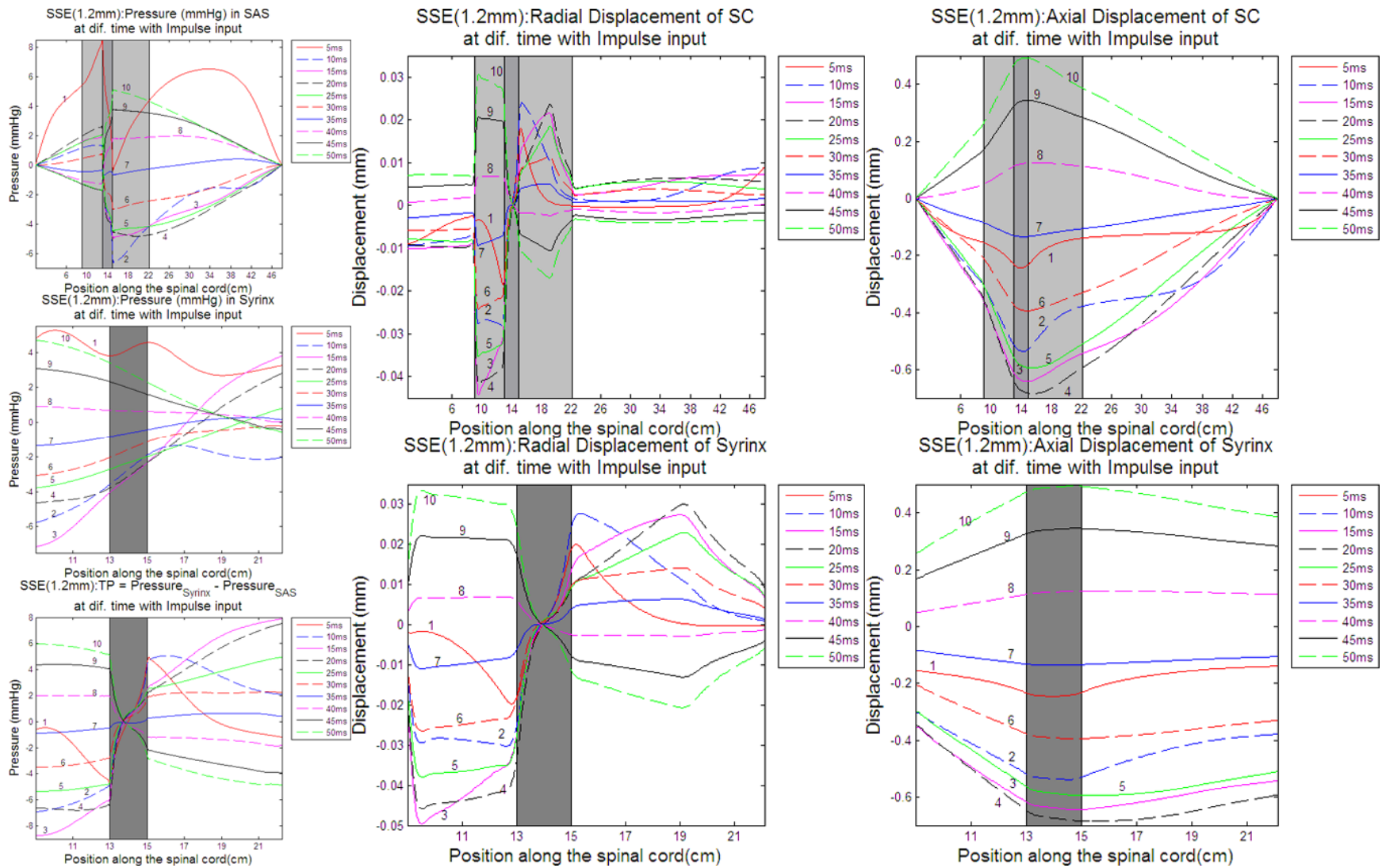


**Figure 4-25: Pressure in SAS and syring along the spine, transmural pressure in the system and displacement of spinal cord and syring in response to excitation of 5 mm triangular impulse for the SSE model at  $t = 5, 10, \dots, 50$  ms, identified as curves 1, 2, ..., 10. Syring and stenosis are denoted in different gray area.**

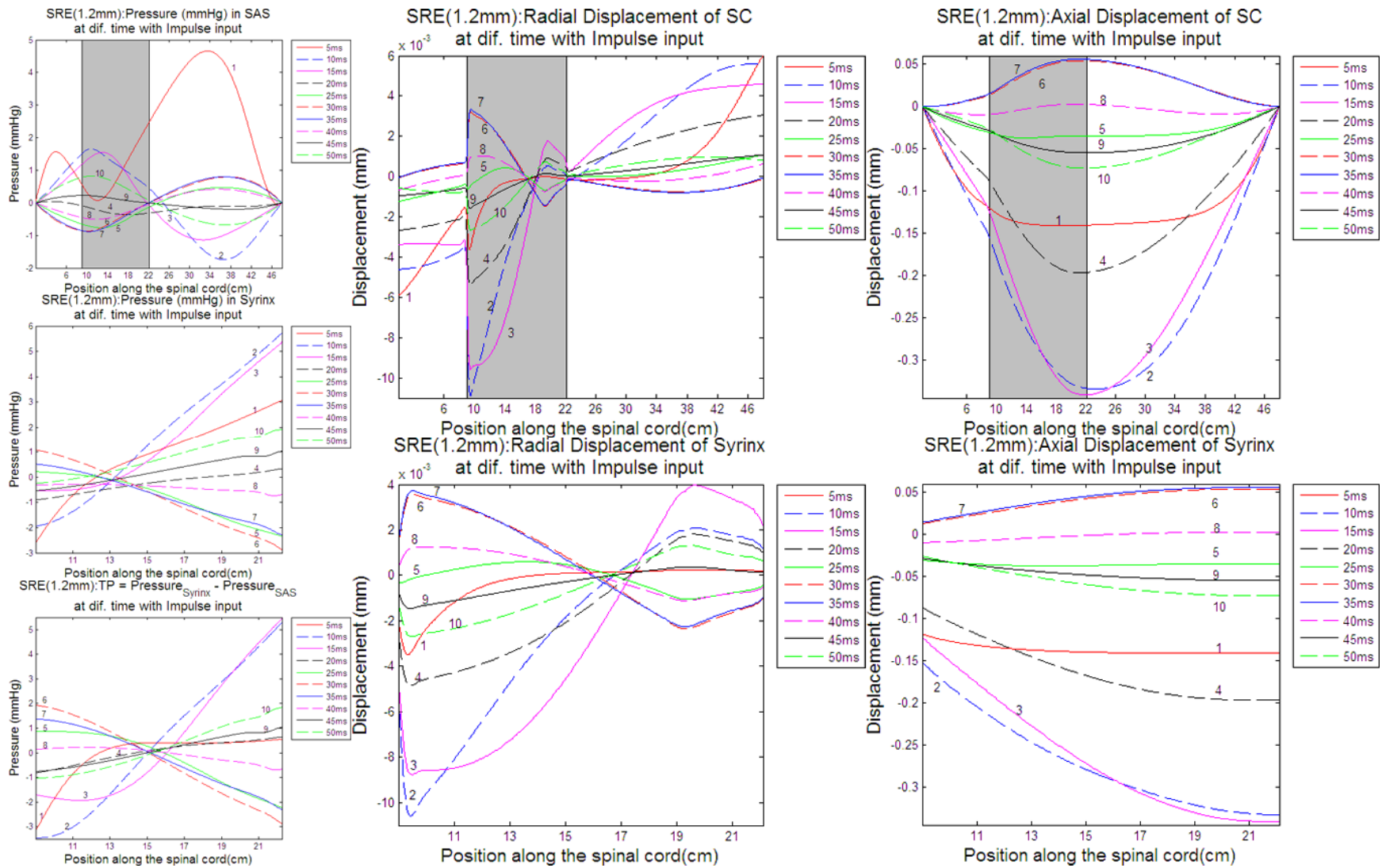


**Figure 4-26: Pressure in SAS and syrinx along the spine, transmural pressure in the system and displacement of spinal cord and syrinx in response to excitation of 5 mm triangular impulse for the SRE model at  $t = 5, 10, \dots, 50$  ms, identified as curves 1, 2, ..., 10. Syrinx and stenosis are denoted in different gray area.**

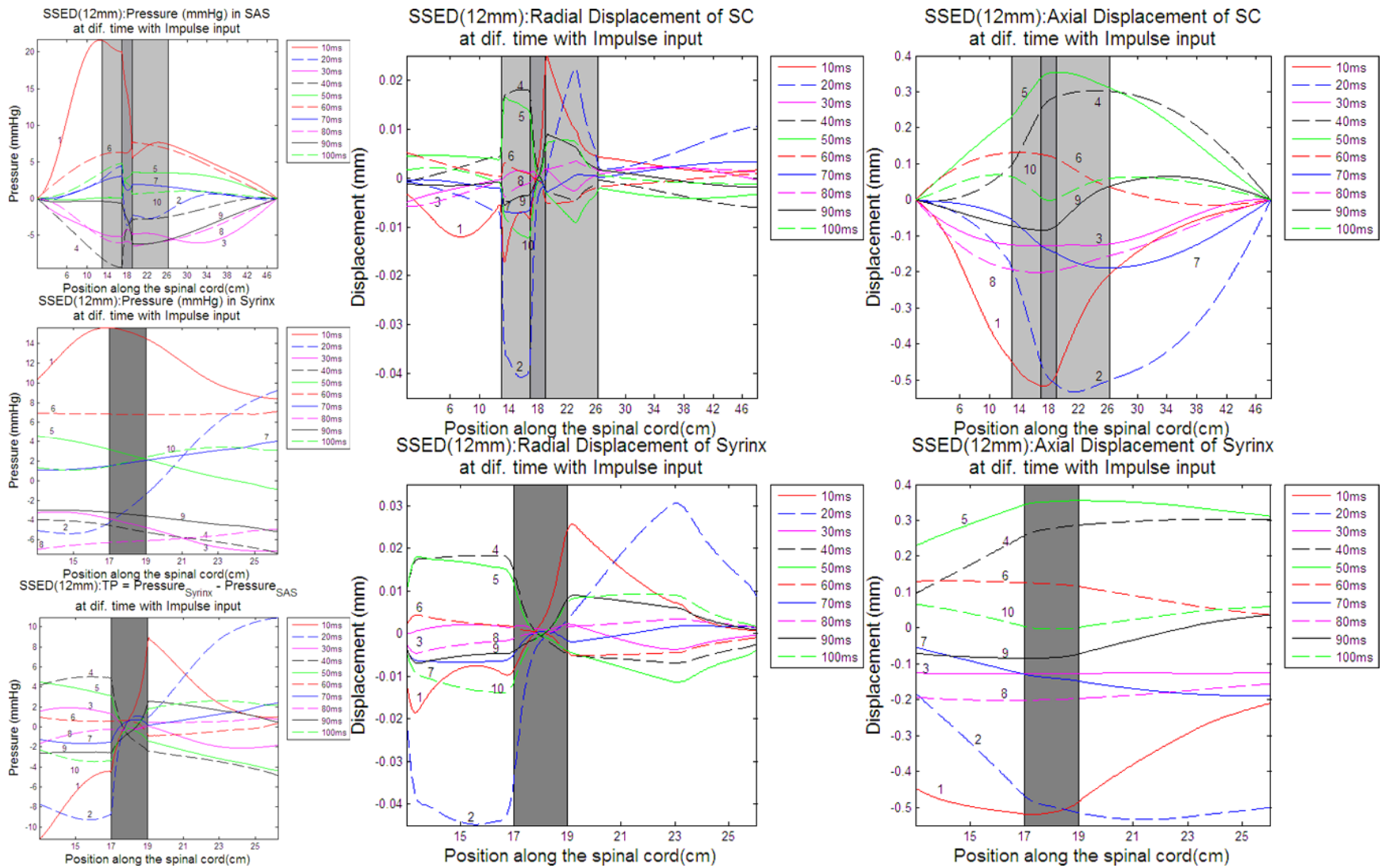


**Figure 4-27: Pressure in SAS and syring along the spine, transmural pressure in the system and displacement of spinal cord and syring in response to excitation of 5 mm triangular impulse for the SSED model at  $t = 10, 20, \dots, 100$  ms, identified as curves 1, 2, ..., 10. Syring and stenosis are denoted in different gray area.**

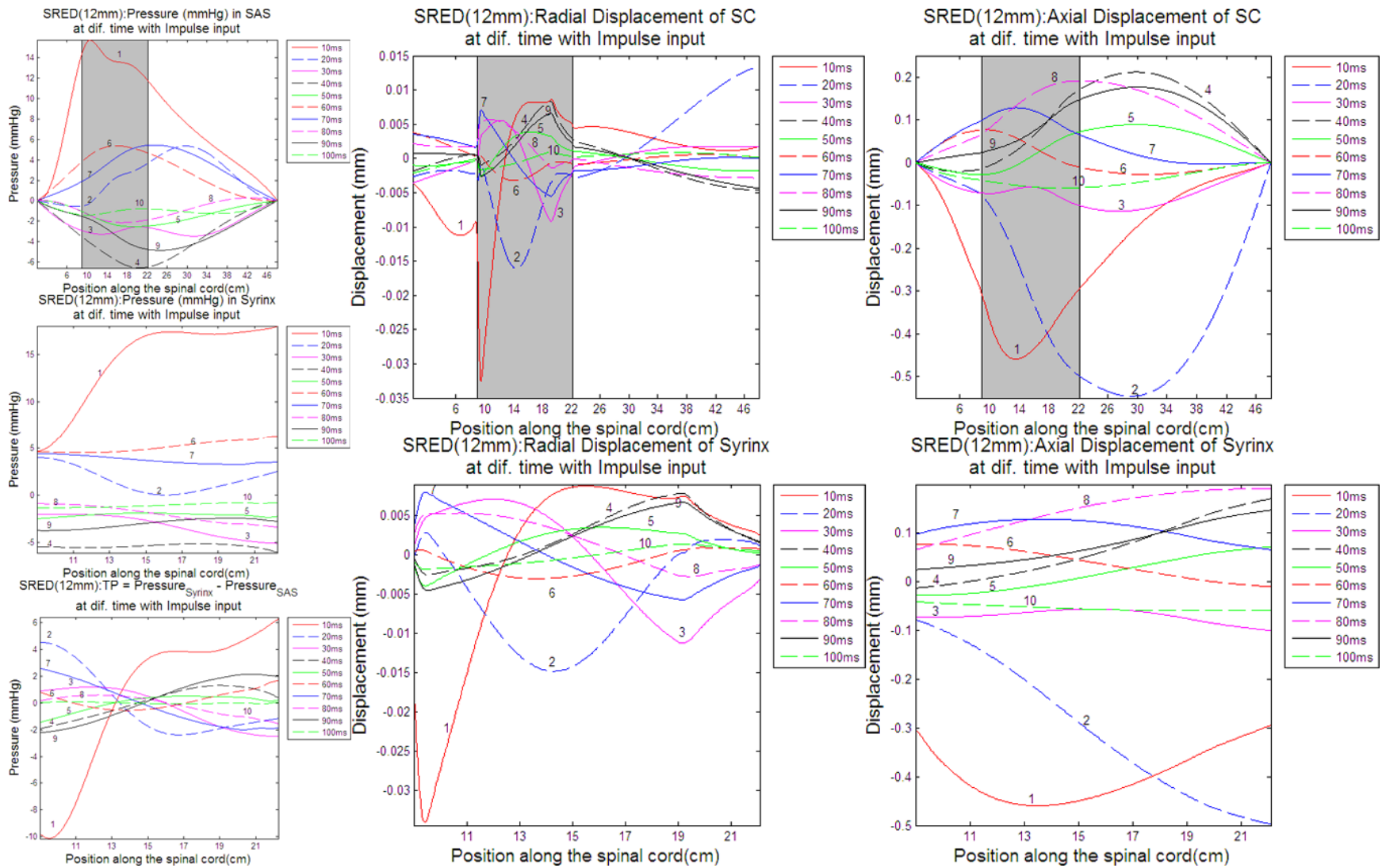


**Figure 4-28: Pressure in SAS and syring along the spine, transmural pressure in the system and displacement of spinal cord and syring in response to excitation of continuous normal CSF pulsation for the SRED model at  $t = 10, 20, \dots, 100$  ms, identified as curves 1, 2, ..., 10. Syring and stenosis are denoted in different gray area.**

#### 4.4 Conclusion and Discussion

Consistent with the in vitro study. The models were defined based on the *in vitro* models constructed by Martin et al. (2008) in terms of geometry, material properties, excitation type and measurements. But, unlike the *in silico* models, the *in vitro* models were not exactly axisymmetric structures, and had more complex boundary conditions at either end. These will complicate the results to some degree.

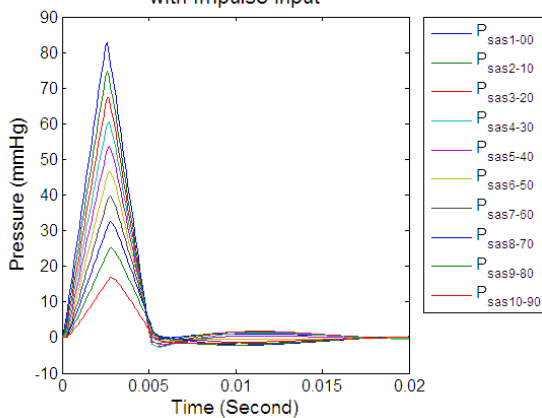
Influence of stenosis and syrxinx. Analyses of six models under one uniform continuous excitation and a transient impulse have been made separately above. Overall, the results indicated that the majority of pressure changes in the SAS happened near the stenosis (SAE, SSE and SSEED). The magnitude of pressure changes was smaller when a syrxinx is present (SSE, SSEED). After the surgery has the stenosis removed in the SRE model, the pressure environment returned to normal like that in the healthy spinal system (CSR model). In addition, the existence of the stenosis also slowed down the pressure wave propagation speed in the SAS and syrxinx.

'Suck and Slosk'. In the 'Suck and Slosk' theory proposed by Williams, he proposed that dilatation of the syrxinx could be caused by the high cranial – spinal pressure dissociation. As discussed in 4.3.2.2 and 4.3.2.3, with a stenosis present in the SSE model, the magnitude of TP is higher than that in the SRE model, where LPD in the SRE model is also lower than that in the SSE and SAE models. This means the stenosis could cause a high LPD and a high TP, where a high TP could cause the dilatation of the syrxinx. Thus, the result supports the theory.

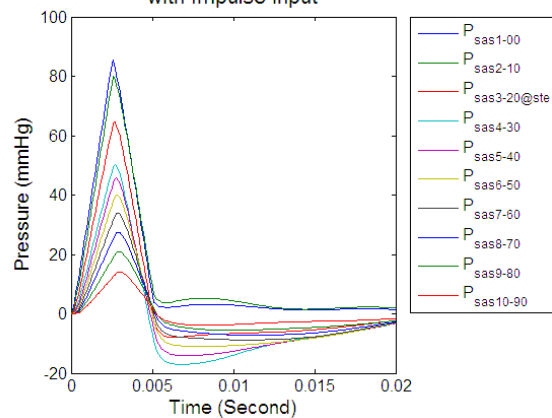
**Venturi Effect.** According to the Venturi effect, when a fluid flows through a constricted section of pipe, the fluid velocity must increase to satisfy the equation of continuity, while its pressure must decrease due to conservation of energy.

From the discussion in Section 4.3.1.1, with a continuous, periodic pulse excitation, pressure at the stenosis site dropped significantly in the SAE, SSE and SSED models, which is consistent with the Venturi Effect explanation. But, with a transient impulse excitation as discussed in Section 4.3.2.1, the pressure at each port was complicated. For an impulse excitation, the pressure waveform after the first pulse is a combination of forward and backward pressure waves. So, to test the Venturi effect, pressure within the first impulse was examined. Figure 4-29 is the pressure waveform of the first pulse for the four rigid dura models under a triangular impulse. It can be found that at the stenosis site in the SAE and SSE models, the pressure amplitude was smaller than that in CSRD and SRE models. Thus, under a transient impulse, the pressure in the SAS in these models is consistent with the Venturi effect explanation.

(a) CSRD(1.2mm):Pressure at SAS Pressure Ports with Impulse input



(b) SAE(1.2mm):Pressure at SAS Pressure Ports with Impulse input



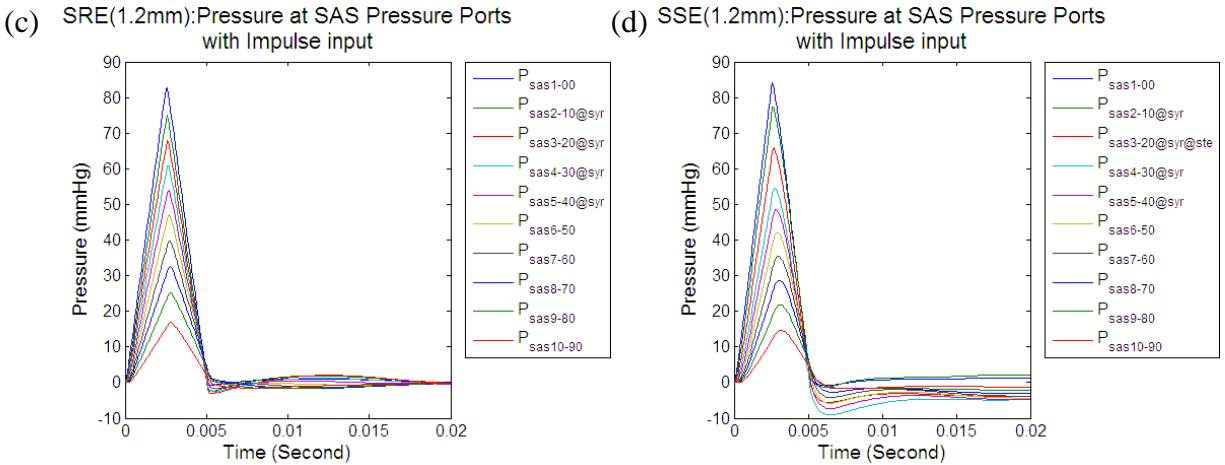


**Figure 4-29: The first impulse of pressure in SAS at the ten pressure port positions in the first 20 ms in response to 5 ms pressure transient.**

**Diastolic valve mechanism and spinal cord displacement (SSE only).** In papers published by Martin et al. (2008) a diastolic valve mechanism effect was introduced. A draft from their papers about this theory is shown in Figure 4-30. According to Martin et al. the syrinx was compressed in systole, which reduced resistance to caudal CSF movement in the SAS through the stenosis. At the onset of diastole, the syrinx was pulled outward by a large positive TP in this region that resulted in greater resistance to rostral directed CSF flow. Fluid was then sucked rostrally through the syrinx from its caudal side rather than through the SAS [5, 43].

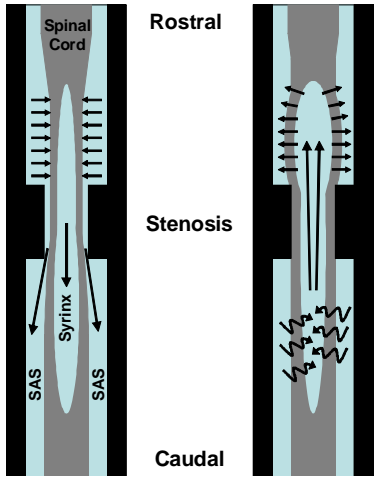


**Figure 4-30: Valve-like action in systole (left) and diastole (right) of the syrinx in SC [43].**

The discussion in 4.3.1.3 and 4.3.2.5 about the pressure, transmural pressure and displacement at different time along the spine and syrinx proved this theory. From these sections, the transmural pressure in SSE model was positive in the distended area and negative in the compressed area. Meanwhile, both the spinal cord and the syrinx moved axially to the direction of the distended part at the same time. These consist with this conclusion drawn by Martin et al.

**Wave Speed.** Because of the nonzero damping value for the spinal aqueduct material in these models, dissipation and oscillation were more, which made it was hard to determine the wave speed. So the wave speeds calculated in these analyses have a much higher error. However, the influence of the stenosis and syrinx on the wave speed in the *in silico* study were consistent with the *in vitro* result. A summary of the wave speed calculated in the *in silico* models and the *in vitro* models measured by Martin et al. (2008) are given in Table 4-3. From these result, it can be found that the existence of stenosis reduced the wave speed in a great level (SSE and SAE). And with a distensible dura (SSED and SRED), the wave speed reduced significantly. On the other hand, the distensible dura also absorbed the pressure wave, which caused a higher dissipation.

**Table 4-3: Summary of wave speeds for the six models measured in the *in silico* and *in vitro* models**

Model	SAS wave speed (m/s)		Syrinx wave speed (m/s)	
	<i>in-silico</i>	<i>in vitro</i>	<i>in-silico</i>	<i>in vitro</i>
CSRD	343	No Data	N/A	No Data
SAE	266	169	N/A	N/A
SRE	369	399	330	680
SSE	218	155	220	118
SRED	32.4	No Data	33	No Data
SSED	30	24	25.4	25

## CHAPTER 5 FUTURE STUDIES

There are various spinal system diseases that are believed to be somehow correlated with changes in the effective elastic properties of the spinal aqueduct and blockage in the normal CSF pathway; syringomyelia is one such disease. In this thesis *in silico* simplified models were developed in the finite element language, ANSYS, to simulate the dynamic mechanical response of the spinal system under realistic excitation conditions with and without pathological conditions present. While some conclusions can be derived from the present work, additional future studies could still be useful.

First of all, the material properties of the spinal components need to be closer to the real spinal tissue. In this study, the damping value and the Poisson's ratio of the spinal aqueduct components were estimated based on the available reference material and different *in silico* trials. Obtaining more accurate experimental values, if possible, would be beneficial.

In this study, to simplify the analysis, the spinal system was built as an axisymmetric model. However, in the real case, the spine has a curved shape, and the cross-section area of the spinal cord and the SAS varies along the spine. Also, the boundary conditions in the *in silico* models were simplified relative to the real spine. In the real cases, biological tissue associated with the spinal system can cause a pressure wave reflection within the SAS. But in this study, to simplify the analysis, the output end of the fluid was given a free boundary condition.

Additionally, in the case of blockage in the CSF pathway, the size of the stenosis, especially the blockage ratio of the stenosis, has an important effect. Also, the location of the stenosis can

cause different pressure environments in the SAS and/ or syrinx. So, greater examination of different sizes and locations of the stenosis could be useful.

Overall, to better understand the hydrodynamic mechanism of the spinal system diseases, especially syringomyelia, more research is needed. And, all of these studies are presented with the hope that this may be helpful towards improving the diagnosis and treatment of persons with spinal system diseases associated with elastic properties changes and blockage in the CSF pathway.

## CITED LITERATURE

1. Henry Gray, C.D.C., *Gray's Anatomy*. 30th ed. 1984.
2. Martin, B.A., *An Experimental Investigation of the Hydrodynamic and Biomechanical Environment Present in Syringomyelia*, in *Mechanical Engineering*. 2005, University of Illinois at Chicago: Chicago.
3. Tortora, G.J., *Principles of Human Anatomy*. Ninth ed. 2002: John Wiley & Sons, Inc.
4. Wikipedia. *Vertebral column*. [cited 2010 Jan 27th]; Available from: [http://en.wikipedia.org/wiki/Vertebral\\_column](http://en.wikipedia.org/wiki/Vertebral_column).
5. Martin, B.A., *An Experimental Investigation of the Hydrodynamic and Biomechanical Environment Present in Syringomyelia*, in *Mechanical Engineering*. 2008, University of Illinois at Chicago: Chicago.
6. Marieb, E.N., *Human Anatomy & Physiology*, ed. 5th. 2000: Benjamin-Cummings Publishing Company.
7. ADAM. Available from: <http://www.nlm.nih.gov/medlineplus/ency/imagepages/19470.htm>.
8. Brodbelt, A.R. and M.A. Stoodley, *Post-traumatic syringomyelia: a review*. J Clin Neurosci, 2003.
9. Maton, A., et al., *Human Biology and Health*. 1993: Englewood Cliffs, New Jersey, USA: Prentice Hall.
10. Martin, B.A., et al., *Syringomyelia hydrodynamics: an invitro study based on in vivo measurements.*, in *ASME Journal of Biomechanical Engineering* 127. 2005. p. 1110-1120.
11. Wikipedia. *Cerebrospinal fluid*. [cited 2010 Jan 27th]; Available from: [http://en.wikipedia.org/wiki/Cerebrospinal\\_fluid](http://en.wikipedia.org/wiki/Cerebrospinal_fluid).
12. The\_University\_of\_Warwick. *Syringomyelia*. Available from: <http://www2.warwick.ac.uk/study/csde/gsp/eportfolio/directory/pg/esebb/research/syringomyelia/>.
13. Klekamp, J. and M. Samii, *Syringomyelia: diagnosis and treatment*. 2002: Springer.
14. Wikipedia. *Young's Modulus*. Available from: [http://en.wikipedia.org/wiki/Young%27s\\_modulus](http://en.wikipedia.org/wiki/Young%27s_modulus).
15. NIND. *syringomyelia information page*. [cited 2010 Jan. 28]; Available from: <http://www.ninds.nih.gov/disorders/syringomyelia/syringomyelia.htm>.
16. Wikipedia. *Syringomyelia*. [cited 2010 Jan 18th]; Available from: <http://en.wikipedia.org/wiki/Syringomyelia>.
17. Staff, M.C. *Syringomyelia Symptoms*. [cited 2010 Jan 28th]; Available from: <http://www.mayoclinic.com/health/syringomyelia/DS01127/DSECTION=symptoms>.
18. WACMA. *A Case of a Temporary ACM/ Syrinx*. Available from: <http://www.pressenter.com/~wacma/bernie.htm>.

19. Anson, J.A., E.C. Benzel, and I.A. Awad, *Syringomyelia and the Chiari Malformations*. 1997: The American Association of Neurological Surgeons.
20. Williams, B., *Simultaneous Cerebral and Spinal Fluid Pressure Recording I. Technique, Physiology, and Normal Results*. Acta Neurochirurgica, 1981. **58**: p. 167-185.
21. Williams, B., *Cerebrospinal Fluid Pressure Changes in Response to Coughing*. Brain, 1976. **99**: p. 331-346.
22. Berkouk, K., P.W. Carpenter, and A.D. Lucey, *Pressure Wave Propagation in Fluid-Filled Co-Axial Elastic Tubes Part 1: Basic Theory*. Journal of Biomechanical Engineering, 2003. **125**(6): p. 852-856.
23. Carpenter, P.W., K. Berkouk, and A.D. Lucey, *Pressure Wave Propagation in Fluid-Filled Co-Axial Elastic Tubes Part 2: Mechanisms for the Pathogenesis of Syringomyelia*. Journal of Biomechanical Engineering, 2003. **125**(6): p. 857-863.
24. Bertram, C.D., A.R. Brodbelt, and M.A. Stoodley, *The Origins of Syringomyelia: Numerical Models of Fluid/Structure Interactions in the Spinal Cord*. Journal of Biomechanical Engineering, 2005. **127**(7): p. 1099-1109.
25. Bertram, C., L. Bilston, and M. Stoodley, *Tensile radial stress in the spinal cord related to arachnoiditis or tethering: a numerical model*. Medical and Biological Engineering and Computing, 2008. **46**(7): p. 701-707.
26. Bertram, C.D., *A numerical investigation of waves propagation in the spinal cord and subarachnoid space in the presence of a Syrinx*. Journal of Fluid and Structures, 2009.
27. Cirovic, S., C. Walsh, and W.D. Fraser, *WAVE PROPAGATION IN A SYSTEM OF COAXIAL TUBES FILLED WITH INCOMPRESSIBLE MEDIA: A MODEL OF PULSE TRANSMISSION IN THE INTRACRANIAL ARTERIES*. Journal of Fluids and Structures, 2002. **16**(8): p. 1029-1049.
28. Cirovic, S. and S.E. Majdalawi, *Propagation of the Cerebrospinal Fluid Pulse in the Spine: Analytical and Experimental Models*. Journal of Biomechanics, 2008. **41**(Supplement 1): p. S519-S519.
29. Cirovic, S., *A Coaxial Tube Model of the Cerebrospinal Fluid Pulse Propagation in the Spinal Column*, in *Journal of Biomechanical Engineering Vol.131*. 2009. p. 021008/1-021008/9.
30. Martin, B.A., F. Loth, and T.J. Royston, *Elastic Properties of the Spinal Aqueduct*. Journal of Biomechanical Engineering.
31. Martin, B.A., et al. *Towards non-invasive assessment of the elastic properties of the spinal aqueduct*. in *SBC2009-205111*. 2009.
32. Martin, B.A., *Pressure Wave Transmission within an In vitro Spinal Canal Model with Stenosis and/or Syrinx Present*. 2009.
33. Martin, B.A., et al. *Pathological biomechanics of cerebrospinal fluid pressure in syringomyelia: Fluid structure in interaction of an in vitro coaxial elastic tube system*. in *Summer Bioengineering Conference*. 2009.
34. Martin, B.A. and F. Loth, *The influence of coughing on cerebrospinal fluid pressure in an in vitro syringomyelia model with spinal subarachnoid space stenosis*.

35. ANSYS®\_Academic\_Research, *Release 11.0, Help System, Element Library*: ANSYS, Inc.
36. Wikipedia. *Viscosity*. [cited 2010 Feb. 20]; Available from: [http://en.wikipedia.org/wiki/Viscosity#Viscosity\\_of\\_water](http://en.wikipedia.org/wiki/Viscosity#Viscosity_of_water).
37. Cremer, L., M. Heckl, and B.A.T. Petersson, *Structure - Borne Sound*. 1988, New York: Springer - Verlag.
38. The\_Physics\_Factbook™. *Density of Glass*. [cited 2010 March]; Available from: <http://hypertextbook.com/facts/2004/ShayeStorm.shtml>.
39. Wikipedia. *Poisson's Ratio*. [cited 2009 Jan.]; Available from: [http://en.wikipedia.org/wiki/Poisson%27s\\_ratio](http://en.wikipedia.org/wiki/Poisson%27s_ratio).
40. Adams, V. and A. Askenazi, *Building Better Products with Finite Element Analysis*. 1 edition ed. 1998: OnWord Press.
41. The\_Engineering\_Toolbox. *Densities of Various Solids*. [cited 2010 March]; Available from: [http://www.engineeringtoolbox.com/density-solids-d\\_1265.html](http://www.engineeringtoolbox.com/density-solids-d_1265.html).
42. Schurch, B., W. Wichmann, and A.B. Rossier, *Post-traumatic syringomyelia (cystic myelopathy): a prospective study of 449 patients with spinal cord injury*. *J Neurol Neurosurg Psychiatry*, 1996: p. 61-67.
43. Martin, B.A., et al., *Spinal Canal Pressure Measurements in an In vitro Spinal Stenosis Model: Implications on Syringomyelia Theories*. 2009.

## VITA

**Yifei Liu**

### EDUCATION

M.S., Mechanical Engineering – July 2010

University of Illinois at Chicago, Acoustics and Vibrations Lab

B.S., Mechanical Engineering – July 2002

Dong Hua University, Shanghai, P.R.China

### PRESENTATION WORK – Conference Abstracts

Yifei Liu, Bryn A. Martin, Thomas J. Royston, Francis Loth, " *A Fluid Structure Interaction Simulation of the Cerebrospinal Fluid, Spinal Cord, And Spinal Stenosis Present In Syringomyelia,*" ASME Summer Bioengineering Conference (Naples, FL, 6/16-19, 2010).

### PROFESSIONAL EXPERIENCE

OptiWorks (Shanghai) Co., Ltd., Shanghai, China –	2002~2008
Associate Product Engineer of Optical Switch	2007 ~ 2008
Failure Analysis Engineer	2007 ~ 2008
Product Engineer of VOA (Variable Optical Attenuator)	2006 ~ 2008
Mechanical Engineer	2002 ~ 2008